FROM: ADVANCED EPR: APPLICATIONS IN BIOLOGY AND BIOCHEMISTRY
A.J. Hoff, Ed., Elsevier, Amsterdam, 1989, CHAPTER 5, pp. 177-242

TWO DIMENSIONAL AND FOURIER TRANSFORM EPR

JEFF GORCESTER, GLENN L. MILLHAUSER, AND JACK H. FREED

1. INTRODUCTION

In the past decade, an extensive range of modern time domain two-dimensional EPR techniques for the study of spin relaxation and motional dynamics of small and macromolecules in fluids, including membranes, have been developed based on electron-spin-echo and on Fourier Transform (FT) techniques. A primary concern has been with the spectra of nitroxide spin labels and spin probes.

The nitroxide spin-label technique has, in the last 20 years, permeated many areas of biophysics (1-4). The principal reliance has been on cw-EPR methods despite the somewhat limited features of the characteristic three-line hyperfine (hf) pattern from the ^{14}N nucleus. Of course, as rotational motions slow down, spectra take on a greater range of shapes in the "slow-motional" regime. The analysis of such spectra is more complicated (5,6), but rewarding, because it can supply more detailed information on microscopic dynamics and ordering in membrane systems (6-11). Recent developments in computational methodology have now lead to a convenient but powerful computer program to simulate slow motional spectra that is readily available (12).

But the fact remains that these spectra exhibit rather low resolution to the details of the dynamics, a matter which is exacerbated by the proton (and/or deuteron) super-hyperfine (shf) splittings. In a significant sense, EPR lagged behind NMR in its applications to the study of dynamic molecular structure, despite its virtues of greater sensitivity to fewer spins and the shorter time scale over which it examines motional dynamics. In NMR, after all, one can use spin echoes to measure homogeneous T_2's; pulse techniques give T_1's directly, and modern two-dimensional (2D) methods based on FT-NMR can provide detailed mappings of complicated cross-relaxation pathways.

But now it is fair to say that the new, though sophisticated, time domain EPR techniques have been able to come to the aid of the EPR spin-labeling method. Modern electron-spin-echo methods can provide a display, in a two-dimensional format, of the homogeneous lineshapes across an inhomogeneous EPR spectrum. Alternatively, they can provide the cross-relaxation rates from each point in the spectrum. Such 2D spectra are found to provide much enhanced sensitivity to motional dynamics, and they even place greater demands on the simulation algorithms because of this enhanced sensitivity (13,14).

Perhaps an even more dramatic development has been the recent introduction of two-dimensional FT-EPR spectroscopy for nitroxides. Instead of looking at a simple three line EPR spectrum, one may now observe a two-dimensional display of "auto-peaks" and of "cross-peaks" whose intensities relate directly to cross-relaxation phenomena such as Heisenberg spin exchange and/or dipole-dipole interactions modulated by the diffusion processes. Extension to the slow-motional regime would lead to the complete 2D mapping of the (integrated) transition rates between each and every point in the spectrum. This can only enhance the sensitivity, reliability, and accuracy with which EPR may be applied to questions of dynamic molecular structure.

In this chapter we review these recent developments, explaining the background theory and the methods, as well as the applications which have already been realized, and the potential for further applications. Other recent reviews focus on related matters, including the application of EPR time domain methods for the study of surfaces (15), studies of rotational dynamics in fluids and membranes (16), and the theoretical and computational methods for extracting the molecular dynamics from the EPR spectra (14).

In Section 2, the relevance of electron-spin-echoes (ESE) to studies of molecular motions is reviewed. Then in Section 3, the 2D-ESE method for obtaining T_2 variations across the spectrum is described in some detail. Section 4 provides the description of techniques to study magnetization transfer (e.g. cross-relaxation) variations across the spectrum. This includes inversion recovery, stimulated echoes, and spin-echo electron-electron double resonance (ELDOR). The effects of electron-spin echo envelope modulations on motional studies are outlined in Section 5. The new 2D-FT-EPR techniques are discussed in Section 6, which includes sub-sections on spin-echo correlated spectroscopy (SECSY), correlation spectroscopy (COSY), and 2D-ELDOR. The initial applications of these methods and their future potential are also discussed in this Section.

2. ELECTRON-SPIN ECHOES AND MOTIONAL DYNAMICS

The principal motivations for applying electron-spin-echo (ESE) techniques to spin relaxation in model membranes include: 1) the ability to separate homogeneous from inhomogeneous contributions to the linewidths (or T_2), as well as to profit from the resulting increase in resolution; 2) the ease of simultaneously performing T_1 measurements; 3) the possibility that special ESE techniques could provide information on motional dynamics in addition to that from cw studies; and 4) the possibility of extending the range of study to slower motions. Fig. 1 summarizes the most typically used ESE pulse sequences.

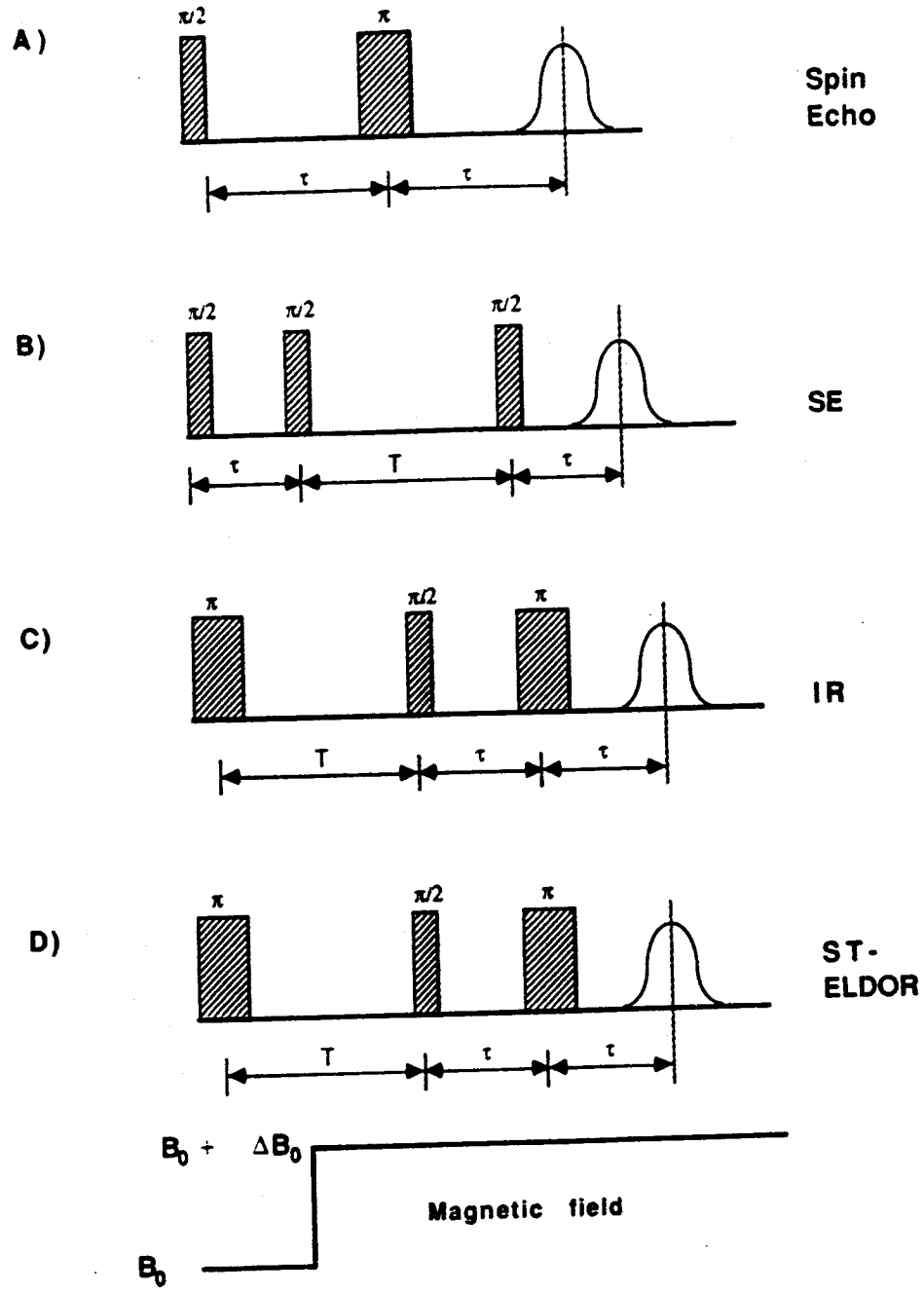

Fig. 1. Typical spin echo pulse sequences: (a) Hahn spin echo (b) Stimulated Echo (c) Inversion Recovery (d) ST-ELDOR echoes.

When an echo technique (17-21) is applied to spin labels with inhomogeneously broadened cw-EPR lines (e.g. due to unresolved--or partially resolved--proton shf interactions in the case of nitroxides) the measured phase-memory time T_M is equal to T_2, the homogeneous linewidth of a single spin packet (21-24) (cf. Fig. 2). Past attempts at removing, or at least reducing, the inhomogeneous broadening were to utilize deuterated spin probes such as PD-Tempone for this purpose, but it is very inconvenient to have to perdeuterate all the various spin labels. A more serious problem occurs in the case of oriented model membrane

samples, where small amounts of disorder can lead to inhomogeneous broadening that is very difficult to distinguish from motional broadening (10,25). ESE techniques now permit accurate experiments on a wide range of nitroxides of different sizes and shapes to obtain T_2's and T_1's, which greatly assist studies on dynamic molecular structure.

The ESE work on nitroxides in liquids shows good agreement with the motionally-narrowed linewidths extracted by cw techniques (cf. Fig. 2). An especially interesting observation (22) was that in the slow motional regime, for $\tau_R \approx 10^{-7}$ to 10^{-6} sec, where τ_R is the rotational correlation time, the phase memory time T_M was found to be proportional to τ_R^{α} with $\alpha \approx 0.5$-1, (cf. Fig. 2). Simple arguments suggested this was to be expected. That is, in the slow motional regime, reorientational jumps should lead to spectral diffusion wherein each jump takes place between sites of different resonant field. This would be an uncertainty-in-lifetime broadening that is analogous to the slow exchange limit in the classic two-site case, and it contributes to T_M. The broadening would then be given by τ_R^{-1}, the jump frequency. This result suggested that studies of the ESE T_M in slow-motional spectra would supply complementary information on motional dynamics to that from cw lineshape studies. A rigorous theoretical basis was established for the analysis of slow-motional ESE in order to interpret such experiments with confidence (23). The theory may readily be computed with the newer cw-EPR slow-motional computer programs (12). This emphasizes that echoes relate to the same type of motional effects as do the cw-lineshapes, but with much better resolution.

The theoretical results on simple $\pi/2$-τ-π-τ echoes (cf. Fig. 1a) clarified the potential of ESE in the study of molecular dynamics. In the theoretical analysis, the relative advantages of simple methods of obtaining τ_R from slow-motional cw spectra (e.g. from first (26) or second derivative (27) outer extreme linewidths) vs. from ESE were compared. It was found that ESE methods are preferable, because the ESE phase memory time, T_M is independent of inhomogeneous broadening. Simple approaches at cancelling out inhomogeneous broadening in cw studies (26,27) are not rigorous, since significant inhomogeneous broadening will have a non-linear effect on the observed cw widths (23,26). It was concluded that careful study of the variation of T_M (i.e. T_2) across the spectrum would be a useful way to proceed in applying ESE to this problem. This led to the two-dimensional spectroscopy approach outlined below.

Let us first summarize the theoretical results on simple $\pi/2$-τ-π-τ echoes. It has been demonstrated that (23): 1) the ESE decay envelopes show a short-time behavior with an $e^{-c\tau^3}$ dependence on τ and a long-time behavior of $\exp[-\tau/T_M^*]$. 2) The asymptotic phase-memory decay constant T_M^* shows a significant dependence on models, and this was traced to the different mechanisms of spectral diffusion induced by these models. 3) The T_M^* obtained from selective echoes on different parts of the (nitroxide) spectrum show significant differences. 4) The short-time

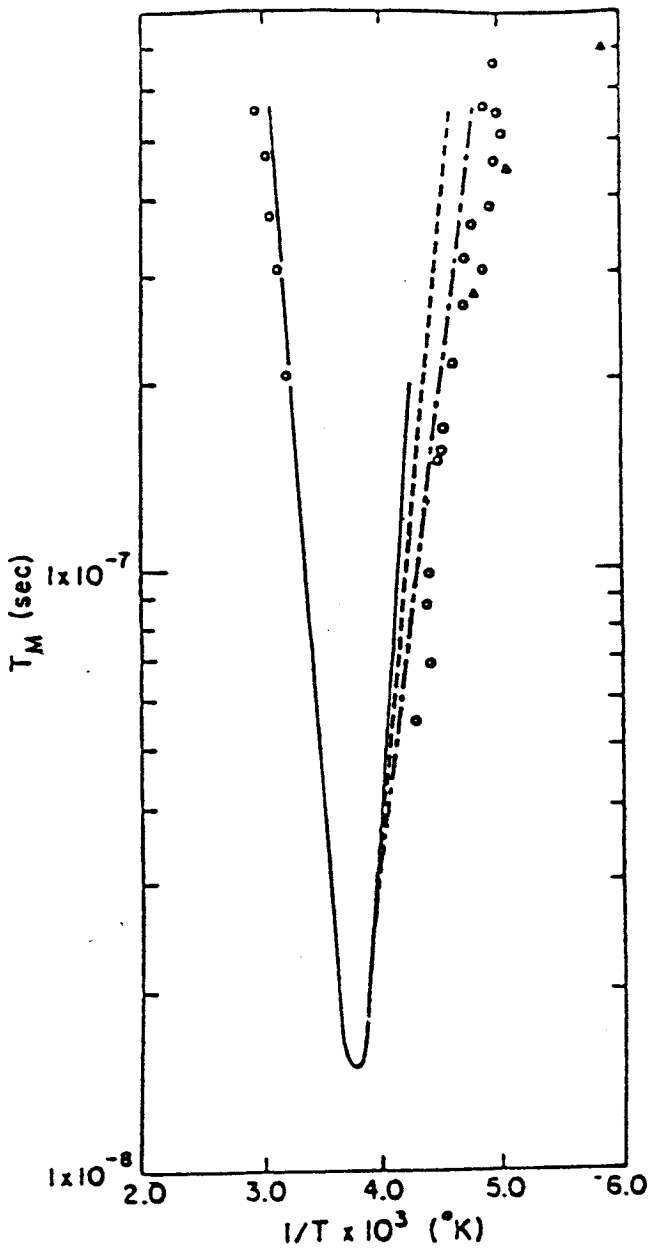

Fig. 2. Plot of T_2 (or T_M) vs T^{-1} for the nitroxide probe Tempone in 85% glycerol/H_2O. The circles show data collected from spin echo experiments; the triangles show T_2 as measured from the center maximum of 2D ESE spectra. The different lines show T_2 calculations from the same spectral region for the different models of jump diffusion (solid line), free diffusion (dashed line) and Brownian diffusion (dashed-dotted line). The calculations employed the values of τ_R extrapolated from the fast-motional regime. [from Ref. 29].

behavior yields a $c \propto \tau_R^{-1}$, and c is independent of diffusional model. The experimental results, such as those in Fig. 2 show that in actual ESE experiments one is primarily sensitive to the T_M^{∞}.

There is an important variant on the simple spin echo. It is the Carr-Purcell (CP) sequence: $\pi/2\text{-}(\tau\text{-}\pi\text{-}\tau)_n$, where the π pulse is applied n times giving rise to

n echoes at times $2m\tau$, m=1, 2...n, and one detects the decay of the echo train for given τ to obtain the decay constant T_M^C. The feasibility of such experiments by ESE was demonstrated by Eliav and Freed (28), and the theory is given by Schwartz *et al.* (23). It was shown that such CP sequences are potentially more informative than just simple two-pulse echoes. In the latter, usually only a single T_M (e.g. T_M^*) is obtained at each spectral position, while in the former a whole set of $T_M^C(\tau)$ vs. τ would, in principle, be obtained, which could be used to explore motional dynamics in greater detail. This is particularly true as τ becomes comparable to τ_R, which results in $T_M^C > T_M^*$ (23). In fact, as $\tau/\tau_R \to 0$, the successive π pulses repeatedly reverse the electron-spin precession so rapidly that the hyperfine and g-tensor anisotropy is (coherently) averaged more effectively by these π pulses than it can be randomized by the slow tumbling. [This is analogous to the NMR case wherein the CP sequence is used to remove the effect on T_2 of translational diffusion in an inhomogeneous applied field].

We now inquire how a two-dimensional technique enables us to obtain maximum information from T_2 measurements. (We shall refer to the T_M as T_2 below).

3. 2D-ESE STUDIES OF T_2 VARIATIONS ACROSS THE SPECTRUM

3.1 The Method

The 2D-ESE method for studying T_2 variations across the spectrum is based upon the theoretical study of ESE and slow motions by Schwartz *et al.* (23). It was shown that the time evolution of the echo height for slow motions could, in general, be represented as a sum of complex exponentials. That is, the observed echo signal, s is given by:

$$s(2\tau+t) \propto \mathrm{Re} \sum_{j,k} a_{kj} \exp[-(\Lambda_k + \Lambda_j^*)\tau] \exp[-\Lambda_k t] \qquad [1]$$

where τ is the time between the $\pi/2$ and π pulses (cf. Fig. 1a) and where $2\tau+t$ is the time period measured from the initial pulse. The echo maximum is expected at time 2τ. In Eqn. [1], Re represents the real part of the complex function to its right and Λ_j and Λ_k are complex eigenvalues discussed below. Eqn. [1] can best be understood in terms of the concept of the "dynamic spin packet" (DSP). That is, in the rigid limit, the inhomogeneously broadened EPR spectrum from a polycrystalline (or glassy) sample is made up of the broad envelope of contributions from many, many (actually a continuum of) spin packets, each one resonating at a definite frequency and associated with the spins on molecules oriented at the appropriate angle with respect to the static magnetic field. The rigid limit spectrum is determined in the usual way in terms of the g-tensor and hyperfine tensor anisotropies.

As the rotational motion increases, each spin-packet in the continuum will "interact" with nearby spin-packets, since the motion will transform molecules contributing to one spin-packet into contributors to another at a different orientation. As a result of this coupled behavior of the original (i.e., rigid-limit) spin packets, there will be new "normal-mode" solutions, the DSP's, which will be linear combinations of the original spin packets. The physics of the problem is described by the stochastic Liouville equation, (5,14), which simultaneously includes the reversible quantum-mechanical spin dynamics and the irreversible molecular dynamics (usually treated classically). Typical spin Hamiltonians and dynamical models are summarized elsewhere (5,14). The eigenvectors of the stochastic Liouville operator are the DSP's, and the Λ_j in Eqn. [1] are the corresponding eigenvalues in the rotating frame. The imaginary parts $Im(\Lambda_j)$ represent the resonance frequencies of the associated DSP [i.e. $\omega_j = Im(\Lambda_j)$], while the real parts $Re(\Lambda_j)$ represent the corresponding natural or homogeneous widths and are associated with the observed $T_{2j} = [Re(\Lambda_j)]^{-1}$. (Note that the asterisk in Eqn. [1] represents a complex conjugation, which requires a simple generalization (23) if echo envelope modulation is to be considered). In general, the relative weights of the DSP's given by the "diagonal" coefficients a_{kk} in Eqn. [1] and the "beats" between pairs of DSP's given by the "off-diagonal" coefficients a_{kj} ($k \neq j$) have a complicated dependence upon the form of these "normal-modes" and of the spin transition moments as averaged over the equilibrium ensemble of molecular orientations. However, near the rigid limit, the a_{kj} simplify to:

$$a_{kj} = (O^T U)_j^2 \, \delta_{kj} \qquad [2]$$

where O is the (nearly) real orthogonal matrix associated with the transformation that diagonalizes the stochastic Liouville operator, while U is the vector of (appropriately averaged) spin transition moments.

When Eqn. [2] applies, Eqn. [1] becomes:

$$s(2\tau+t) \propto \sum_j a_{jj} \exp[-2Re(\Lambda_j \tau)] \exp[-Re(\Lambda_j t)] \cos[Im(\Lambda_j t)] \qquad [3]$$

Thus, in a "two-dimensional" plot of s vs. the two independent variables τ and t, the t dependence includes both the resonance frequency of each DSP and its $T_{2,j}$. If we set t=0 and step out τ, then we obtain the echo envelope as a superposition of exponential decays corresponding to the different $T_{2,j}$ values from each DSP contributing appreciably to the signal. However, such a result would be difficult to disentangle. Instead, let us take advantage of the additional resolution provided by two-dimensional spectroscopy. Let us perform

a double Fourier transform of Eqn. [3], recognizing however that in the near-rigid limit the linewidth for each DSP will largely be masked by various sources of inhomogeneous broadening such as unresolved shf interactions and site variations in the spin-Hamiltonian parameters. We shall therefore assume a Gaussian inhomogeneous width $\Delta \gg T_{2,j}^{-1}$. This yields the two-dimensional spectrum given by:

$$S(\omega,\omega') \propto \sum_j a_{jj} \frac{T_{2,j}}{1+\omega^2 T_{2,j}^2} \exp[-(\omega'-\omega_j)^2/\Delta^2] \qquad [4]$$

which is a sum of Lorentzians along the ω-axis (the FT of τ) and the sum of Gaussians along the ω'-axis (the FT of t). But more importantly, we have separated out the role of the relaxation of each spin packet given by its $T_{2,j}$, which is plotted along the ω axis, from its resonance position in the spectrum given along the ω' axis. In fact, for ω=0 we almost recover the expression for the cw lineshape (with Gaussian inhomogeneous broadening) along the ω'-axis. Thus this separation allows us to observe how the $T_{2,j}$ vary across the whole spectrum. In other words we have succeeded in resolving the different dynamic behavior of the various spin packets, subject however, to the resolution limit due to the inhomogeneous broadening, Δ. Examples of such 2D-ESE spectra appear in Fig. 3.

The actual experimental technique that has been utilized by Millhauser and Freed (MF) (29) is to sweep through the static magnetic field B_0 very slowly, but with a microwave-field intensity B_1 small enough that only DSP's associated with widths well within the inhomogeneous width Δ are effectively rotated by the pulses. MF show that Eqn. [4] applies to their experiment provided that the following set of inequalities apply:

$$\gamma B_s > \Delta \gg \gamma B_1 \gg T_{2,j}^{-1} \qquad [5]$$

where γB_s is the full extent of the spectrum. In this format, one sweeps through B_0 and observes the echo height at 2τ; i.e. one obtains an "echo-induced EPR spectrum" for each value of τ. This provides an $S(\tau,\omega')$ such that the FT in t is automatically obtained. Then an FT in τ is performed after the experiment is repeated for a sufficient number of values of τ to obtain the form of Eqn. [4]. This technique has the advantage of simplicity, a minimum of experimental artifacts, and only low-power microwave pulses are required. However, it is time consuming, typically requiring about 5-10 hours for a complete set of 2D data. One may use a standard ESE spectrometer such as the one illustrated in Fig. 4. We shall show in Sect. 6 that modern techniques now permit such an experiment to be performed with large enough B_1 pulses such that the whole spectrum can be

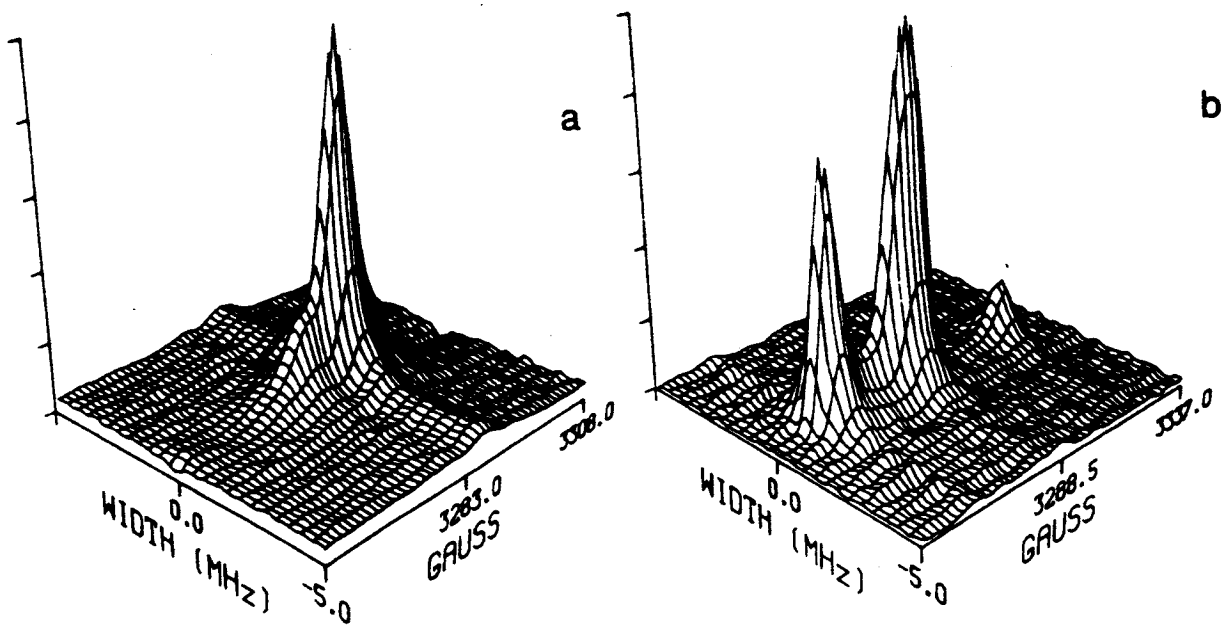

Fig. 3. Experimental 2D-ESE spectra from CSL spin probe in oriented multilayers of low water content DPPC: a) θ=0°, T=-20°C b) θ=90°, T=-20°C where θ denotes the orientation of the director with respect to the external field B_0. The "width" axis provides the homogeneous lineshape, whereas the "Gauss" axis (in units of 10^{-4} T) supplies the inhomogeneous EPR lineshape. [From Ref. 30].

irradiated. For this newest technique, the relevant inequalities would be:

$$\gamma B_1 \geq \gamma B_s > \Delta >> T_{2,J}^{-1} \qquad [6]$$

in order that Eqn. [4] be obtained after a double FT in τ and t. This newest technique is more difficult. Nevertheless, by removing the need to sweep slowly through B0, but instead to gather the whole spectrum after each echo sequence, at the least there is an order-of-magnitude savings in time.

3.2 Examples

The actual data are most usefully displayed not by the full 2D representation, but by normalized contours. These are produced by dividing $S(\omega,\omega')$ by the "zero MHz slice" [i.e., $S(0,\omega')$] to normalize and then to display the constant contour lines (and also the zero MHz slice). A set of horizontal lines imply that there is no T_2 variation across the spectrum, whereas contour lines with curvature indicate the presence of at least some variation. One finds that these contours are very sensitive not only to the rate of reorientation but also to the model of molecular reorientation, (e.g. whether it is by jumps, free diffusion, or Brownian motion) with different characteristic patterns for each! We show in Fig. 5 an actual experimental demonstration of the sensitivity to motional anisotropy by comparing the results for Tempone, which tumbles nearly

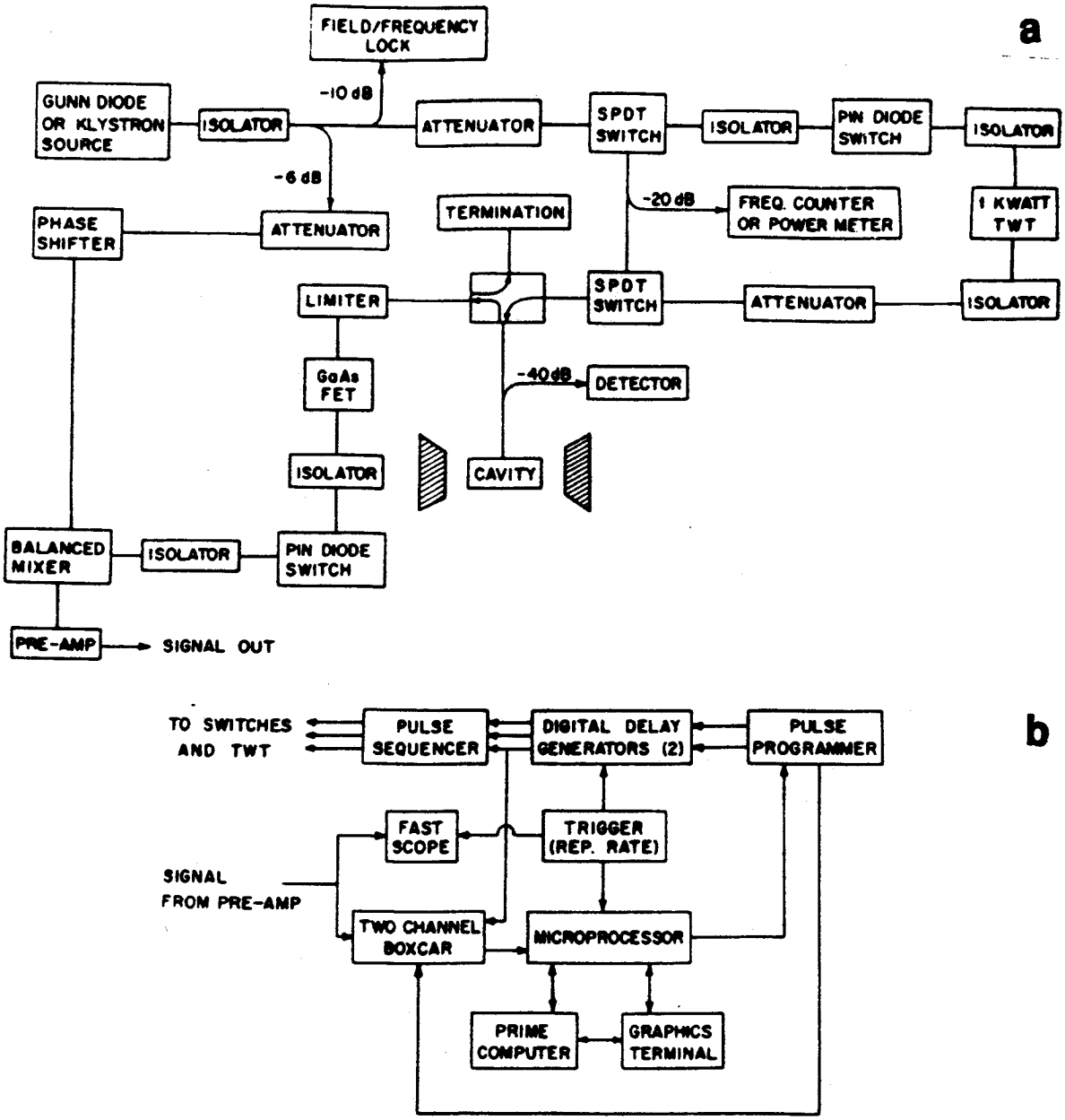

Fig. 4. Block diagram of conventional electron-spin-echo spectrometer that was used for field-swept 2D-ESE experiments. a) Spin-Echo Bridge; b) Digital Electronics.

isotropically vs. those for CSL, whose motion is anisotropic. While the T_2's are comparable, the contour shapes are significantly different, emphasizing the large anisotropy for CSL.

It should also be emphasized that Fig. 5 shows patterns that are consistent with a Brownian reorientation model. In the general theoretical analysis ofthis experiment, MF show that Brownian reorientation, which occurs by infinitesimal steps, will lead to a T_2 variation, because of the different sensitivity of different spectral regions to a small change in molecular orientation [i.e. $dS(\omega')/d\theta$ varies across the spectrum]. On the other hand, reorientation by substantial jumps would not show any T_2 variation.

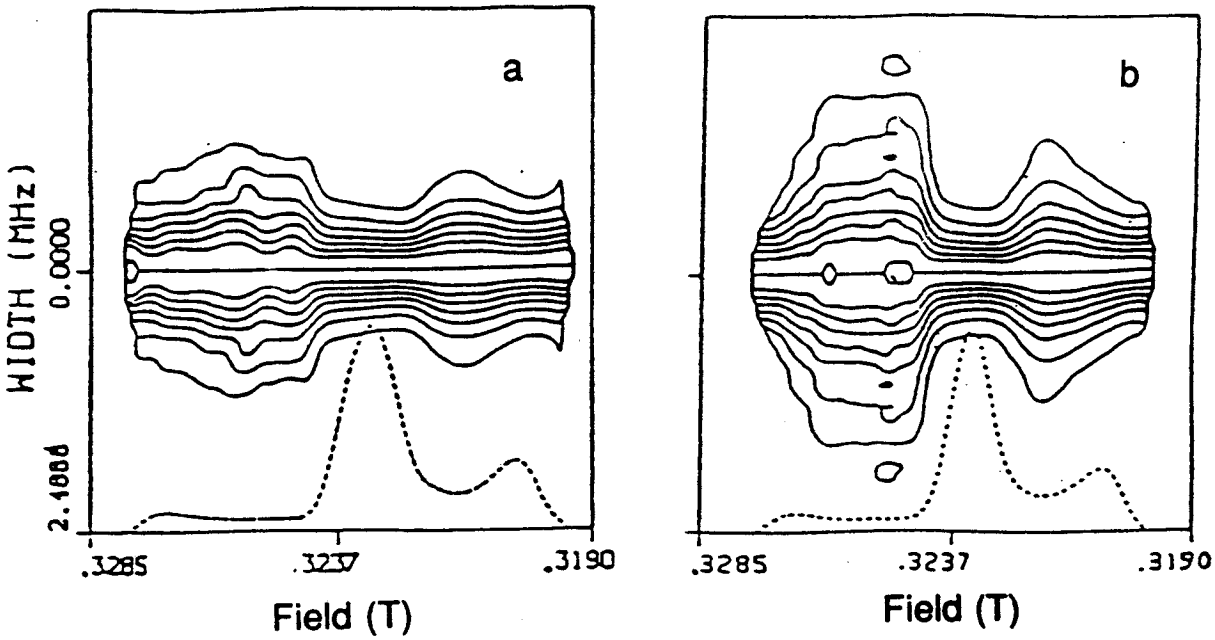

Fig. 5. Normalized contours and zero MHz slices from spectra of two different nitroxides. (a) shows the spectrum of Tempone in 85% glycerol/H_2O at -75°C. (b) shows the spectrum of CSL in n-butylbenzene at -135°C. The T_M's for these spectra, under these conditions, are approximately the same.

We have applied the 2D-ESE technique to oriented phospholipid samples (30) (cf. Fig. 3). In Fig. 6, we show a sequence of experimental contours and zero MHz slices from oriented multilayers of low water-content dipalmitoyl-phosphatidyl choline (DPPC) doped with cholestane spin label (CSL) for different temperatures and angle of tilt θ, and in Fig. 7 we show typical simulations which relate to these results (in particular, Fig. 6a) showing specific sensitivities to the orienting potential as well as details of the dynamics.

We wish to emphasize the importance of this sensitivity. Our studies with CSL in oriented lipid samples have shown that even in the slow-motional region, where cw-spectral simulations are only slightly sensitive to motion, it is very difficult to obtain a unique set of parameters characterizing the system under study (8-10). In fact, temperature-dependent inhomogeneous broadening may dominate the cw-EPR line shapes in the very slow motional region. In the cw line shape analysis, there is a danger of misinterpreting this effect as due to motion! The 2D-ESE results are much more sensitive to these matters as illustrated in the simulations of Fig. 8. In Fig. 8a we show a cw-EPR simulation for high ordering (S=0.87) and very slow motion $R \approx 10^4$ sec^{-1}. We superimpose the results for isotropic (N=1) and very anisotropic (N=100) motions to demonstrate that they are almost indistinguishable. However, in Fig. 8b we show the 2D-ESE contours and 0 MHz slices for the same parameters. They clearly differ both in magnitude and shape and are very easily distinguishable!

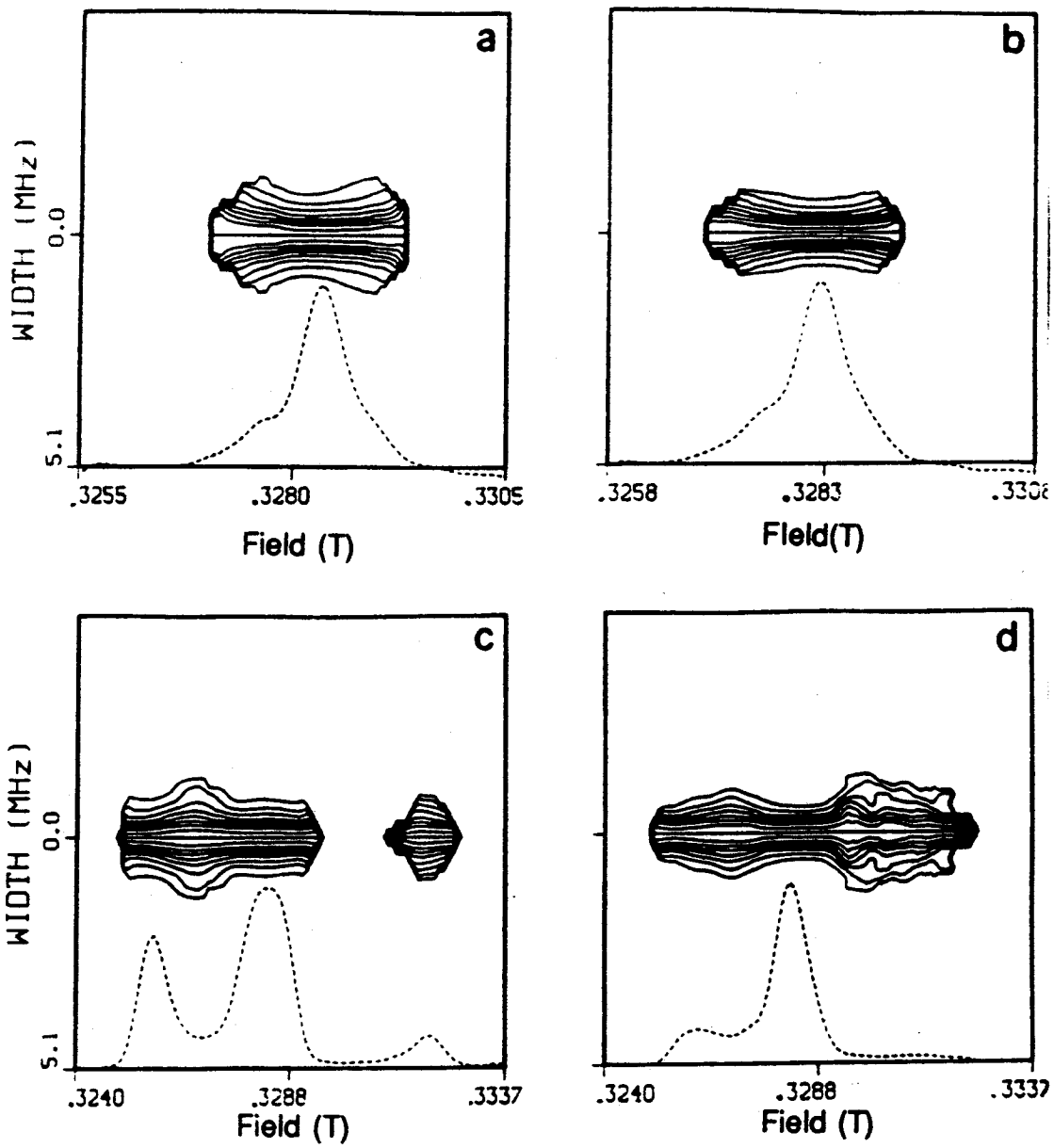

Fig. 6. Normalized contours of experimental spectra from oriented multilayers of low water content DPPC doped with CSL spin probe. (a) θ=0°, T=0°C; (b) θ=0°, T=-20°C; (c) θ=90°, T=-20°C; (d) θ=45°, T=-20°C. [Note b and c correspond to the spectra shown in Fig. 3a and b respectively]. [From Ref. 30].

It is this sensitivity to dynamics and ordering that may be exploited in many biophysical applications. For example, we have obtained well-aligned 2D-ESE spectra for higher water content samples (20 wt. % H_2O) prepared by a combined evaporation and annealing method. Several plate samples are stacked together to increase signal strength. Typical results (31) are shown in Fig. 9. These are interesting because they show significant variation of T_2 across the spectrum, more than previously obtained for lower water content (cf. Fig. 7), and this should enhance the ability to distinguish structure and dynamics.

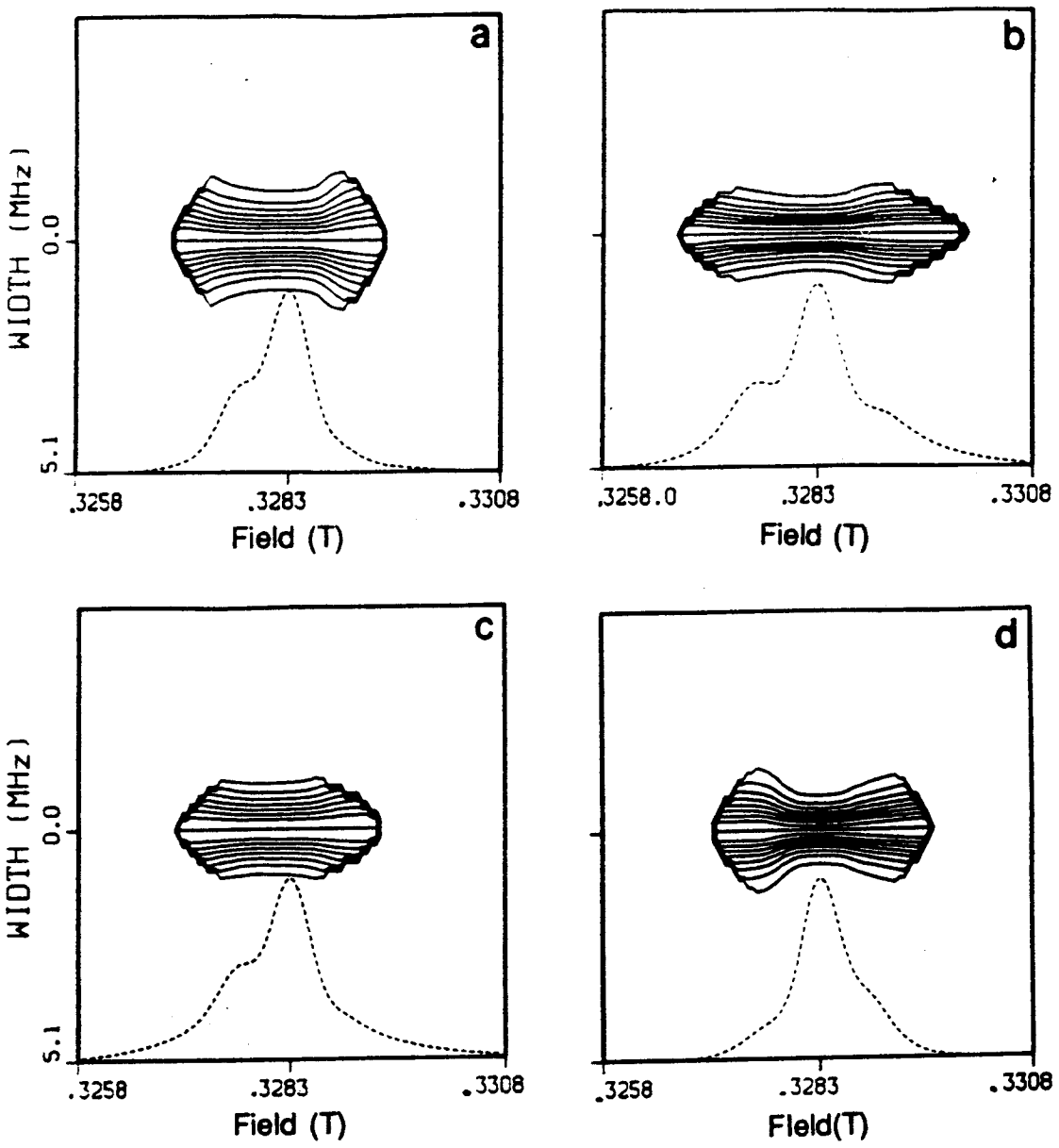

Fig. 7. Normalized contours and zero MHz slices of simulated DPPC/CSL oriented spectra (θ-0°) to illustrate the sensitivity to motion and ordering. (a) $R_\parallel$=4x10^4 sec^{-1}, $R_\perp$=0.8x10^4 sec^{-1}, or N=5 , S=0.85; (b) $R_\parallel$=2x10^4 sec^{-1}, $R_\perp$=0.5x10^4 sec^{-1}, or N=4, S=0.85; (c) $R_\parallel$=$R_\perp$=1x10^4 sec^{-1}, S=0.7; (d) $R_\parallel$=$R_\perp$=1x10^4 sec^{-1}, S=0.91. Here $R_\parallel$ and $R_\perp$ are the parallel and perpendicular components of the rotational diffusion tensor, N = $R_\parallel/R_\perp$, and S is the order parameter. The effects of an intrinsic (solid-state) T_2^{ss} (0.7 μs) and inhomogeneous broadening (0.32 mT) have been included.

Before closing the summary of this technique, we wish to point out that an important experimental artifact has not been included in Eqn. [4], viz. the effect of a non-zero dead-time τ_d after the second pulse (partly due to cavity ringing), so that one is restricted to $\tau \geq \tau_d$. Eqn. [4] may be corrected for this effect by multiplying by a factor: $\exp[-2\tau_d/T_{2,j}]$ inside the summation. However, Millhauser and Freed (32) have shown that a modern technique of data analysis, viz. linear prediction with singular-value decomposition (LPSVD), enables one to back-

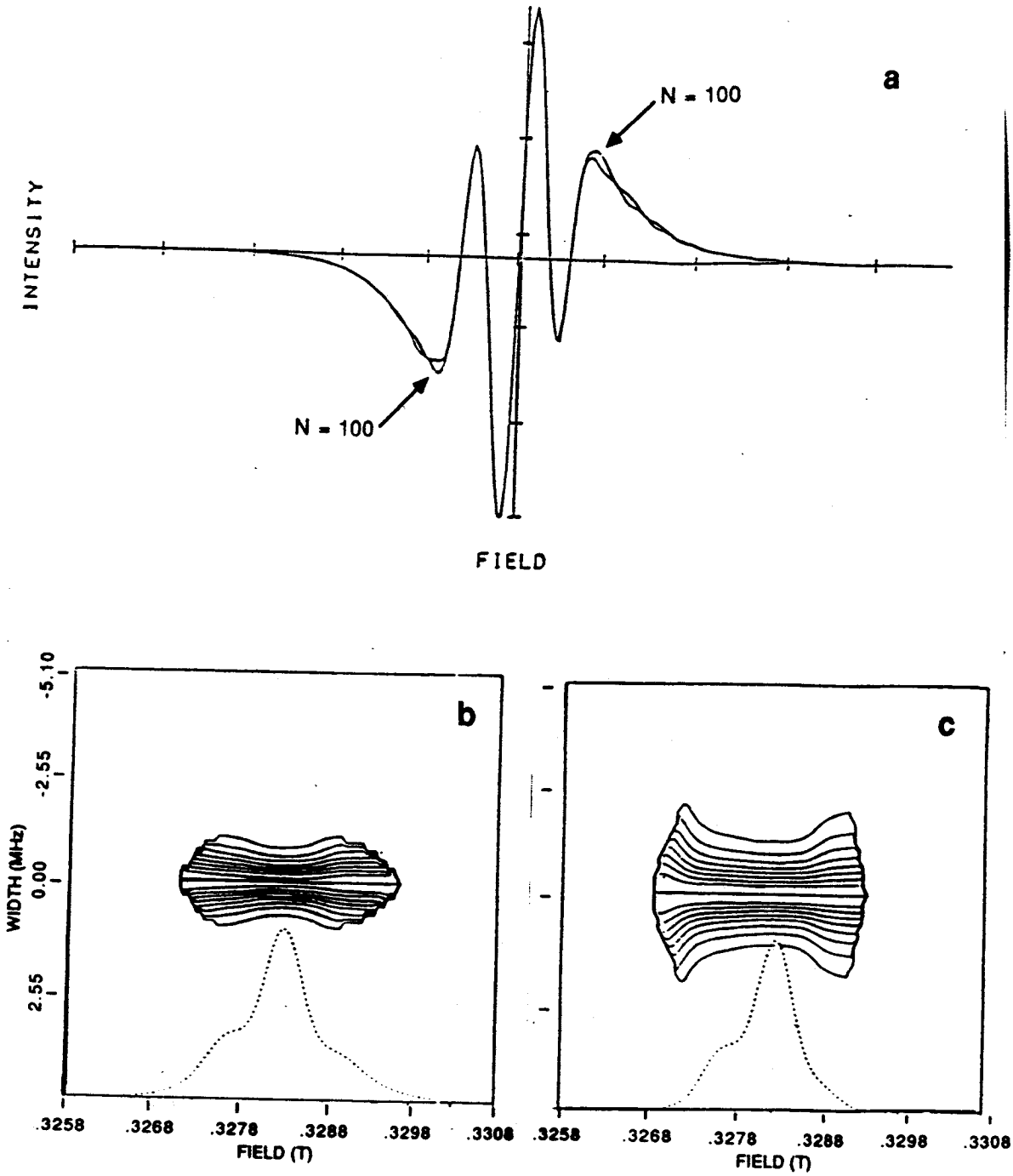

Fig. 8. A comparison of the relative sensitivity of cw vs. 2D ESE to motional anisotropy. (a) Two superimposed spectral simulations where one spectrum has $R_1=10^{-4}$ s^{-1} and N=1, and the other has the same R_1 but with N=100. The markers on the x-axis are 9.77×10^{-4} T apart. The normalized contours are simulated from the same parameters with (b) N=100 and (c) N=1. Case of high ordering, with order parameter S=0.87 and θ=0°.

extrapolate the 2D-ESE data set to estimate the signal in the range $0 < \tau \leq \tau_d$. The LPSVD method also leads both to significantly improved resolution enhancement of the complex 2D line shapes as well as to the least-squares values

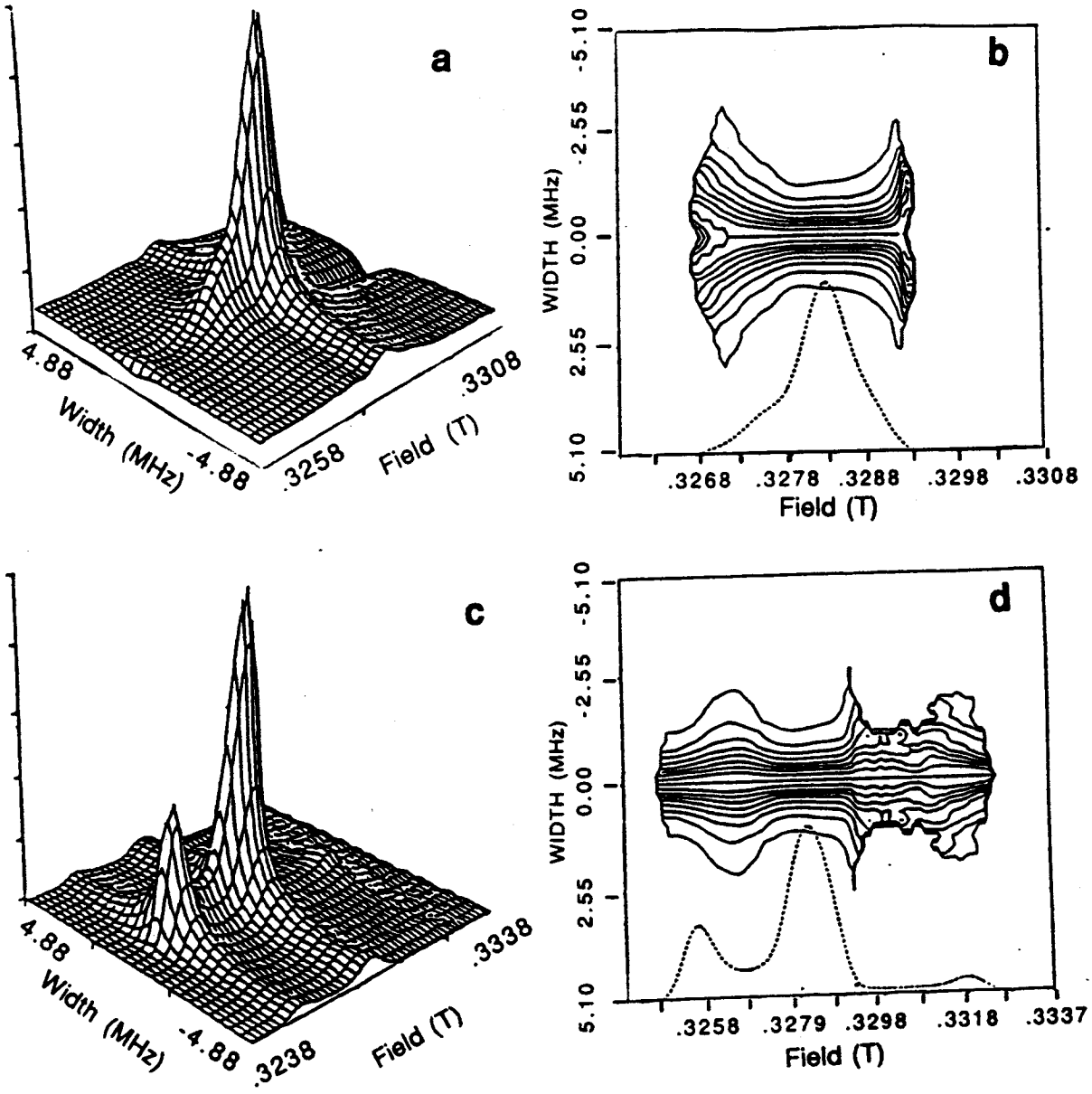

Fig. 9. 2D ESE spectra of DPPC containing a high water content (20% by weight) and doped with CSL spin probe at -40°C. (a) and (b) show the spectrum and associated normalized contours for θ=0°. (c) and (d) are for θ=90°. [From ref. 30].

characterizing the exponential decays consistent with Eqns. [3] and [4] (32). Furthermore, it removes a difficulty with Fast Fourier Transform (FFT) methods. That is, to avoid so-called FFT window effects, it is necessary to collect data over a considerable time range, before performing an FFT. This means that a considerable amount of time is spent collecting data when the signal-to-noise ratio is low, and, hence, the spectral resolution is low. Instead, with LPSVD, one need only collect over those time ranges for which there is a significant

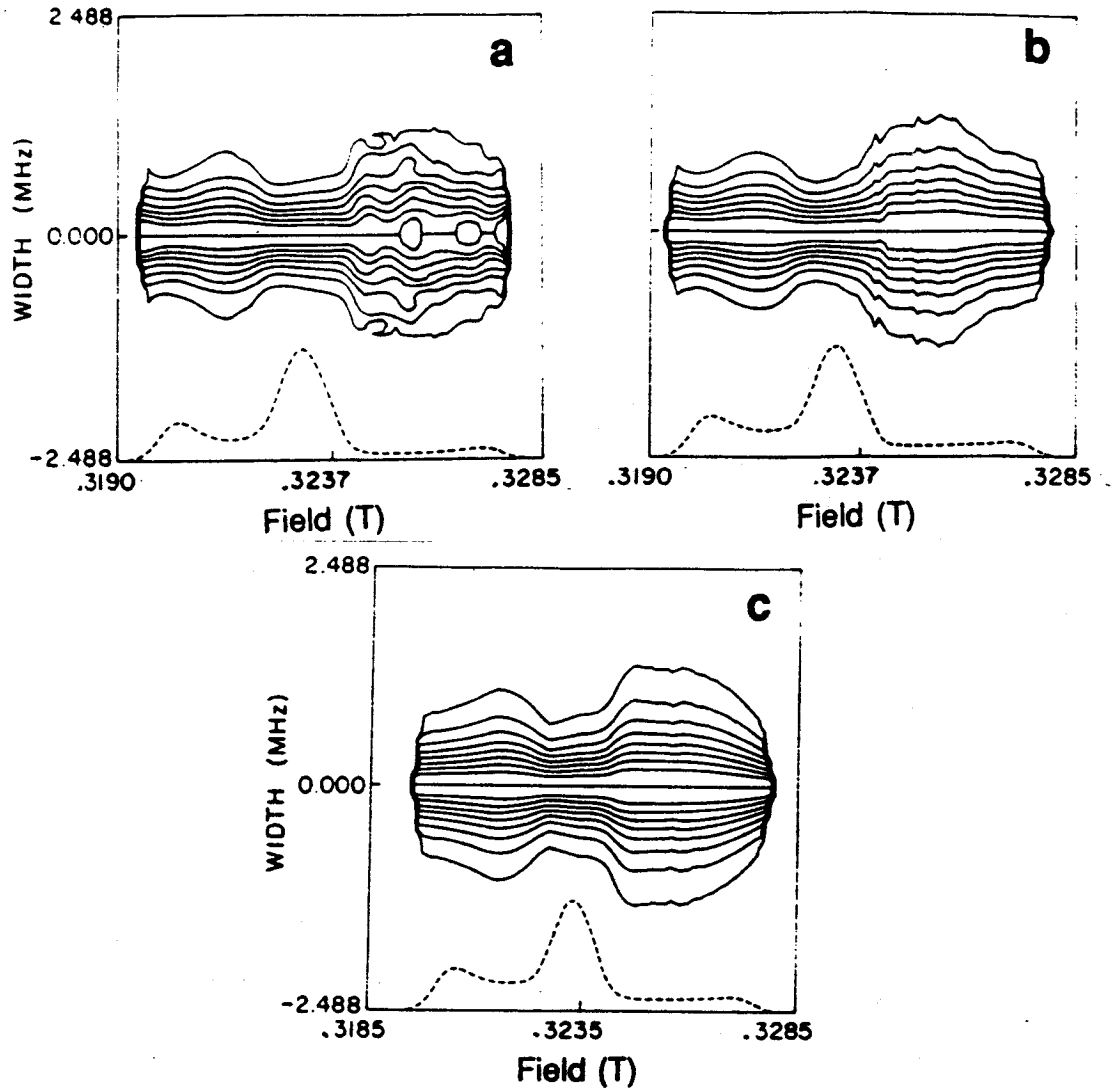

Fig. 10. Normalized contours showing the resolution enhancement obtained from the LPSVD treatment. (a) is from data of Tempone in 85% glycerol/H_2O at -75°C treated by conventional FFT. (b) is from the same data set, but treated with LPSVD. (c) is a different data set that was collected from the same system in a manner that maximizes the efficiency of the LPSVD algorithm. [From Ref. 32].

signal, thereby greatly increasing the efficiency of the data acquisition. These features are illustrated in Fig. 10.

Thus, we have found that the use of LPSVD in the data analysis leads to a much more powerful and useful 2D-ESE method. It means much better discrimination of detail in the 2D contours which translates into a much better analysis of molecular dynamic structure. Its ability to recover signal from noise means, that as long as one is able to obtain echoes yielding an estimate to T_M by usual procedures, then useful 2D-ESE contours may be obtained with the use of LPSVD. This is an important development for model membrane studies. In the case of low-water-content samples (10), it was possible to obtain estimates of T_M from ESE over most of the temperature range from +140° C to -150° C for both CSL and the phospholipid spin label 16-PC, as shown in Figs. 11 However, only a restricted

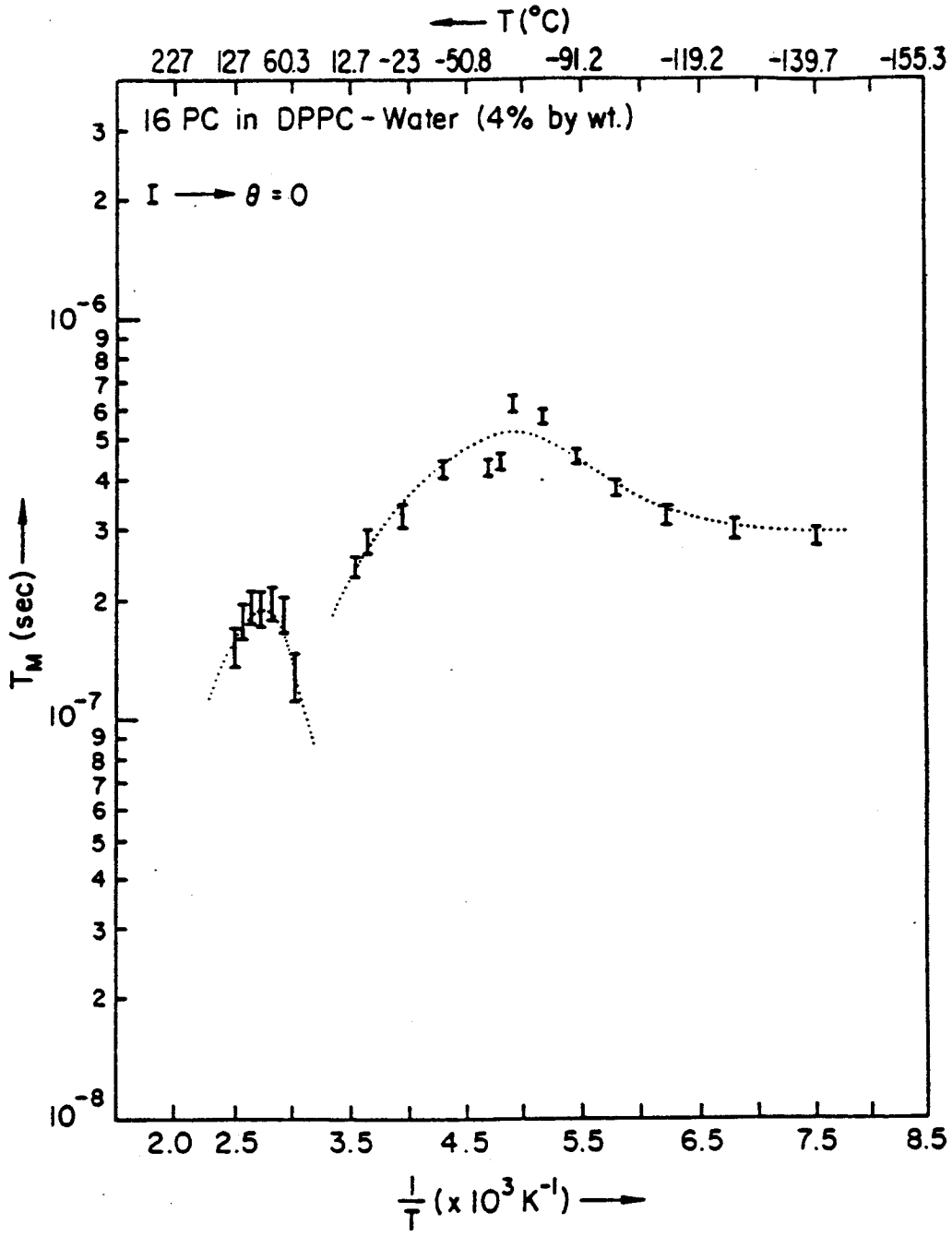

Fig. 11a. Variation of T_M with temperature for CSL in low water content DPPC. The height of the symbols (I,T) marking the data points give an idea of the error associated with each data point [From ref. 10].

range (e.g. cf. Fig. 6) could yield sufficient S/N by conventional FFT methods to recover meaningful 2D-ESE contours from experiments of reasonable duration (ca. 5 hours). With LPSVD and the improved data collection it permits, the whole range of Figs. 11 is now available to 2D-ESE.

Given the fact that this 2D-ESE technique is very sensitive to slow motions, i.e. $\tau_R < 10^{-3}$ sec, it also has applications to the study of slow motional reorientation of spin labeled proteins. In Fig. 12, we show the 2D-ESE spectra

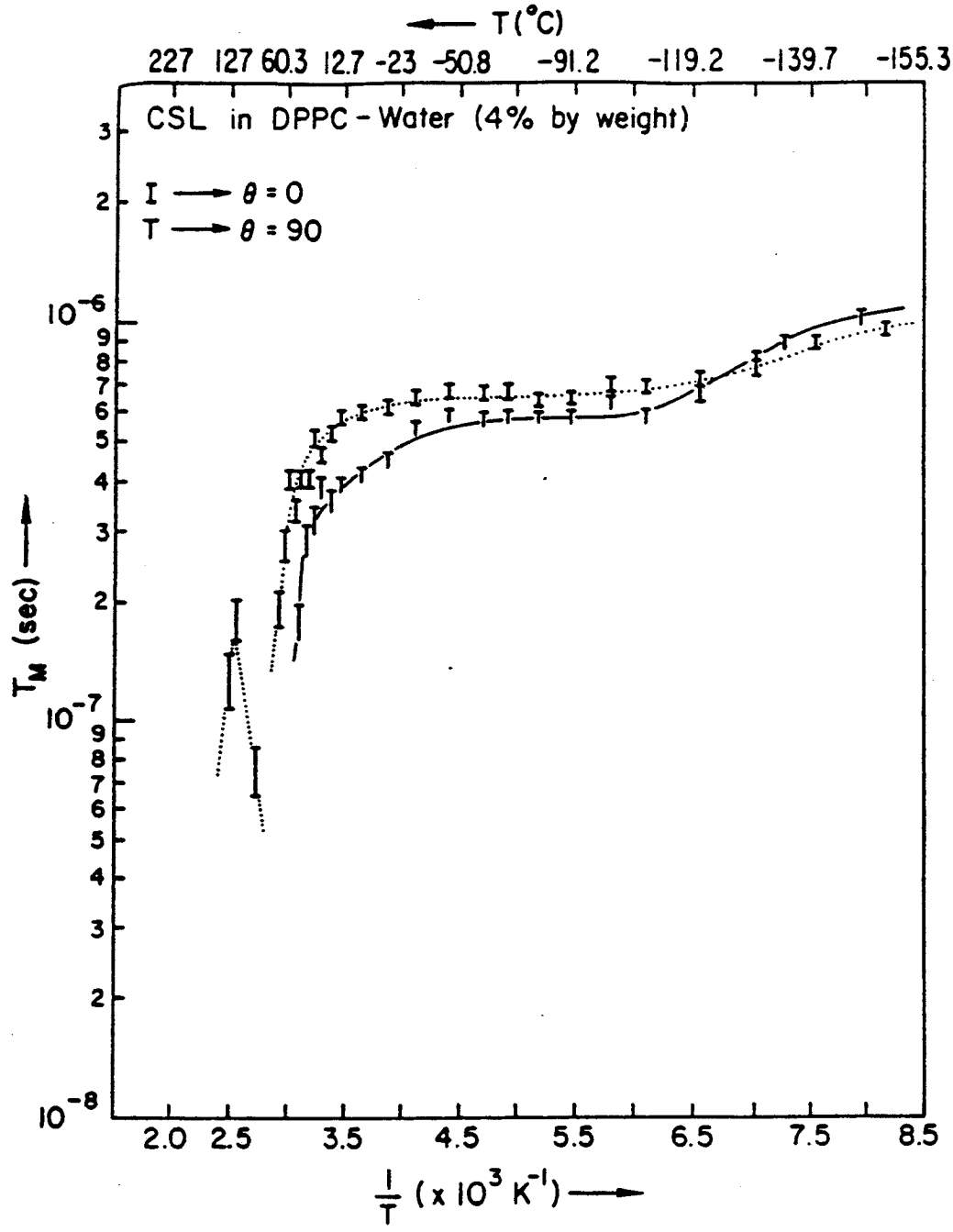

Fig. 11b. Variation of T_M with temperature for 16-PC in low water content DPPC [From ref. 10].

that we have obtained from spin labeled α-chymotrypsin immobilized on CNBr-Sepharose (33). The effects of the rotational motions are still visible in the 2D contours. A more extensive 2D-ESE study of slow tumbling for an immobilized protein has been performed by Kar *et al.* (34).

Finally, we note that saturation transfer (35) is a cw-EPR technique frequently used in a more qualitative fashion to study very slow motions. While relatively easy to perform, the analysis is quite complex. The analysis of 2D-ESE, as discussed above, is more straightforward.

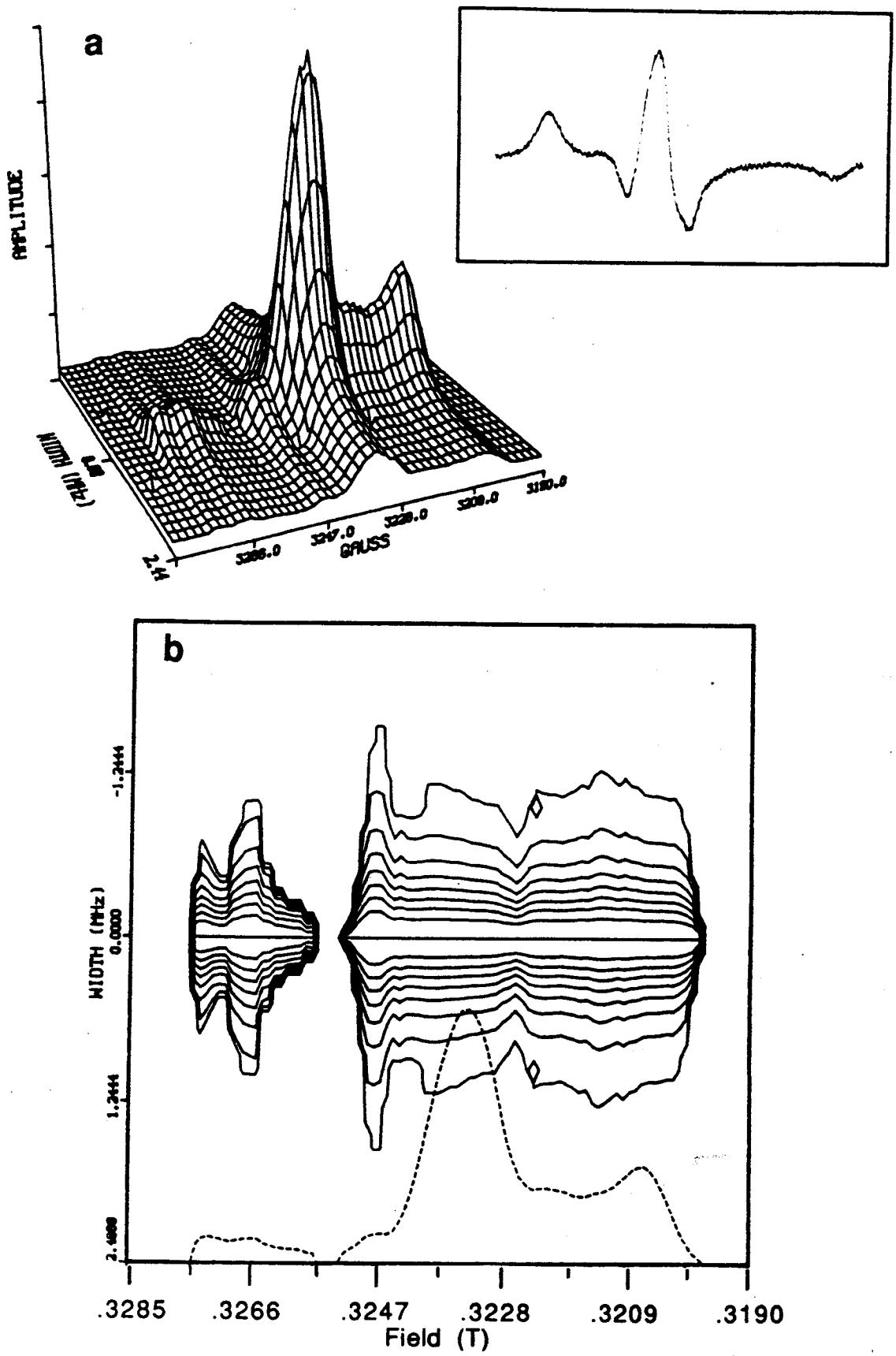

Fig. 12 (a) 2D-ESE Spectrum of α-Chymotrypsin spin labeled with SL-2 immobilized on CNBr-Sepharose Recorded at -55°C. Inset shows derivative of cw EPR spectrum. (b) Contours for (a). [From Ref. 33]

4. 2D-ESE STUDIES OF MAGNETIZATION-TRANSFER VARIATION ACROSS THE SPECTRUM

In the previous section we have demonstrated how, by the use of the standard two-pulse echo sequence, one could obtain a slow-motional 2D ESE spectrum, which is a plot of the spectrum as a function of both the natural line widths and the resonance positions of the DSP's. We now wish to describe an analogous experiment but in the context of T_1 measurements, which provides a "map" of the rates of "magnetization transfer" from each spectral region. However, we must first provide the needed background on echo sequences designed to measure T_1's and more generally "magnetization transfer". First we review (Subsection 4.1) the standard T_1-type measurements, i.e., the inversion recovery (IR) sequence π-T-$\pi/2$-τ-π-τ (cf. Fig. 1c) and the stimulated echo (SE) sequence $\pi/2$-τ-$\pi/2$-T-$\pi/2$-τ (cf. Fig. 1b) (17,21,24,36). We also summarize their theoretical interpretation in terms of motional dynamics. We then describe (Subsection 4.2) the appropriate 2D techniques and provide an example.

4.1 Inversion Recovery and Stimulated Echo Sequences: Full Irradiation

The IR sequence first inverts the z-magnetization with a π pulse, and after a time T, the z-magnetization is probed by a simple $\pi/2$-π echo sequence (cf. Fig. 1c). If the spectrum is fully irradiated by a "non-selective" pulse, then by stepping out T, one observes a simple exponential decay with decay constant T_1 equal to $(2W_e)^{-1}$, where W_e is the pure electron-spin-flip rate, assumed for simplicity, to be isotropic. This result is true both in the fast-and slow-motional regimes.

The SE sequence is more sophisticated (cf. Fig. 1b). The first pulse of this sequence (called the preparation pulse) nutates the dynamic spin packets first into the x-y plane, where they precess at their individual Larmor frequencies for a time τ. During this evolution period the DSP's get out of phase, and the projection of each DSP onto the rotating y'-axis at time τ, which will be nutated onto the z-axis by the second pulse (taken as being about the x'-axis) will depend upon its Larmor frequency. In this manner, the DSP's are "frequency-labeled" during this first τ interval. During the second (i.e., T) interval (referred to as the mixing period), electron-spin flips will reduce the negative magnetization component M_z just as in the IR sequence, and this would be independent of the individual DSP labeling for an isotropic W_e. Unlike the situation in the IR sequence, motion and nuclear-spin flips will also be effective during this mixing interval. This is because, as the molecules reorient or change their nuclear-spin state, they change the DSP's to which they contribute. An echo will be formed at a time τ after the third (or detection) pulse only to the extent that the frequency labeling is still accurate at the end of the mixing interval. The more effective is the motion and/or the nuclear spin flips at changing (during the mixing period) the DSP's to which a molecule contributes, the weaker will be the echo after the detection pulse.

At this point the reader may be concerned by the fact that DSP's are being "interconverted" by the molecular dynamics. Are they not the normal-modes? The answer to this question lies in the fact that the DSP's as introduced above refer to normal-mode solutions for spin-packets precessing in the rotating x'-y' plane, hence the designation of T_2-type behavior. When the spins are rotated to the (negative) z-axis, then the effective stochastic Liouville operator (in particular the spin part) is different, so that the normal-mode solutions are different, even though the molecular dynamics is unchanged. These are the T_1-type normal modes (24,36). For example, for the case of a simple g-tensor spin-Hamiltonian describing ultra-slow motion near the rigid limit, the DSP's are to a first approximation the rigid-limit spin packets (i.e., a continuum with each member representing a particular orientation), while the T_1-type normal modes are found to be the spherical harmonics (i.e., the eigenfunctions of the simple rotational diffusion operator which span the Hilbert space defined by the molecular orientations). This is why it is possible for the T_2-type DSP's to be interconverted during the period when T_1-type relaxation is occurring. The general theory (24,36-38) allows one to consider the appropriate normal modes at each stage of the pulse sequence and their interconversion by each pulse.

The theoretical results therefore predict that the T_1-type relaxation in slow motional "magnetization-transfer" (MT) experiments may be expressed as a weighted sum of exponential decays, whose time constants represent the T_1-type normal modes. Let us call them the MT modes. The weighting factors depend, in part, on τ, which measures how long the DSP's dephase by their precession in the x-y plane after the first $\pi/2$ pulse.

As discussed above, the case of the IR sequence with full irradiation reduces to just a single exponential form:

$$s(T+2\tau) = A[1-2\exp(-2W_eT)] \qquad [7]$$

where $s(T+2\tau)$, the signal at time $T+2\tau$, is that of the echo maximum (cf. Fig. 1c). For SE with full irradiation, the result is written as:

$$s(T+2\tau) = \sum_p b_p(\tau)\exp(-\Lambda_{d,p}T) \qquad [8]$$

where $\Lambda_{d,p}$ is the decay rate for the p^{th} MT mode. While it would be difficult to detect many superimposed exponentials, we have found that in the limit of $W_e\tau_R \ll 1$, this expression is fit to a good approximation by a sum of only two exponential decays, i.e., as:

$$s(T+2\tau) = A + B\exp(-2W_eT) + C\exp[-T/T_A] \qquad [9]$$

where $T_A(\tau)$ is the MT time, which decreases with τ. One can show that at τ=0, C=0, so there is only a single exponential decay in $2W_e$, since there is insufficient evolution time for the spins to precess appreciably in the x-y plane, and the first two $\pi/2$ pulses thus add to a single π pulse. The more interesting limit is for $\tau > T_2^*$, the effective decay time of the free-induction decay (FID), (while also $\tau < T_2$), for which T_A approaches an asymptotic value such that $T_A < (2W_e)^{-1}$. Also B and C take on asymptotic values independent of τ that are in general significant. In this case the frequency labeling during the evolution period is complete, so that MT during the mixing period can have its maximum effectiveness. We find this asymptotic value to be $T_A \sim \tau_R/b$ where b ≈ 2.5 for Brownian motion and b ≈ 1 for jump motion (24,36). In the limit $W_e\tau_R \gg 1$, the slow motional MT is too weak, so the results are again simply described by Eqn. [7].

4.2 2D-ESE and Magnetization Transfer: Partial Irradiation

By analogy to the 2D technique providing T_2 variation across the spectrum, we can devise an experiment to provide the MT or T_A variation across the spectrum by employing partial irradiation. However, in the case of partial irradiation, both IR and SE sequences yield signals of the form of Eqn. [8] which are well represented by Eqn. [9] for all positions in the spectrum. There is now an extra MT mechanism, viz. MT shifts spins that are initially irradiated to frequencies outside the irradiated region. When this occurs, the spin is no longer detectable, and it is as though it has relaxed back to equilibrium. More precisely, spins rotated into the x-y plane by the (frequency) selective preparation pulse will not even be affected by the second or mixing pulse and/or the detection pulse if they are transferred out of the irradiation "window". This mechanism is more important for IR than for SE, since in the latter case the basic spin-delabeling mechanism, described above, already supplies a closely related effect on T_A.

In summary, the relative effectiveness of MT out of the different spectral regions can be studied by such a partial irradiation technique, but first the two decays in $(2W_e)^{-1}$ and T_A^{-1} must be separated in the data processing. This is again accomplished by applying LPSVD.

We now consider mechanisms whereby T_A can vary across the spectrum. Suppose a molecule whose principal magnetic axis is parallel to the applied field (θ=0°) makes a small Brownian jump by $\Delta\theta$. Its new spectral frequency will hardly change, because the orientation-dependent part of the resonance frequency mainly goes as $3\cos^2\theta$-1, which for θ=0° or 90° gives a change of $\Delta\omega \propto (\Delta\theta)^2$. However, for a molecule oriented at $\theta \sim 45°$, that same Brownian jump will cause a corresponding spectral frequency change given by $\Delta\omega \propto \Delta\theta$. Thus, the spin packet at the θ=45° orientation experiences the more effective MT out of an irradiated region. Similarly if there is anisotropy of the diffusion tensor (e.g., let there be rapid

rotation only about the molecular y-axis) then DSP's associated with the perpendicular (i.e. x and z) orientations will experience more rapid MT than DSP's associated with the y-orientation, thus yielding a greater T_A^{-1} for those DSP's associated with the perpendicular orientations.

The more general form of Eqn. [8] for SE with partial irradiation is (24,36,37,38):

$$s(T+2\tau) = A' \exp(-2W_e T) \sum_p b_p^{\omega}(\tau) \exp(-T/\tau_p) \qquad [10]$$

where

$$\tau_p^{-1} = \Lambda_{d,p}^{-1} - 2W_e \qquad [11]$$

and

$$b_p^{\omega}(\tau) = \sum_{n',\ell',j'}^{\omega} \sum_{m,k,i} \sum_{s,q} O_{o,qn'} O_{o,mn'} O_{d,mp} O_{d,k,p} O_{o,k\ell'} [O_{o,i\ell'} O_{o,ij'}^{*}] O_{o,sj'}^{*} \times \exp[-(\Lambda_{o,n'} + \Lambda_{o,j'}^{*})\tau] \qquad [12]$$

(For a nitroxide with 3 allowed transitions, s and q take on values -1, 0, and 1). Here O_o is the orthogonal transformation introduced in the previous section, which diagonalizes the stochastic Liouville operator associated with the DSP's and O_d is the equivalent orthogonal transformation for the MT modes. The $\Lambda_{o,n'}$ are the eigenvalues of the DSP's while the $\Lambda_{d,r}$ are those for the MT modes. The primes appearing on the indices n', ℓ', and j' imply that these are summed only over those DSP's which are within the irradiation window of the selective pulse, (i.e. they depend upon ω_j-ω). This gives an implicit dependence upon ω as indicated. We have actually used this form for the theoretical predictions given below (24,36). (In the near rigid limit, when Eqn. [2] applies, we may let $\sum_i O_{o,i\ell'} O_{o,ij'}^{*} \approx \delta_{\ell',j'}$ to achieve some simplification of Eqn. [11]). Fortunately, the results are approximately fit by Eqn. [9] at each position in the spectrum! Also, W_e is found to be constant, within experimental error, across the spectrum. (But we shall encounter an expression like Eqns. [10]-[12] in Sect. 6). Thus, after extracting the term in $\exp(-T/T_A)$ by LPSVD, and after FT, one obtains a plot of $T_A/(1+\omega^2 T_A^2)$ across the spectrum with normalized contours showing the variation of T_A.

We illustrate this 2D-MT experiment for the NO_2/vycor system in which the NO_2 is physisorbed on the vycor surface. We display in Fig. 13 the 2D normalized contours for T_A obtained at 35 K. Focussing on the M_I=0 region (the central region), we see that the broadening that corresponds to the x and z molecular axes

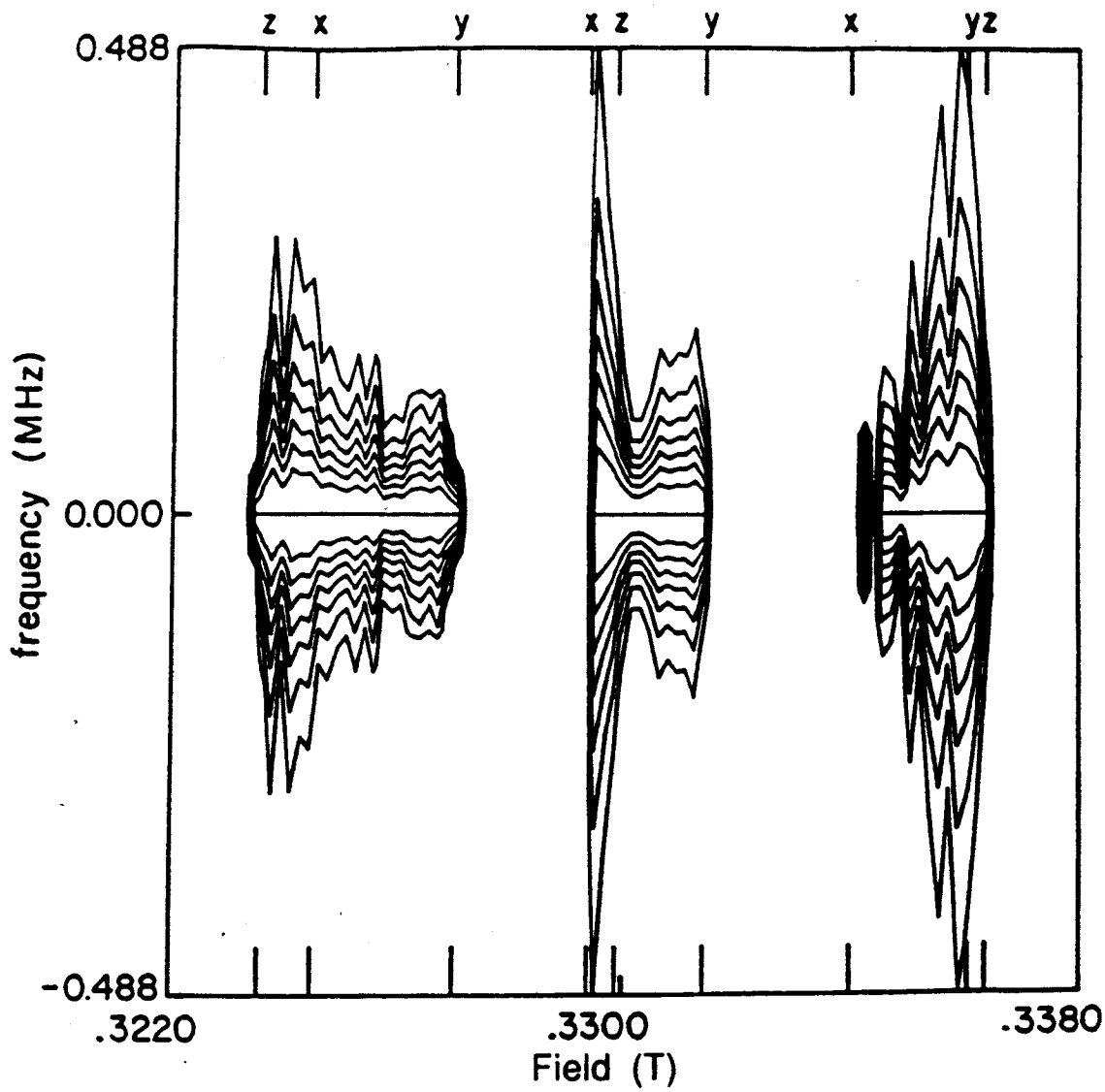

Fig. 13. Two-dimensional ESE contours from stimulated echo sequence for NO_2 on vycor at 35 K showing rates of magnetization transfer. It shows relatively rapid rotation about the molecular y axis (i.e. the axis parallel to oxygen-oxygen internuclear vector). [From Ref. 36].

being parallel to the field is quite dramatic. This is clear evidence for more rapid rotation about the y-axis, which is the axis parallel to the line connecting the two oxygen atoms. The contours in the $M_I=\pm 1$ regions indicate less clear trends, probably due to inhomogeneous broadening from site variation in the hf-matrix. This example indicates the potential utility of the 2D-MT experiment, which can provide useful information about molecular dynamics even prior to a thorough quantitative spectral analysis. Furthermore, it appears that rotational motion is detectable at lower temperatures than with the T_2-type 2D-ESE experiment described in Sect. 3. The relationship to the new 2D-FT techniques will be discussed in Sect. 6.

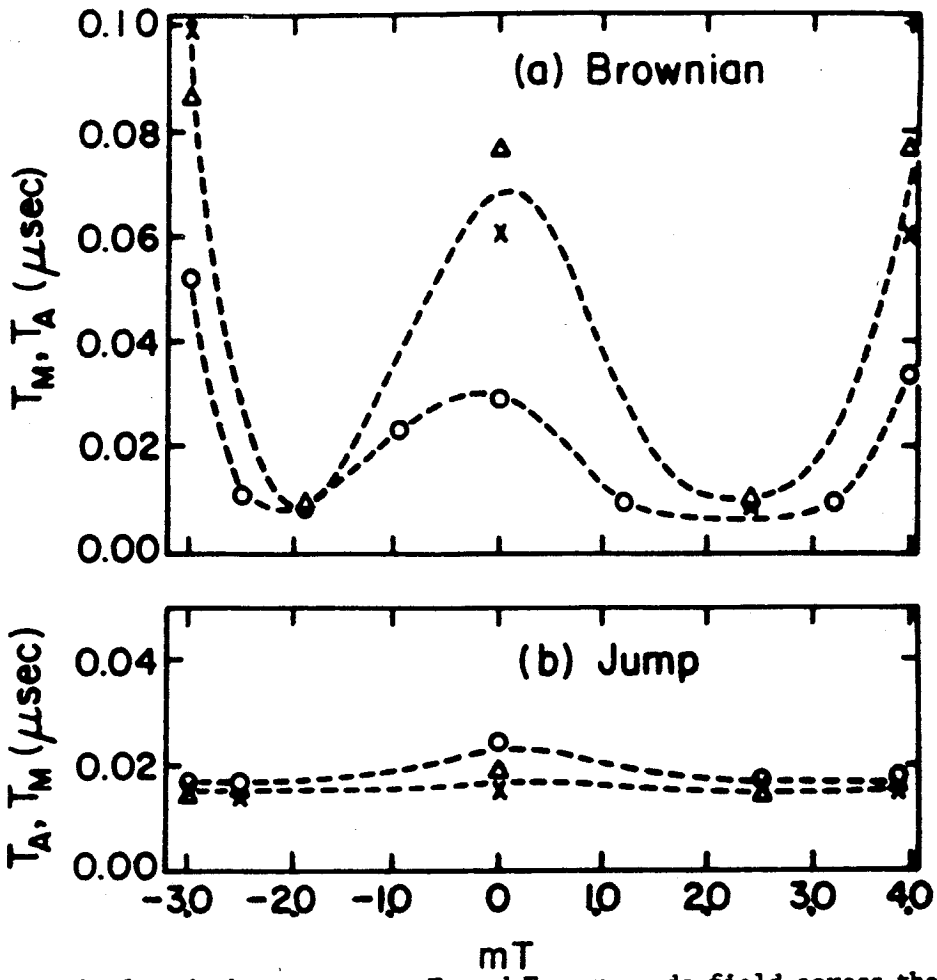

Fig. 14. Calculated time constants T_A and T_M versus dc field across the nitroxide spectrum for partial irradiation. The irradiation window is 4×10^{-4} T. The T_A from the IR sequence are (×), those from the SE sequence are (Δ), while the T_M from a spin-echo sequence are (0). (a) Brownian motion and τ_R=170 nsec, W_e=0.05/τ_R; (b) Moderate jump model, τ_R=17 nsec, W_e=0.05/τ_R [From Ref. 36].

We conclude with some theoretical predictions (24,36), summarized in Fig. 14, which show that this technique is very sensitive to the model of molecular motion.

4.3 Spin Echo ELDOR

A spin-echo ELDOR technique has also been developed and has been applied to the study of slow motions (39). While ELDOR has typically been applied in the past as a cw technique (40), pulsed ELDOR is also possible (41). The use of cw-ELDOR for the study of slow motions was suggested some time ago by Bruno and Freed (42), and detailed cw studies and analysis were performed by Hyde and Dalton (43). The use of spin echoes in such studies was suggested previously (38). The advantages of an echo technique for ELDOR are 1) the absence of the radiation fields (as well as any dc field modulation) during the evolution time of the spins and the (rotational) diffusion of the molecules, 2) the cancellation of effects of inhomogeneous broadening, and 3) the direct measurement of relaxation rates rather than just their ratios, such as obtained by cw ELDOR. This latter advantage

also exists for pulsed ELDOR based on saturation recovery techniques (44). Thus (1) permits a much simpler theoretical analysis (in terms of the stochastic Liouville equation), while (2) suggests greater accuracy in data analysis (without having to resort to deuteration of spin labels as we already noted) and (3) removes the need for additional techniques.

ELDOR may be regarded as the epitome of magnetization transfer experiments by EPR. One first inverts the z-magnetization of some spin packets, and at a later time, one "observes" whether this spin inversion has been transmitted to another part of the spectrum. Thus, whereas the previous MT methods merely observe the rate of loss of magnetization from a given spectral region, ELDOR shows to which regions(s) of the spectrum they are delivered.

The precise technique that was first used (39) is a stepped-field method in conjunction with a conventional three-pulse π-T-$\pi/2$-τ-π-τ sequence used to measure T_1's by IR (cf. Fig. 1d). We call this technique spin-echo ST-ELDOR. The first π pulse inverts the magnetization at one resonant field B_0 in the spectrum. Then B_0 is rapidly stepped by ΔB_0 to a new region of the spectrum, and the $\pi/2$-τ-π pulses are applied to yield the usual echo at time τ after the last π pulse. In this experiment T is varied, while τ is maintained at a fixed value. The echo amplitude, as a function of T gives the variation of the spin magnetization at the spectral region $B_0 + \Delta B_0$ due to the initial inversion of the spins at B_0. It is thus a direct measure of transfer of spin polarization. Similar experiments have also been performed by Soviet workers (45).

Stepped magnetic fields in the local region of the EPR sample are produced by a coil wound on the inside tube of a variable temperature dewar cavity insert. A specially constructed pulsed current supply provided the current for driving the coil. It is driven by a variable width and amplitude pulse from a pulse generator triggered by the EPR spectrometer. Current pulses with a rise time of 100 nsec could be produced, but the characteristics of the turn-off are much poorer. Thus the field-step is turned on after the first π pulse and maintained during the $\pi/2$-τ-π-τ sequence.

The characteristic feature of the results is the initial decrease in signal vs. T to a minimum followed by a slower return to an equilibrium value. (cf. Fig. 15a). The shape of s(T) is consistent with a model in which a portion of the spins inverted in one region is transferred to another and then relaxes back to equilibrium. The transfer of spin polarization can be due to rotational reorientation, while W_e would then restore the spins to equilibrium.

A simplified analysis of this experiment, based on the model of strong-jumps leads to the following discussion (39). The orientation-dependent echo-signal, $S(\Omega_i,T)$ at Euler angles specified by Ω_i due to initially irradiating the spectrum corresponding to Ω_j is given by:

$$S(\Omega_i,T) \propto \frac{-1}{8\pi^2}\ (e^{-T/T_1} + e^{-\omega' T}[8\pi^2\delta(\Omega_i-\Omega_j)\ -\ 1]) \qquad [13]$$

where $\omega'=T_1^{-1} + \tau_R^{-1}$, and $\delta(\Omega_i-\Omega_j)$ is the Dirac delta function. Here $T_1=2W_e$, which is assumed to be largely independent of orientation. Thus, if $\Omega_i \neq \Omega_j$ one has:

$$S(\Omega_i,t) \propto \frac{-1}{8\pi^2}\ [e^{-T/T_1} - e^{-\omega' T}] \qquad \Omega_i \neq \Omega_j \qquad [14]$$

Eqn. [14] clearly shows that there will be a non-negligible effect only if τ_R is not much longer than T_1. In actual fact, a range of Ω_j are affected by the first π pulse, while the detecting pulses "observe" a range of Ω_i. Thus we may write:

$$S(\Omega_i,T,\tau) = S_o(\Omega_i,\tau)\ (1-C(\Omega_i,\Omega_j)[e^{-T/T_1}-e^{-\omega' T}]) \qquad \Omega_i \neq \Omega_j \qquad [15]$$

where $S_o(\Omega_i,\tau)$ measures the echo signal from a conventional $\pi/2$-τ_2-π-τ_2 sequence that arises from the dynamic spin packets in the appropriate range of orientations centered about Ω_i. Also, $C(\Omega_i,\Omega_j)$ is a factor determined by the range of orientations centered about Ω_i, whose spins are initially inverted, and the range about Ω_j, whose spins are "observed." It is both an instrumental factor via B_1 and a function of the spectral lineshape. This factor can be removed from the analysis by solving for T_{min} such that $S(\Omega_i,T,\tau)$ is a minimum. One easily obtains:

$$\ln(1 + T_1/\tau_R) = T_{min}/\tau_R \qquad [16]$$

However, the "integrating effect" over a range of orientations still remains in the technique. (2D-FT-ELDOR described in Sect. 6 would <u>not</u> suffer from such integrating effects and would permit Ω_i - Ω_j to be arbitrarily small).

An extensive theoretical analysis of ELDOR spin-echoes based upon the stochastic Liouville equation has been developed (24). This analysis confirms the semi-quantitative validity of the simple analysis for jump diffusion, but it also rigorously extends the theory to all types of motions. The general results can again be approximated by Eqn. [15] with specific values of S_o and C given as a function of the resonant frequencies initially inverted and then observed. Also, the precise definitions of T_1 and ω' are modified somewhat. However, a mechanism of orientation-independent nuclear spin flips was found to be potentially important in generating ELDOR effects (cf. Fig. 15b).

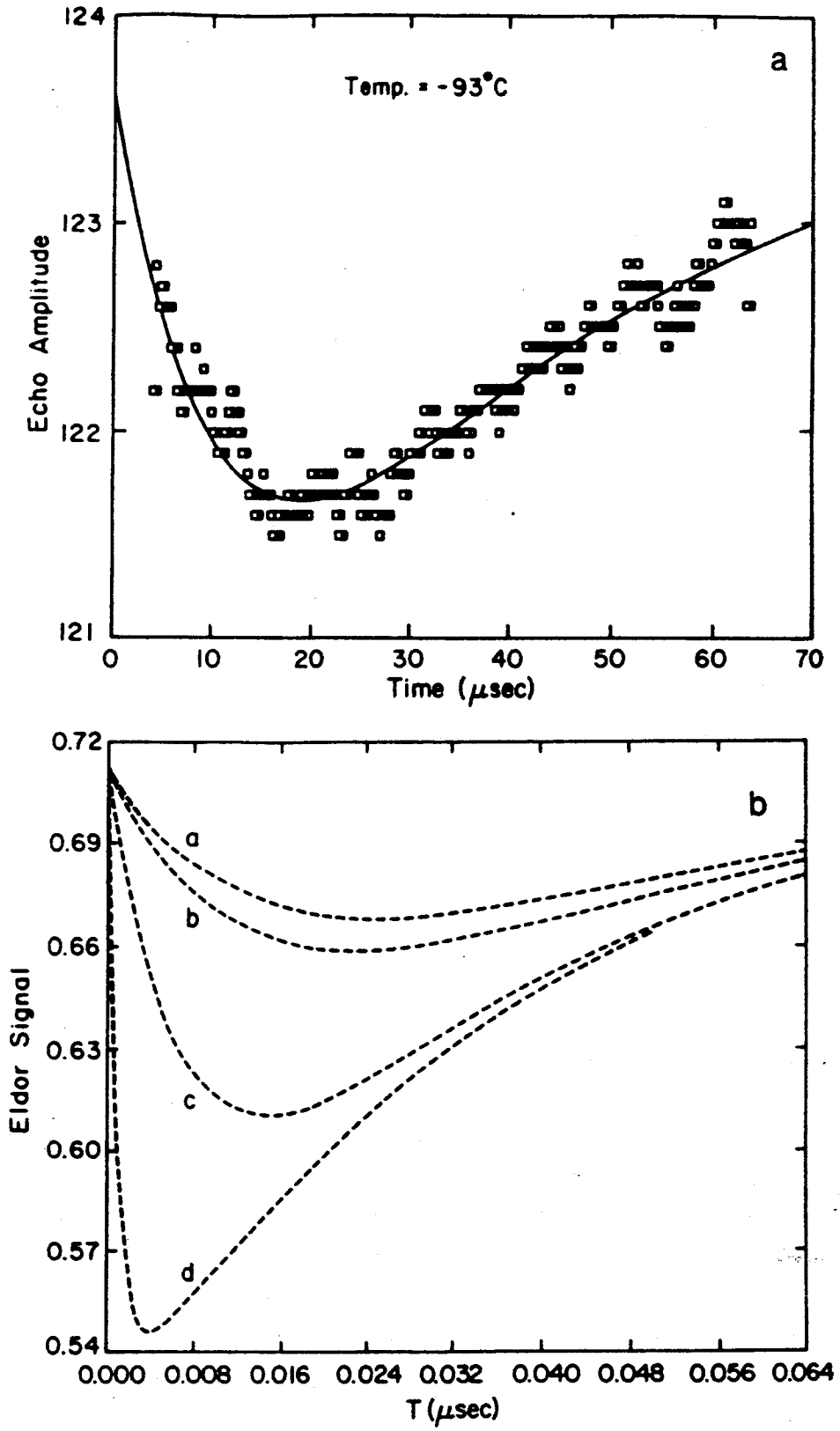

Fig. 15. (a) Experimental stepped-field ELDOR echo amplitude versus time between first π pulse and $\pi/2$ pulse for PD-Tempone in 85% glycerol/H_2O at -93°C. Solid line: Best two-exponential fit to data. [from Ref. 39] (b) Calculated ELDOR curves for slowly tumbling nitroxide. In sequence a-d orientation-independent nuclear spin flip rate increased, thereby increasing the ELDOR effect. [From Ref. 24].

The primary limitation of the original experiments (39) is a 1-2 μsec delay after stepping the field. We have redesigned this experiment so that two frequency sources (a klystron and a Gunn diode) feed separately pulsed signals to the travelling wave tube. This configuration allows one to pulse the pumping and observing regions with time delays of as little as 10-20 nsec. This arrangement is used in conjunction with a low Q cavity with an absorption half-width of 125 MHz which permits one to irradiate spectral regions separated by $\Delta H < 4.5$ mT. Such an experimental arrangement could be used to study possible exchange between ordered and disordered lipids or between fluid and immobilized lipids in oriented samples containing polypeptides or proteins (46). It can also be effectively used for studies of motional dynamics in the regions corresponding to fast motions (e.g. high water content liquid crystalline phases) where one may directly measure the electron spin, and cross-relaxation rates (35,38,47). This has been done with cw-ELDOR (48,49). However, the 2D-FT methods such as those that are described in Section 6 below are more powerful.

5. ELECTRON-SPIN ECHO ENVELOPE MODULATION (ESEEM)

An important application of ESE techniques enables one to obtain more detailed information about the location of spin probes. This may be achieved by studying the electron-spin-echo modulations (ESEEM) resulting from the dipolar interaction of the unpaired electron of the nitroxide group with deuterated (or protonated) sites. In particular, the use of these ESEEM for the study of site geometries has been utilized by Kevan and co-workers (50), and was applied by them to the study of doxylstearic acid spin labels in frozen micellar solutions of surfactants (51) with deuterated head groups, deuterated counterions, or deuterated terminal methyl groups. By measuring the ESEEM as a function of the location of the nitroxide group on the hydrocarbon chain, they were able to assess the location of the spin probe nitroxide group relative to the head group region. Also, by measuring the deuterium interactions from D_2O with the different labeled doxylstearic acids, they could investigate the degree of water penetration into the micellar systems.

The theory for ESEEM has been reasonably well developed and is summarized elsewhere in the volume. It enables the measurement of extremely weak electron-nuclear dipolar interactions such as exist between the unpaired electron of the nitroxide label and the deuterons (protons) on the nearby surfactants or D_2O (H_2O) molecules. Aside from measurements of modulation frequency which can be sensitive to the dipolar interaction, the deuterium (proton) modulation depth depends on the number of interacting deuterons and their average distance from the spin probe (or more precisely, their average dipolar interaction). Kevan and co-workers (51) used their estimate of the average numbers of surfactant head groups or counterions a spin probe interacts with to extract information on the relative distances of

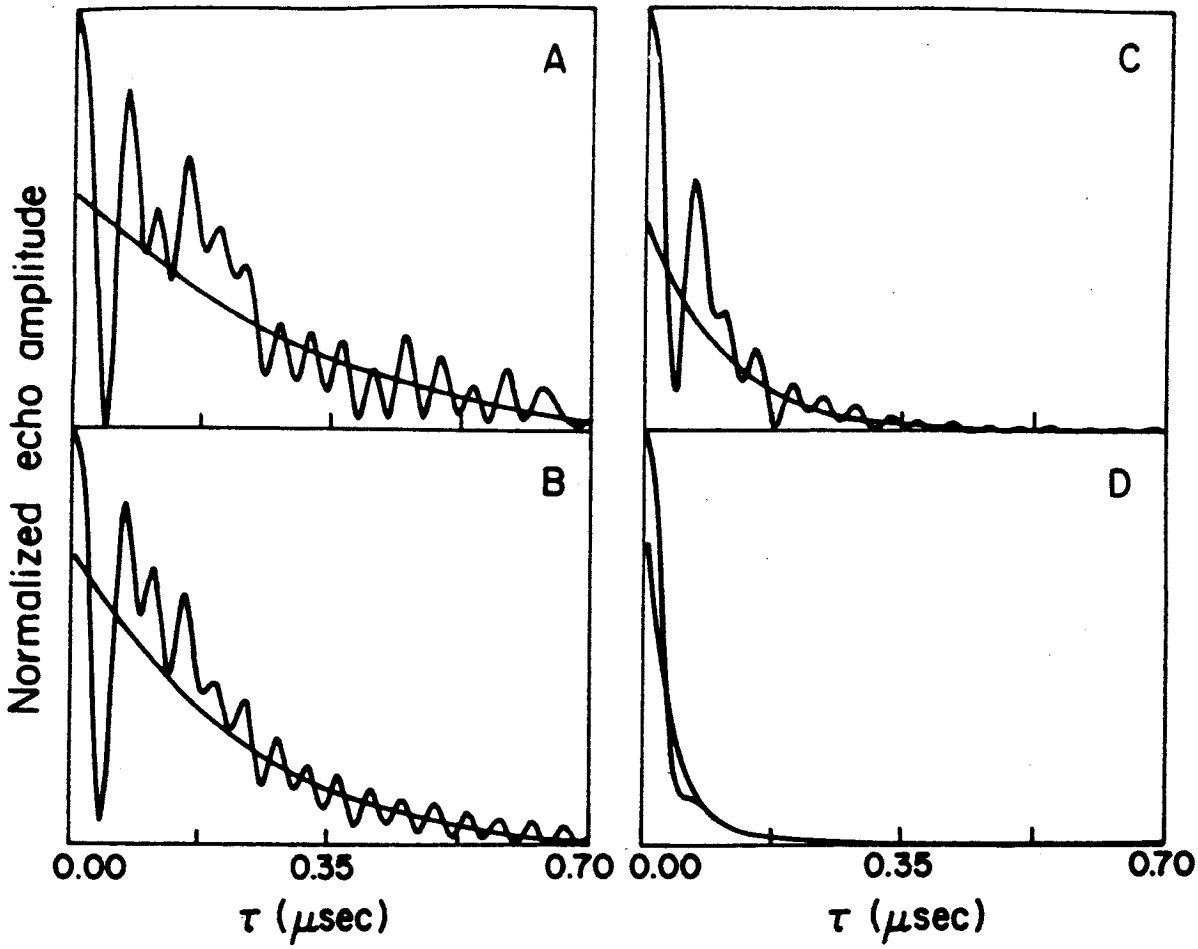

Fig. 16. Theoretical simulations of ESEEM patterns for a spin probe containing a single proton undergoing Brownian diffusion with rotational correlational times of (A) 3.6×10^{-5} sec, (B) 3.6×10^{-6} sec, (C) 3.6×10^{-7} sec and (D) 3.6×10^{-8} sec. Here $A_\perp$=0.325 mT, $A_\parallel$=0.65 mT, B_0=0.22 T. Superimposed are the best fits to $\exp[-2\tau/T_M]$ [From Ref. 23].

the spin-probe from the head-group region. They found that deuteron ESEEM is generally detectable for determining interaction distances less than 6 Å.

While ESEEM has primarily been used for structural studies, it is also possible to utilize them in the study of motional dynamics. In general, motion averages out the ESEEM. A general theoretical approach to the problem of how motion averages ESEEM has been developed (23,24). We show in Fig. 16 a theoretical computation illustrating how they become averaged out as the rotational motion speeds up from rigid-limit values.

We find in model experiments (24) that for PD-Tempone, where the ESEEM are due to the weak deuteron shf splittings, that the patterns change significantly for τ_R values ranging from about 10^{-4} sec to 10^{-7} sec, although residual effects may be seen for somewhat faster and slower motion (cf. Fig. 17). Note that the deuteron shfs is significantly smaller (e.g. $A_z \approx 100$ mG) than the ^{14}N hf term ($A_z \approx 3.0$ mT). Thus, it will be averaged out by motions that are considerably slower

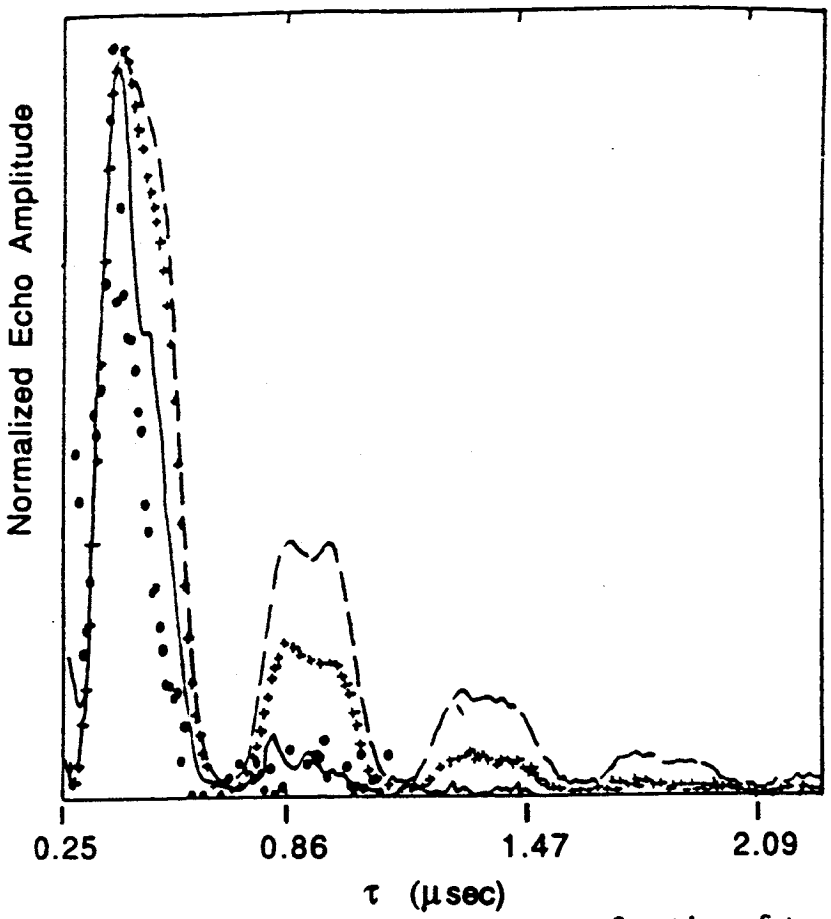

Fig. 17. Experimental $\pi/2$-τ-π-τ ESEEM patterns as a function of temperature, for PD-Tempone. Dots, -43°C; solid line, -55°C; crosses, -64°C; dashed line, -73°C. Solvent is 85% glycerol/H_2O. [From Ref. 24].

than required for normal ESE spectra. Effects from deuterons directly on PD-Tempone are averaged by any reorientation. Deuterons of the solvent can also cause ESEEM in the rigid limit (52), which would be averaged by the relative translation and rotation of solvent and solute molecules.

Another way of studying the ESEEM is to use a stimulated echo sequence: $\pi/2$-τ-$\pi/2$-T-$\pi/2$-τ and step out T for fixed τ. However, by varying the pulse interval τ, one can markedly affect the shape of the ESEEM. This effect has been called the suppression effect in solids (53). When these ESEEM are affected by motions, then studies as a function of both τ and T could be most useful.

We now address the question as to the relevance of ESEEM for 2D-ESE experiments. We recall that the T_2-type 2D-ESE experiments of MF required a small B_1 such that $\gamma B_1 \ll \Delta$ the inhomogeneous width (cf. Eqn. 5). However, it <u>also requires</u> that $B_1 \ll a_i/\gamma$, where a_i is the shf constant for the i^{th} deuteron (or proton) in order that ESEEM <u>not</u> be excited. In actual fact, it is only practical to achieve this inequality for <u>fully</u> protonated samples, so only such samples were used. On the other hand, if $B_1 > a_i/\gamma$, then the 2D-ESE experiments would include the effects of ESEEM, and in fact, one could map out how the ESEEM varies

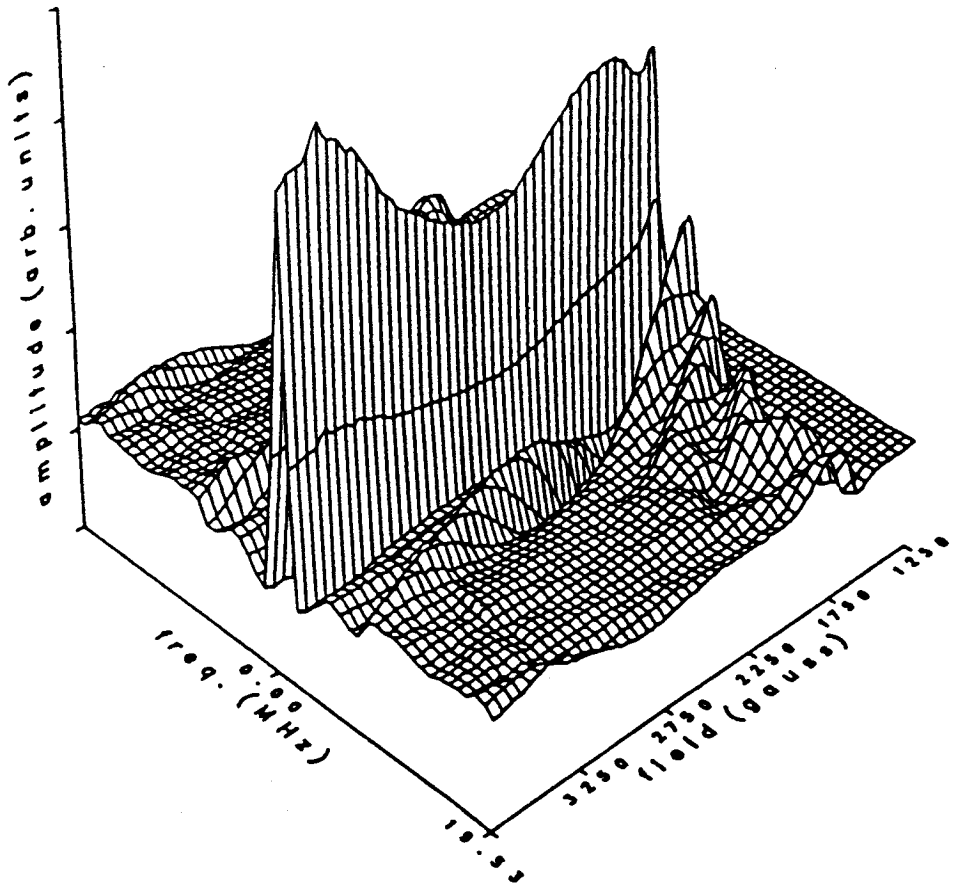

Fig. 18. 2D-ESE spectrum of ovotransferrin-carbonate containing Fe(III). [From Ref. 53].

across the EPR spectrum. This can be expected to enhance the interpretation of these patterns, both for structure and dynamics. We show such a 2D-ESE spectrum in Fig. 18, not for a nitroxide, but for ovotransferrin-carbonate containing Fe(III) (54). It dramatically demonstrates the sensitivity of ESEEM to position in the EPR spectrum (i.e. the field position).

Actually, special 2D techniques have been demonstrated to help one to unravel complicated ESEEM patterns (55-57). In fact, the work by Merks and de Beer (55,56) on two-dimensional echo spectroscopy for improving spectral resolution of ESEEM in solids was the first example of 2D-EPR. LPSVD methods should be useful in the analysis of the deuteron modulations. We show in Fig. 19 1D results obtained from the model system of PD-Tempone in deuterated glycerol/H_2O. In particular, we could distinguish six distinct frequencies with the aid of LPSVD. Thus LPSVD methods are likely to greatly enhance the sensitivity of related 2D studies, (cf. chapters by van Ormondt and by Norris).

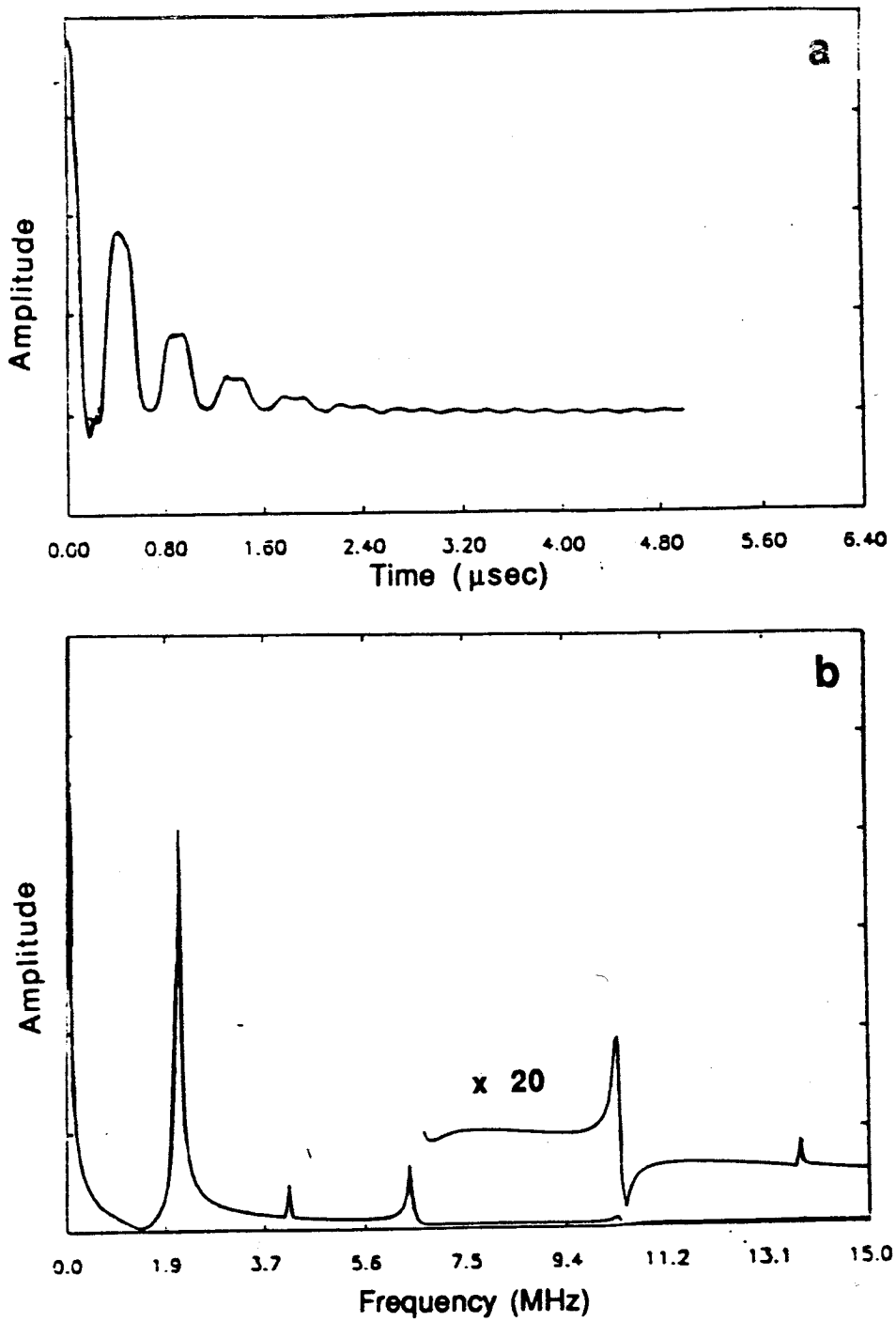

Fig. 19. ESEEM patterns of PD Tempone in 85% glycerol/H_2O at -80°C (a) Experimental data (dashed line) and LPSVD fit (solid line). (b) Fourier transform of LPSVD curve showing six spectral components.

6. TWO-DIMENSIONAL FOURIER-TRANSFORM EPR

6.1 Introduction and Motivation

Ernst and Anderson demonstrated that the response of an ensemble of nuclear spins to a pulse of polarized radiofrequency (rf) is equivalent to the slow-passage NMR spectrum (58). When a two level spin system is in thermal equilibrium, the -1/2 state is only slightly more populated than the +1/2 state. The slow-passage (unsaturated) NMR experiment is based on the well-known linear response theory wherein one excites nuclear spin transitions without significantly altering these thermal equilibrium spin state populations. This is accomplished with continuous rf irradiation at low power. In a high power pulsed NMR experiment the populations of +1/2 and -1/2 spin states can be rapidly equalized before the rf power is switched off. Fourier transform spectroscopy works because in the time following the rf pulse, the ensemble of coherently excited spins evolves in the complete absence of rf radiation. Linear response theory applies because there is no rf field during this free precession period. This means that Fourier transformation of the free precession signal (known as the free induction decay) generates the NMR spectrum that is obtained in the slow-passage experiment.

Jeener (59) first proposed the idea of two-dimensional correlation spectroscopy (2D-COSY). In 2D-COSY NMR the time correlation function of the magnetization is obtained by utilizing two or more closely spaced rf pulses. Ernst and co-workers (60) first demonstrated this concept utilizing two $\pi/2$ pulses in the basic 2D-COSY NMR experiment. Since that original experiment, 2D-NMR techniques have flourished (61). However, that potential had not been realized experimentally in EPR, because of the requirement that the entire spin Hamiltonian be "rotated" by the radiation field, an experiment substantially more difficult in EPR than in NMR.

In terms of Fourier spectroscopy, other distinctions between electron spins and nuclear spins are that the electron spins typically resonate at much higher (i.e. microwave) frequencies with much greater spectral widths, and they exhibit much shorter relaxation times. These properties have imposed certain limitations on the application of Fourier spectroscopic techniques to EPR. The generation of extremely narrow (5-10 nsec) microwave pulses necessary for Fourier transform EPR has only recently become practical. Digitizers with adequate sampling capability to record free induction decay signals of electron spins have also not been available until very recently. Now that such components are commercially available, the same techniques that were introduced to NMR beginning twenty years ago are being introduced to EPR. Simultaneously, Bowman and co-workers performed FT-EPR experiments of short-lived organic free radicals of spectral bandwidth ~ 40 MHz (62,63), and Gorcester and Freed performed FTEPR experiments on the broader (~90 MHz) spectra of nitroxide radicals (64) based on earlier considerations of Hornak and Freed (65). In a communication that followed shortly

thereafter, Gorcester and Freed first demonstrated 2D-SECSY and 2D-FT exchange EPR experiments on the same nitroxide radical samples (66). Since these initial demonstrations, there have been significant developments and improvements of 2D-FT-ESR instrumentation and methodology (67,68).

The principal application of 2D-FT-EPR demonstrated thus far is to the ELDOR experiment. As we have already discussed in Sect. 4.3, ELDOR requires the use of two excitation fields: one to modify the populations (the pumping field at frequency ω_p) and another to detect the response (the observing field at frequency ω_o) elsewhere in the spectrum. In the slow-passage ELDOR experiment, one typically keeps the two constant at a precise frequency difference, while sweeping the DC magnetic field B_0 through the entire spectrum. One could repeat this experiment in which the difference between pumping and observing frequencies is varied and thereby obtain a two-dimensional spectrum with $\gamma_e B_0$ on one axis and $\omega_o - \omega_p$ on the other. Such a data set can be manipulated to produce the two-dimensional spectrum as a function of $\omega_o - \gamma_e B_0$ and of $\omega_p - \gamma_e B_0$, which are the "natural variables" for interpreting the spectrum. Alternatively, such a procedure can be applied in the time-domain by utilizing the ST-ELDOR-echo method discussed above. Such experiments would be very time consuming and are typically not practical. However, such an experiment may be performed very efficiently with 2D-FT-EPR methodology. With 2D-FT-ELDOR (67), one obtains all of the combinations of pump and probe frequencies simultaneously in a single two-dimensional experiment! In fact, the matrix of 2D-ELDOR peak intensities is rather simply related to the matrix of transitions probabilities. Such an experiment can typically be performed in less than an hour, and analyzed in a few minutes.

The analysis of 2D experiments, whether NMR or EPR, typically involves 2D Fourier transformation of a two-dimensional time series, followed by phase corrections and numerical determination of volume integrals. LPSVD presents an alternative to Fourier analysis (69,70), and we do find that LPSVD may be very usefully applied to 2D-FT-EPR, (71). Also, we have found a variation of this technique that is customized to exploit many of the symmetries in 2D-FT EPR or NMR (71).

We now consider how the newly developed FT-EPR methods can improve and extend the range of 2D experiments on molecular dynamics. To date, this has been done for cases involving fast motional nitroxide EPR spectra, but the principles and methods can be extended to slow motions.

6.2 Spin-Echo Correlated Spectroscopy: (SECSY)

The 2D-FT analogue of our field-swept T_2-type 2D-ESE experiment may be referred to as spin echo correlation spectroscopy (66,68) (SECSY). The basic pulse scheme for SECSY is illustrated in Fig. 20. The SECSY experiment involves acquisition of the electron spin echo during the t_2 time period for a series of equally spaced values of t_1. The 2D-SECSY spectrum (Fig. 21) is obtained after

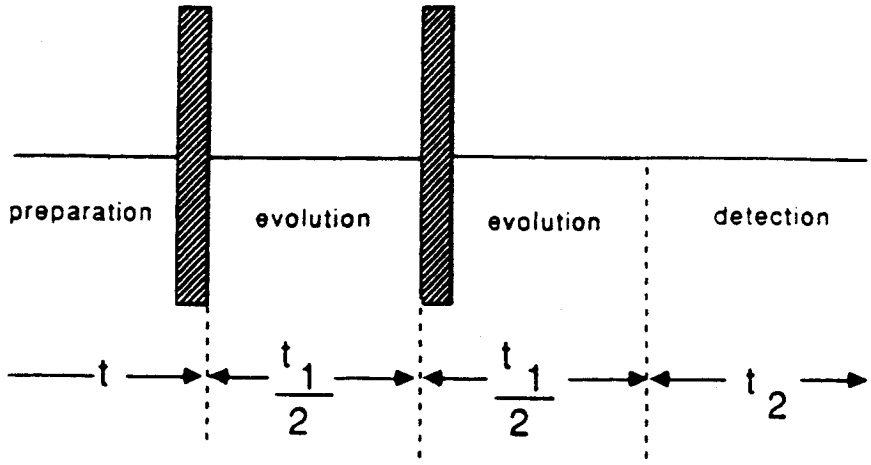

Fig. 20. SECSY pulse sequence. The homogeneous decay of the spin echo occurs during the evolution period t_1; the inhomogeneous decay occurs in the detection period t_2.

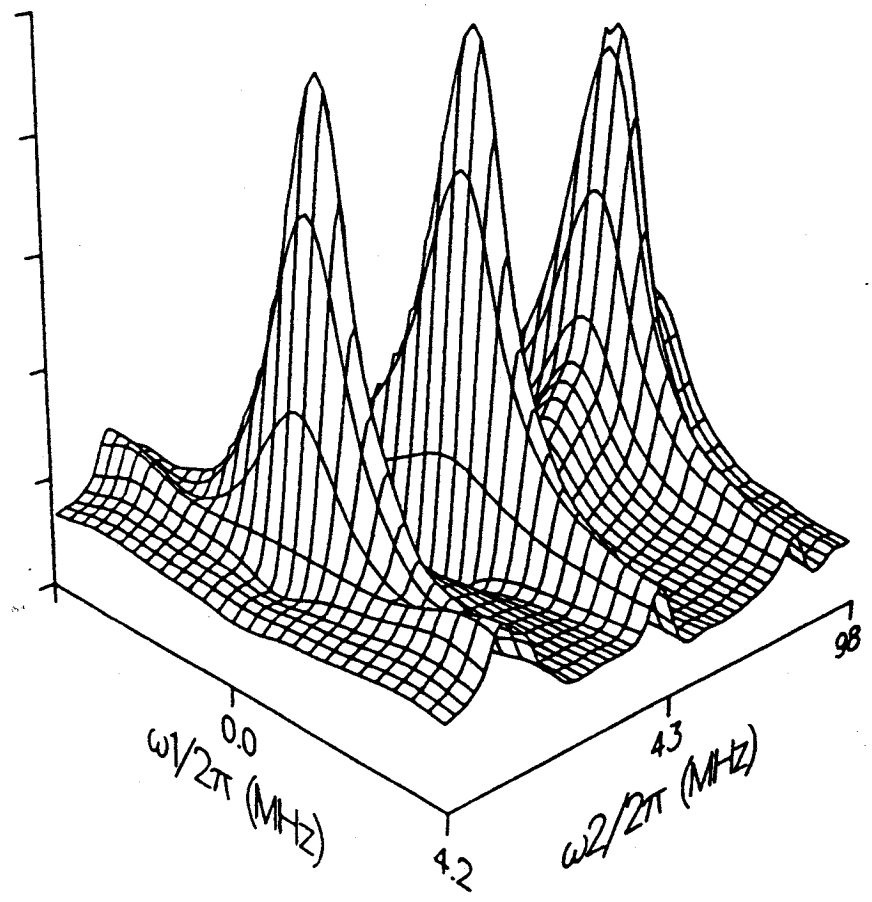

Fig. 21. SECSY spectrum of 1.17×10^{-3} M PD-Tempone in toluene-d_8 at 22°C. $T_2^* \simeq 75$ nsec; $T_2 \simeq 174$ nsec; 0.86 nsec resolution in t_2 providing 256 complex data points, each the average of 2048 transients. Time resolution in t_1 is 12 nsec; pulse width is 15 nsec; acquisition time 60 minutes. [From Ref. 66]

making a small first-order phase correction in ω_2 and a linear amplitude correction. One observes the inhomogeneously broadened three-line hf patternalong ω_2 and the Lorentzian homogeneous lineshapes along ω_1. [The DC magnetic field homogeneity was destroyed to suppress the FID from the second $\pi/2$ pulse. This would not be necessary for a slow-motional spectrum (29,30,36)].

The advantage of SECSY in comparison to field-swept 2D-ESE is the order-of-magnitude shorter data acquisition time. In addition, SECSY has the potential for observing (weak) cross-correlations which cannot be observed with techniques using narrow band excitation.

The theory for this experiment (67,68) is very similar to that of field-swept 2D-ESE (cf. Sect. 3). One obtains:

$$s'(t_1,t_2) = \sum_{k,m} c_{km}\exp(-\Lambda_k t_2)\ \mathrm{Re}\ \sum_j b_{mj}\exp(\Lambda_k-\Lambda_j^*)t_1/2] \qquad [17]$$

for the pulse sequence in Fig. 20, where

$$c_{km} = \sum_n U_n O_{o,nk} V_m O_{o,mk} \qquad [18]$$

and

$$b_{mj} = \sum_l O_{o,mj}^* V_j^* O_{o,lj}^* U_l \qquad [19]$$

We have neglected electron spin echo envelope modulation (ESEEM) arising from cross-polarization of nuclei via the hf tensors (but see Sect. 5). These terms are important in the slow-motional regime.

The V_j give the correction for variation of effective B_1 across the spectrum for the "$\pi/2$ pulse," i.e. the j^{th} DSP resonating at angular frequency ω_j experiences an effective rotation that depends on $\omega_j-\omega$ (with ω the irradiating frequency) and on B_1 (65,67,68,72). In comparing Eqn. [17] with Eqn. [1], we note that the a_{kj} of Eqn. [1] is now replaced by $\sum_m c_{km}b_{mj}$. Also U is the vector of (appropriately averaged) spin transition moments.

After Fourier transformation with respect to t_1 and t_2 we obtain

$$S'(\omega_1,\omega_2) = \sum_{k,m} c_{km}\ \frac{1}{i\omega_2-\Lambda_k}\ \ \mathrm{Re}\sum_j b_{mj}\ \frac{1}{i\omega_1-\frac{1}{2}(\Lambda_k+\Lambda_j^*)} \qquad [20]$$

Thus inhomogeneous broadening is removed along the ω_1 axis.

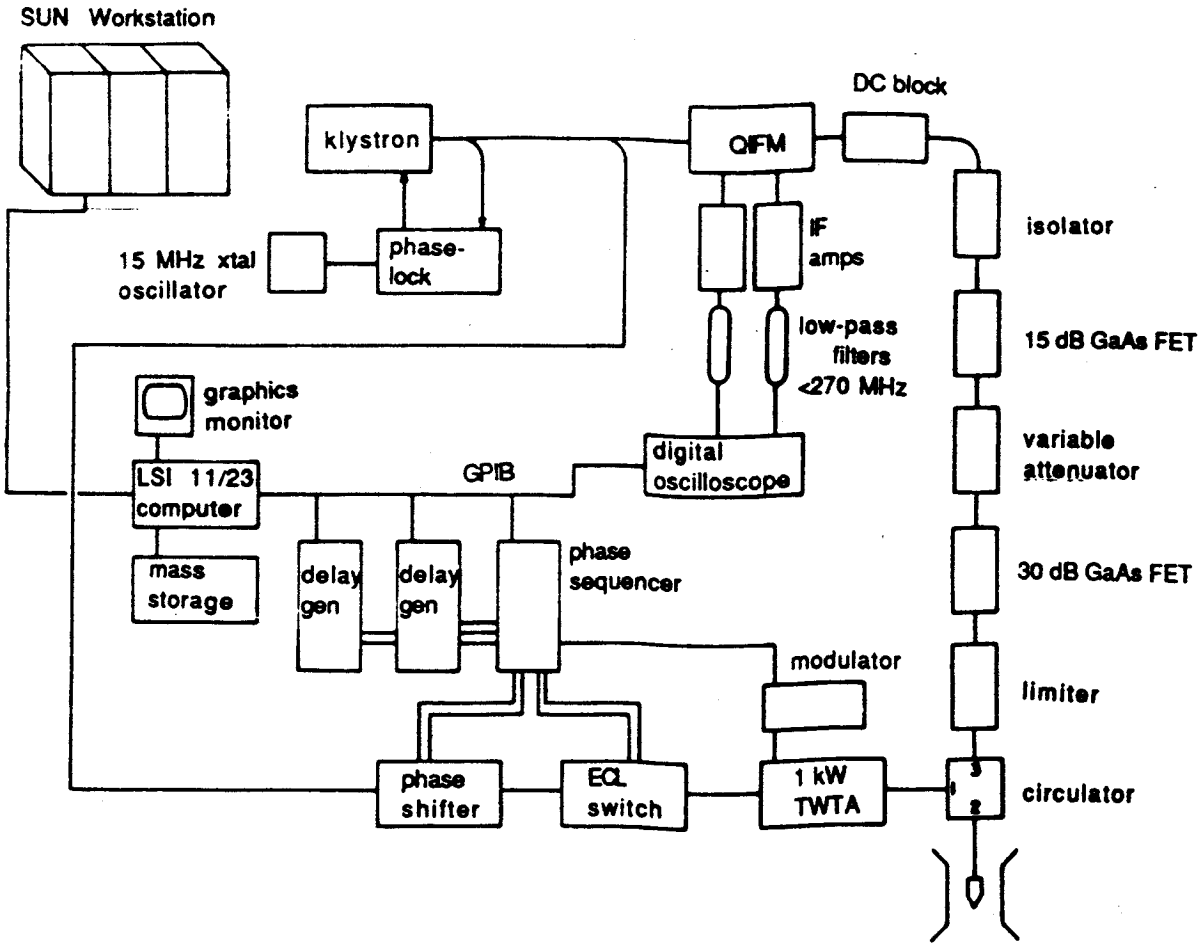

Fig. 22. Block diagram of spectrometer used for 2D-FT-EPR experiments.

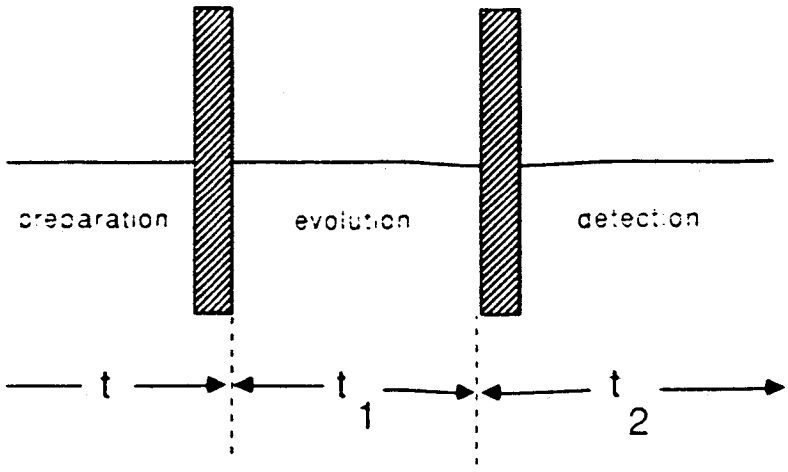

Fig. 23. 2D-COSY pulse sequence.

A comparison of Eqn. [20] with Eqn. [4] shows that this full FT method provides both the in-phase and quadrature components with respect to ω_2. They are obtained from the two arms of the quadrature detector. It is also possible to obtain the out-of-phase part of the signal with respect to ω_1. First, let us refer to the pulse sequence yielding Eqn. [20] as: $(\pi/2)_x$ - $(\pi/2)_x$, where the subscript x implies rotation of the spins by the microwave radiation along the rotating x-axis. Then the out-of-phase part of the signal with respect to ω_1 is obtained by phase shifting the first $\omega/2$ pulse by 90°, which we then write as a $(\pi/2)_y$ - $(\pi/2)_x$ sequence. It yields $S''(\omega_1,\omega_2)$ which is given by Eqn. [20] but with the real part of the expression in curly brackets replaced by its imaginary part. We shall refer to this approach as the 2D phase quadrature scheme.

An illustration of the principal features of our 2D-FT-EPR spectrometer is shown in Fig. 22.

6.3 Correlation Spectroscopy (COSY)

The previous method was based on detection of the echo signal. We now turn to FT-EPR experiments which are based upon detection of the free-induction decay (FID).

Two-dimensional correlation spectroscopy (2D-COSY) in its various forms has gained widespread use in NMR as a method of observing coherence transfer between coupled spin transitions. The pulse sequence $\pi/2$-t_1-$\pi/2$-t_2 constitutes the simplest of the COSY experiments and is used in NMR in the separation of scalar interactions (60,61). A COSY-EPR spectrum is obtained in much the same manner as for NMR; the basic pulse scheme is illustrated in Fig. 23. The preparation period consists of a $\pi/2$ pulse to generate the initial transverse magnetization components. Free precession of the magnetization occurs during the evolution period of duration t_1 during which the components become amplitude encoded according to their precessional frequencies in the rotating frame. The FID is recorded during the detection period of duration t_2, which begins with the final $\pi/2$ pulse. For each t_1 the FID is collected, then the phase of the first pulse is advanced by 90°, and a second FID is collected. These two signals depend on terms oscillatory in t_1 that are in phase quadrature, i.e. the 2D phase quadrature scheme. The oscillatory behavior in t_1 is illustrated in Fig. 24 after Fourier transforming one of these signals with respect to t_2 only. Two-dimensional complex Fourier transformation generates a spectrum over the two frequency variables, ω_1 and ω_2.

This two step phase alternation sequence yields the required frequency discrimination in ω_1, and it provides the phase information necessary for the pure absorption representation of the 2D spectrum (73). In order to cancel "images" resulting from imperfections in the quadrature detector, (cf. Fig. 22), we combine this two step procedure with the four step CYCLOPS image cancellation

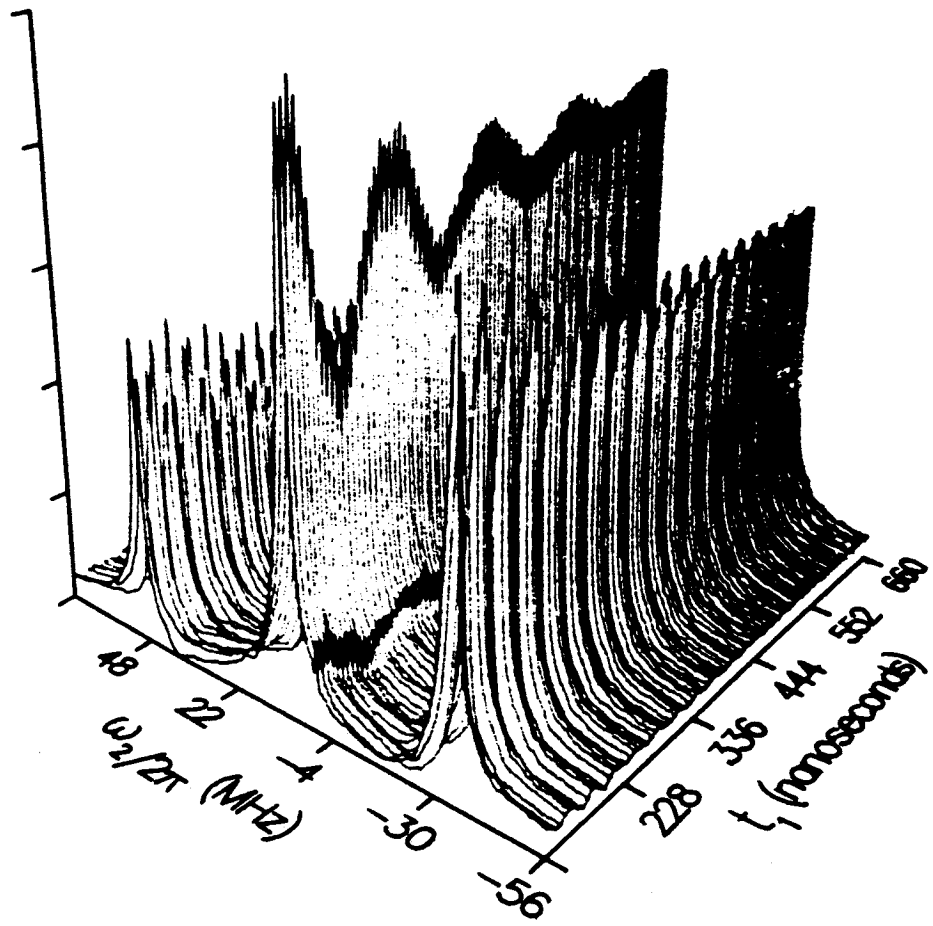

Fig. 24. 2D-COSY-EPR spectrum of 5.1×10^{-4} M PD-Tempone in toluene-d8 prior to FT in the t_1 domain in order to show the oscillatory behavior in t_1 (cf. Fig. 25 for a fully transformed 2D spectrum).

method (74) to obtain a sequence consisting of eight steps as described elsewhere (67,68). A COSY-EPR spectrum of 5×10^{-4} M PD-Tempone in toluene-d_8 obtained in this manner is shown in Fig. 25. Resonances at positions for which $\omega_1=\omega_2$ will be referred to in the standard fashion as autopeaks, because they represent auto-correlations. Cross-peaks representing cross-correlations are not found in the spectrum of Fig. 25 because the contributions of the electron-electron dipolar and chemical or Heisenberg exchange interactions are too weak. Such mechanisms can induce "off-diagonal" relaxation between the different transitions (47,74). Additional peaks at positions for which $\omega_1=0$ arise because of electron spin flips during the evolution period; these peaks are referred to in the standard manner as axial peaks (60,61).

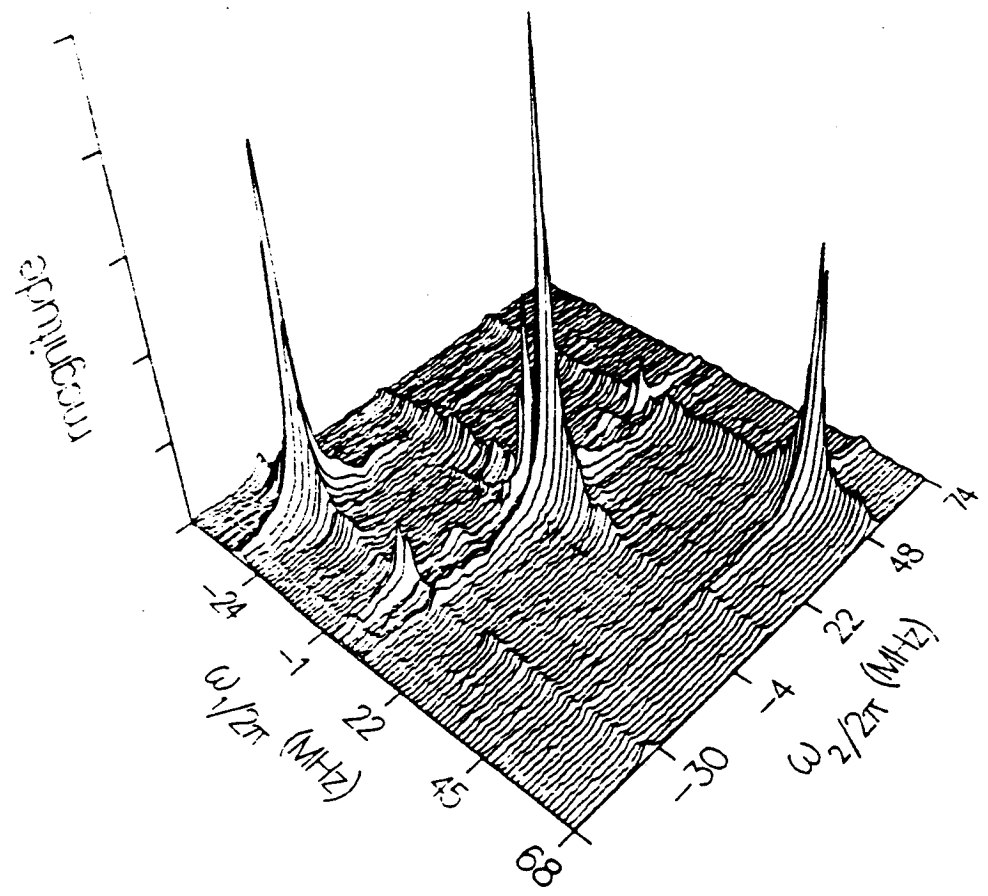

Fig. 25. Absolute value 2D-COSY-EPR spectrum of 5.1×10^{-4} M PD-Tempone in toluene-d_8 at 21°; τ_p=15.5 nsec; Δt_1=3.9 nsec; 90 samplings in t_1; eight step phase alternation sequence with 30 averaged FID per step; dead time in t_2 of 100 nsec; dead time in t_1 of 120 nsec; acquisition time 10.6 minutes. [from Ref. 67].

6.4 2D-ELDOR

We now describe the 2D-FT experiment that displays the effects of MT. More precisely, it is a way of performing ELDOR but with only a single frequency source! The spectral band produced by a finite pulse is coherently related, and this is the basis for the power of the technique. 2D-ELDOR involves a procedure similar to that of simple COSY except that three $\pi/2$ pulses are applied in the sequence $\pi/2$-t_1-$\pi/2$-T-$\pi/2$-t_2 with the mixing time T being held constant. The application of this sequence (in NMR) to the study of chemically exchanging species was first illustrated by Jeener et. al. (75). The basic pulse scheme for 2D-ELDOR is illustrated in Fig. 26. The preparation period consists of a $\pi/2$ pulse to generate the initial transverse magnetization. The phase of this pulse determines the phase of the amplitude modulation that results from the "frequency labeling" during the subsequent evolution period of duration t_1 as described above for the COSY-EPR experiment. The second $\pi/2$ pulse marks the beginning of the mixing period wherein the longitudinal magnetization components associated with

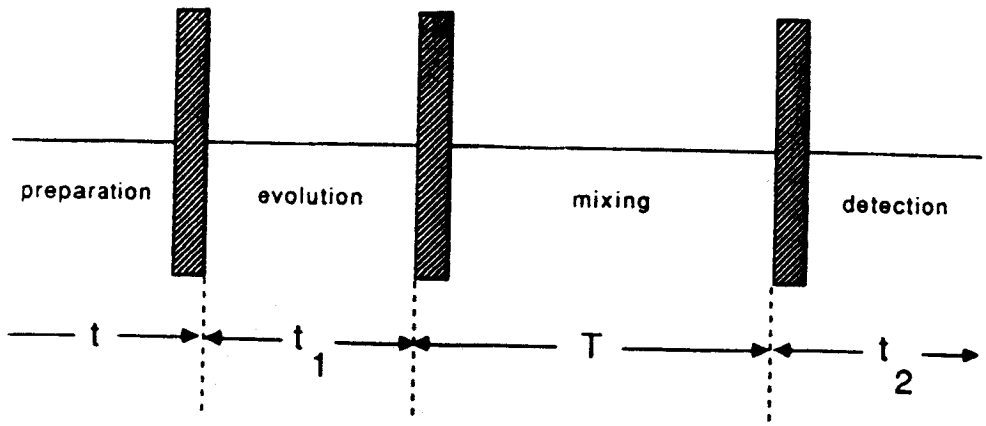

Fig. 26. 2D-ELDOR pulse sequence, involving four time periods: preparation, evolution, mixing, and detection. After the preparation period, a $\pi/2$ pulse generates the initial transverse magnetization. "Frequency labelling" occurs during the evolution period t_1. The second $\pi/2$ pulse starts the mixing period wherein the longitudinal magnetization components associated with each hf line can be exchanged with components having different precessional frequencies. When the magnetization is rotated into the x-y plane for detection, components initially precessing with angular frequency $\omega_1=\omega_a$ will, to the extent that magnetization transfer has occurred during mixing, precess with new angular frequency $\omega_2=\omega_b$.

each hf line can be exchanged, thereby mixing components carrying different precessional-frequency information (i.e. MT occurs). Thus, after rotating this magnetization into the x-y plane for detection by the third $\pi/2$ pulse, components initially precessing with angular frequency $\omega_1=\omega_a$ will (to the extent that MT occurred by exchange curing the mixing period) precess with new frequency $\omega_2=\omega_b$. As in the COSY-EPR experiment, the pulse sequence is repeated for a series of equally spaced values of t_1, where for each t_1 the FID is collected and then the phase of the preparation pulse is advanced by 90°, followed by collection of a second FID.

A 2D-ELDOR spectrum of 1×10^{-3} M PD-Tempone in toluene-d_8 (67) is shown in Fig. 27 with the corresponding contour map in Fig. 28. Magnetization transfer induced by Heisenberg spin exchange (HE) during the mixing period gives rise to cross-correlations and hence to the appearance of cross-peaks (66-68). The cross-peaks in Fig. 27 have the characteristics predicted for an exchange process, viz. there are comparable cross-peaks between all pairs of auto-peaks. This arises because HE has no nuclear spin selection rules. Measurement of the relative intensities of autopeaks and cross-peaks gives a direct determination of the Heisenberg exchange rate ω_{HE} (cf. Sect. 6.5).

Quantitative determination of exchange rates with 2D-ELDOR is complicated by the presence of unwanted coherences which add intensity only to the autopeaks of a motionally narrowed 2D spectrum, and in the slow-tumbling regime to the

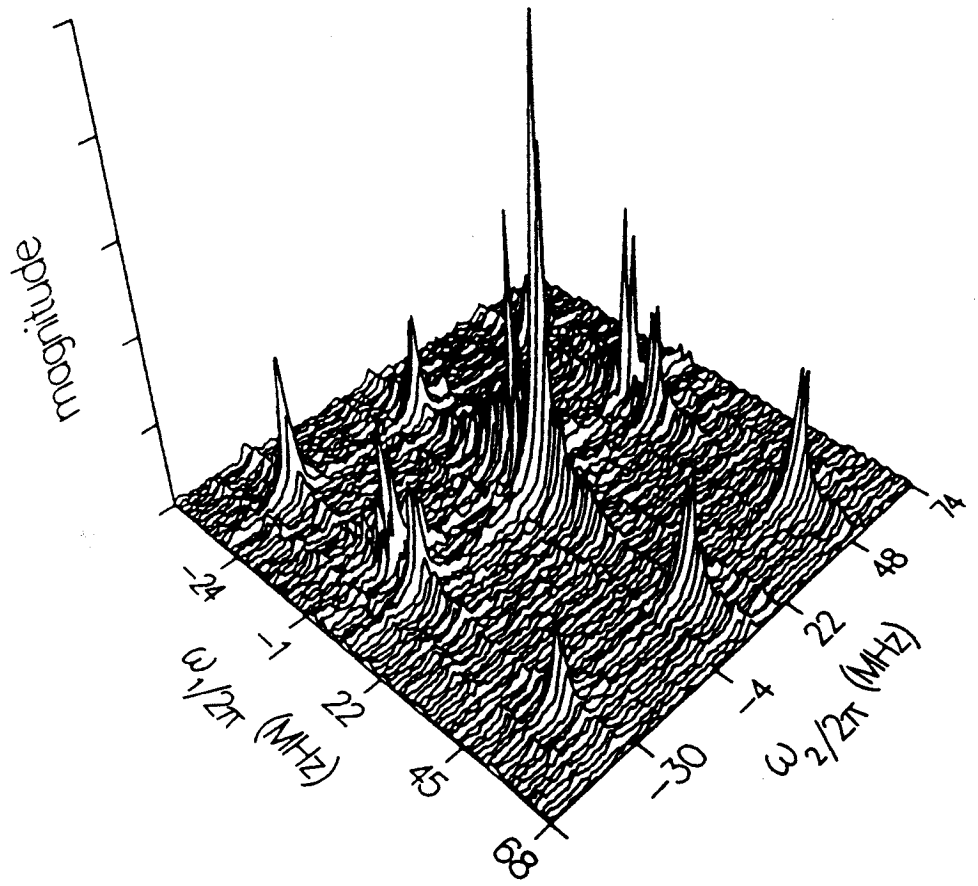

Fig. 27. Absolute value 2D-ELDOR spectrum of 1.17×10^{-3} M PD-Tempone in toluene-d_8 at 21°; τ_p=15.2 nsec; Δt_1=6 nsec; Δt_2=3.9 nsec; 90 in t_1; 16 step phase alternation sequence with 30 averaged FID per step; dead time in t_2 of 100 nsec; dead time in t_1 of 120 nsec; mixing time T=3.10×10^{-7} sec; 256 complex data points per FID extending to 1 μsec; acquisition time 27 minutes. [From Ref. 67].

cross-peaks as well. This phenomenon, known as transverse interference (76), arises from transverse magnetization following the first $\pi/2$ pulse which freely precesses for the rest of the sequence and interferes with the FID recorded during the detection period. A two step phase alternation sequence has previously been suggested for the cancellation of transverse interference (76). We can combine this sequence with our eight step 2D image cancellation sequence to obtain a sixteen step procedure tabulated elsewhere (66). However, we have discovered a more compact phase alternation sequence for 2D-ELDOR which achieves the same result as the sixteen step sequence but requires only eight steps. It is also tabulated elsewhere (66).

The 2D-ELDOR spectra of 1×10^{-3} M PD-Tempone in toluene-d_8 were recorded with the 16 step phase alternation sequence for four different mixing times. The ω_{HE} were determined by comparison of autopeak and cross-peak magnitudes (e.g. volume)

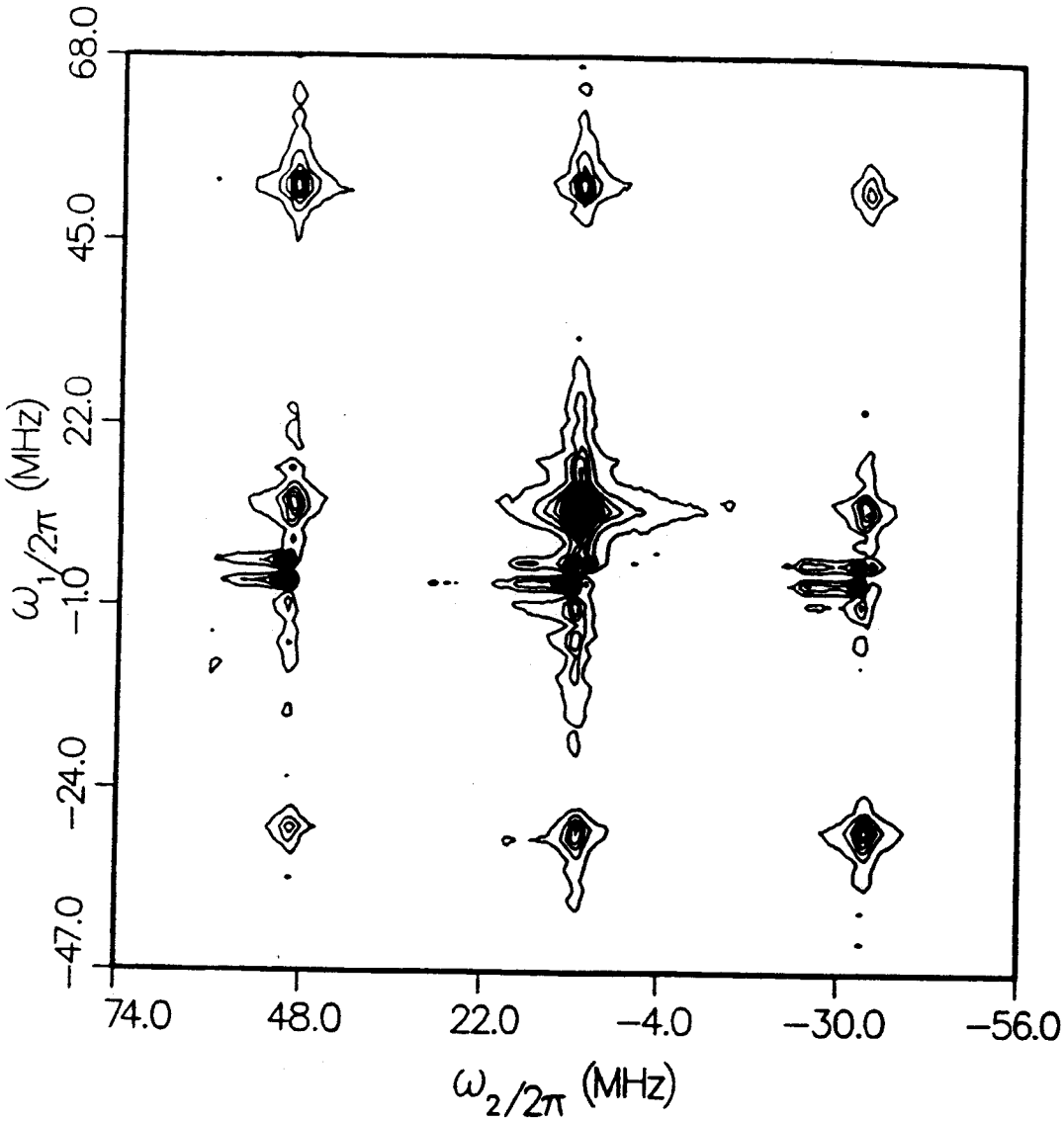

Fig. 28. 2D-ELDOR contour map of spectrum of Fig. 27. Residual axial-peaks appear as doublets centered on the line ω_1; the observed splitting is an artifact of the baseplane correction described in the text [From Ref. 67].

in each of these spectra according to the theory summarized below. These results could be compared to an ESE study in which six different concentrations of PD-Tempone in toluene-d_8 were used, and T_2 (M_I=0) was determined for each by fitting the ESE envelope to a single exponential (67). The exchange rate determined by ESE corresponds to the rate constant $\omega_{HE}/C=k_{HE}=3.63 \pm 0.63\times10^9$ M^{-1} sec^{-1}. The result is in agreement, within the experimental uncertainty, with the value determined by 2D-ELDOR (cf. Fig. 28), corresponding to $k_{HE}=3.97 \pm 0.43\times10^9$ M^{-1} sec^{-1}.

The 2D-ELDOR technique constitutes a direct observation of Heisenberg exchange on a single sample, whereas the ESE technique is somewhat indirect; that is, one usually fits T_2^{-1} to a linear dependence on concentration, but this is not always valid (77,-79). Electron-electron dipolar (EED) relaxation between probe molecules can also contribute to the observed T_2 in a concentration-

dependent fashion. EED is "ELDOR active" (47) but its presence is reflected relatively more substantially in the T_2^{-1}, hence also in the widths with respect to ω_1 and ω_2 of the 2D-ELDOR resonance lines. This allows for discrimination between HE and EED in the 2D-ELDOR experiment; (EED was not important in this experiment in a nonviscous solvent [77,80]). Also, we note that in an ELDOR experiment the sensitivity to ω_{HE} depends upon the ratio ω_{HE}/W_e (where W_e is again the electron spin-flip rate), whereas in a T_2 experiment it depends upon $\omega_{HE}T_2(0)$, where $T_2(0)$ is the concentration-independent T_2), so that when $W_e \ll T_2(0)^{-1}$, as is frequently the case, the ELDOR experiment would be the more sensitive to ω_{HE}. In this connection, one should note that whereas cw ELDOR only yields ratios such as ω_{HE}/W_e, time domain ELDOR, such as 2D-ELDOR, yields the relaxation rates directly (37,38,47,81).

It is possible to use LPSVD methods to facilitate accurate projection of 2D absorption lineshapes and to suppress certain artifacts that appear in 2D-ELDOR spectra. For this purpose we have developed a new linear predictive technique, based on LPSVD (71), which models two-dimensional time series obtained in COSY type experiments entirely in the time domain, i.e. without Fourier transformation. This new application of complex valued linear prediction facilitates the projection of 2D absorption lineshapes as well as the rejection of residual axial peaks and much of the noise. We applied 2D linear prediction to the data set leading to Fig. 27. Projection of pure absorption lineshapes was performed in both time domains. Extrapolation in t_1 eliminated artifacts caused by t_1 truncation and enabled a more accurate determination of baseplane offset. In Fig. 29 we illustrate the LPSVD result obtained after eliminating components for which $|\omega_1/2\pi| < 3$ MHz (i.e. narrow reject filtering of axial peaks); note the considerable improvement in signal/noise ratio. The volume integral of each 2D absorption line was measured by numerically integrating in the ω_2 domain and summing the results over the discrete values of ω_1. Estimation of the Heisenberg exchange rate from ratios of volume integrals with the use of Eqn. [44] gives the result $k_{HE}=3.92\times10^9\ M^{-1}\ sec^{-1}$, in good agreement with the result obtained from Fig. 27.

In the experiment of Fig. 27, we have chosen a sample and temperature for which nuclear spin relaxation is very small (80). If the nuclear spin relaxation rate $2W_n$ constitutes a non-negligible source of spin relaxation, then a more general analysis of the 2D-ELDOR experiment is required. Note that W_n arises from rotational modulation of the electron nuclear dipolar interaction involving the ^{14}N nuclear spin, and it is an important parameter in the study of molecular dynamics (47,80). The 2D-ELDOR spectrum of PD-Tempone in the liquid crystal S2 (Fig. 30) is an example of a 2D-ELDOR experiment in which nuclear spin relaxation cannot be neglected. In this case Heisenberg exchange does not play a significant

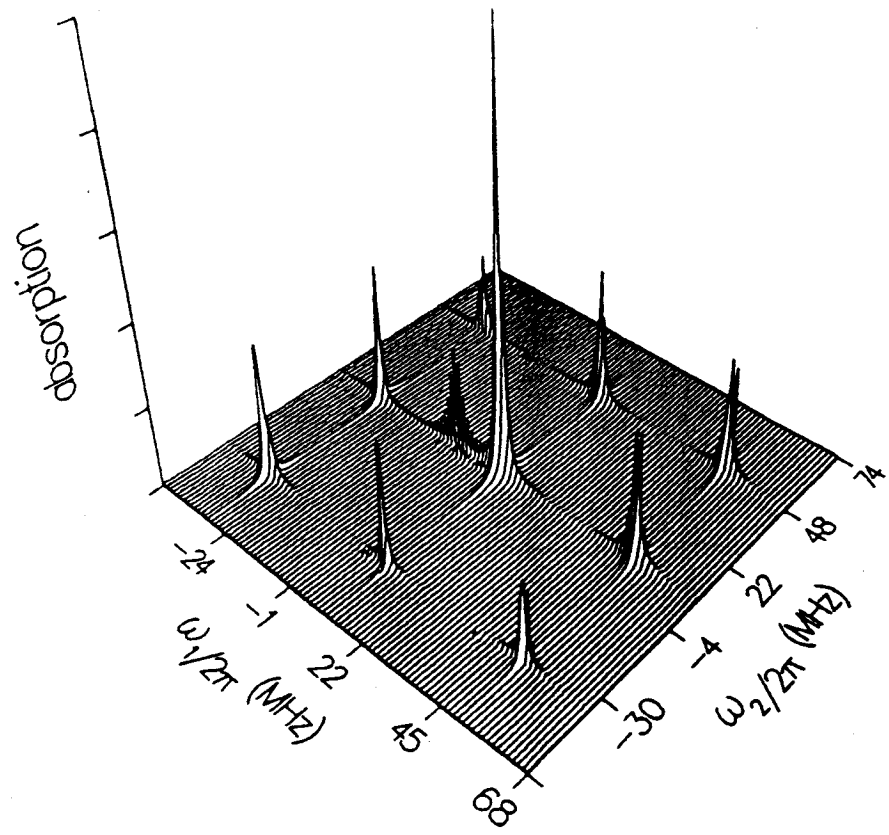

Fig. 29. LPSVD projected pure 2D absorption representation of the spectrum of Fig. 27. M=24, K=6 in the t_1 domain, M=60, K=12 in the t_2 domain; where M is the number of linear prediction coefficients and K is twice the number of signal peaks. The broad peak near the center of the spectrum (at $\omega_1/2\pi$=-8 MHz) has zero width in ω_2 (hence zero volume) and is apparently an artifact of the computation. [From ref. 71].

role in the transfer of magnetization. This is apparent by inspection of the contour map (Fig. 31) associated with the spectrum of Fig. 30 which shows no significant cross-peaks connecting the outer hf lines. This is consistent with a nuclear spin relaxation mechanism where $\Delta M_I=\pm 1$, e.g. from the electron-nuclear dipolar interaction. The spectrum of Fig. 30 yielded the relaxation rate $2W_n=4.25 \pm 0.25\times10^5$ sec^{-1}. The quantitative accuracy of this technique for determination of W_n was demonstrated by comparison with stimulated echo (SE) results.

The quantitative agreement of 2D-ELDOR and SE methods raises the question: why perform 2D-ELDOR experiments, which are significantly more sophisticated than stimulated echoes, when SE experiments yield the same results? The answer to this question is two-fold. First, note that the SE experiment required the use of substantially larger sample volumes in order to obtain adequate sensitivity.

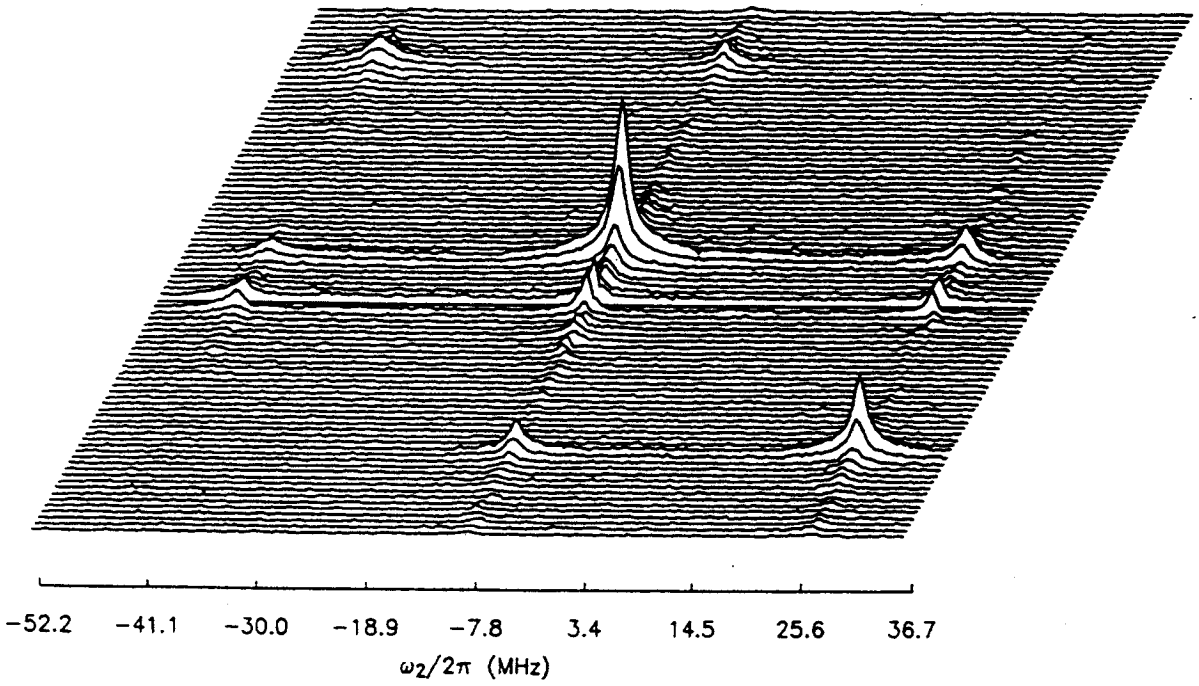

Fig. 30. Absolute value 2D-ELDOR spectrum of 2.05×10^{-3} M PD-Tempone in liquid crystal S2 at 35.5 ± 0.5°C obtained with the director aligned parallel to B_0; τ_p=12 nsec; Δt_1=7 nsec; Δt_2=5.86 nsec; 128 samplings in t_1; eight step phase alternation sequence with 128 averages per step; dead time in t_1 of 66 nsec; dead time in t_2 of 145 nsec; mixing time $T=5.48\times10^{-7}$ sec; 256 complex data points per FID extending to 1.5 μsec; acquisition time 51 minutes. [From Ref. 72].

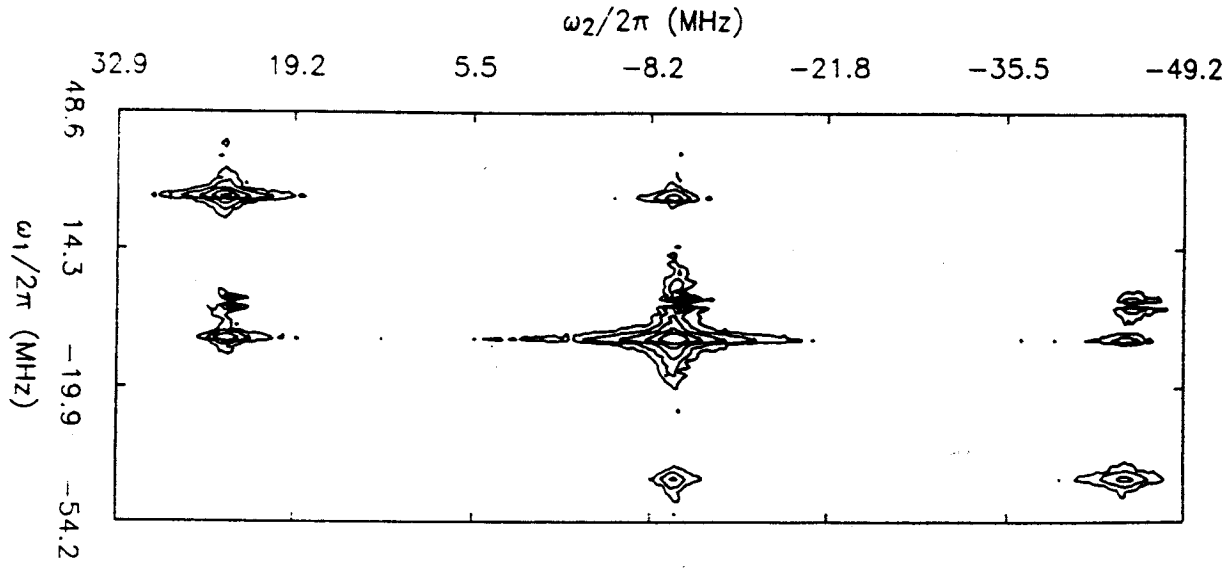

Fig. 31. 2D-ELDOR contour map of the spectrum of Fig. 30. Note the absence of cross-peaks connecting the two outer hf lines, indicative of an ^{14}N nuclear spin relaxation mechanism, [From Ref. 72].

This is because the stimulated echoes observed in these sytems are about one order of magnitude smaller in signal voltage than the FID's recorded in the 2D-ELDOR experiment. Second, it is important to compare the methods of analysis required for the two types of data. In the case of 2D-ELDOR, a direct determination of W_n and ω_{HE} is obtained by comparison of peak volumes (cf. below), whereas for SE a least-squares fit to a sum of exponentials is required. Unless extensive signal averaging is performed, the least-squares procedure will be susceptible to error, particularly in the case of $W_n/W_e \ll 1$ or $\omega_{HE}/W_e \ll 1$. This underscores the need for three SE experiments, each performed at a different hf line. The proper set of SE experiments therefore requires 1) substantially longer data acquisition times than 2D-ELDOR; 2) greater minimum number of spins than 2D-ELDOR; 3) a measurement of spectrometer dead-time; and 4) a five parameter nonlinear least-squares fitting procedure. The SE experiment is nevertheless complementary to 2D-ELDOR, in that it provides a fairly accurate measurement of W_e which is not obtained in a single 2D-ELDOR experiment, but it can be obtained from 2D-ELDOR results as a function of mixing time T, as discussed below, (or by studying "type E" axial peaks, cf. below and Ref. 68). [Note also, that these comments about SE apply also to saturation recovery (SR) discussed by Hyde in this volume. In SE, however, the spins are first prepared in a well-defined state prior to studying their time evolution. Also, in SR one observes not an echo (nor an FID), but a low power cw signal].

Recently, a detailed study was completed utilizing 2D-ELDOR and ESE to clarify more precisely the nature of rotational motion in a liquid crystalline smectic (lamellar) phase (72). This work demonstrates the power of the new methods in view of the more extensive and more accurate data they provide.

The nuclear spin flip rate $2W_n$ is shown in Fig. 32 as a function of temperature, and it is readily fit with an activation energy E_a=10.3 ± 0.3 kcal/mole. A typical angular dependent result for W_n is shown in Fig. 33 for T=20° C. Here θ is the angle between nematic director and magnetic field. Now W_n is proportional to the (electron-nuclear dipolar) spectral density $J_1^{DD}(\omega_e)$ for θ=0 (47). However, the angular dependence of $2W_n$=$J_1^{DD}(\omega_e,\theta)$ provides one with additional spectral densities as a function of θ:

$$J_M^{DD}(\omega,\theta) = \sum_{m'=-2}^{m} |d^{(2)}_{M,M'}(\theta)|^2 \, J_{M'}^{DD}(\omega,\theta=0) \qquad [21]$$

where the $d^{(2)}_{M,M'}(\theta)$ are the reduced Wigner rotation matrix elements of rank two. The use of Eqn. [21] in EPR requires that the spin probe is not highly

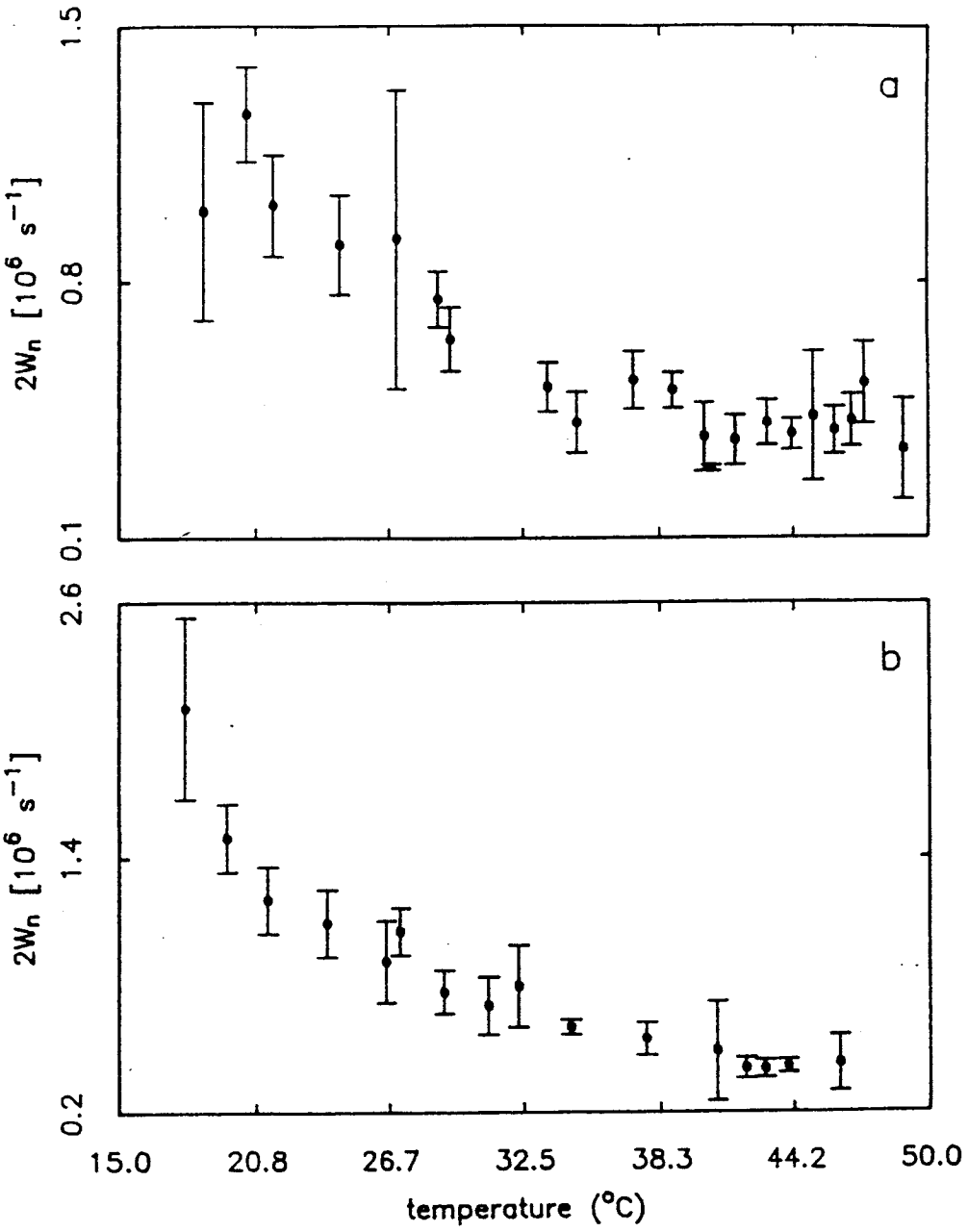

Fig. 32. Temperature dependence of nuclear spin flip rate W_n for PD-Tempone in the liquid crystal S2 at orientation (a) θ=0°; (b) θ=90°. [From Ref. 72].

ordered (82). Here M represents a quantum number for projection of the spin axes in the director frame. Eqn. [21] yields three basic quantities: $J_0^{DD}(\omega_a)$, $J_{\pm1}^{DD}(\omega_a)$ and $J_{\pm2}^{DD}(\omega_a)$, which are obtained from a non-linear least squares fit to the orientation-dependent data. In particular, the data of Fig. 33 lead to $J_1^{DD}(\omega_a) < J_0^{DD}(\omega_a) < J_2^{DD}(\omega_a)$, which immediately rules out a variety of mechanisms proposed for liquid crystalline phases. However, a model due to Moro and Nordio (83) for molecular dynamics in smectic phases was found to be consistent with the results. It is based on the idea that the orientational potential felt by a molecular probe should depend upon the probe location within the bilayer. Thus

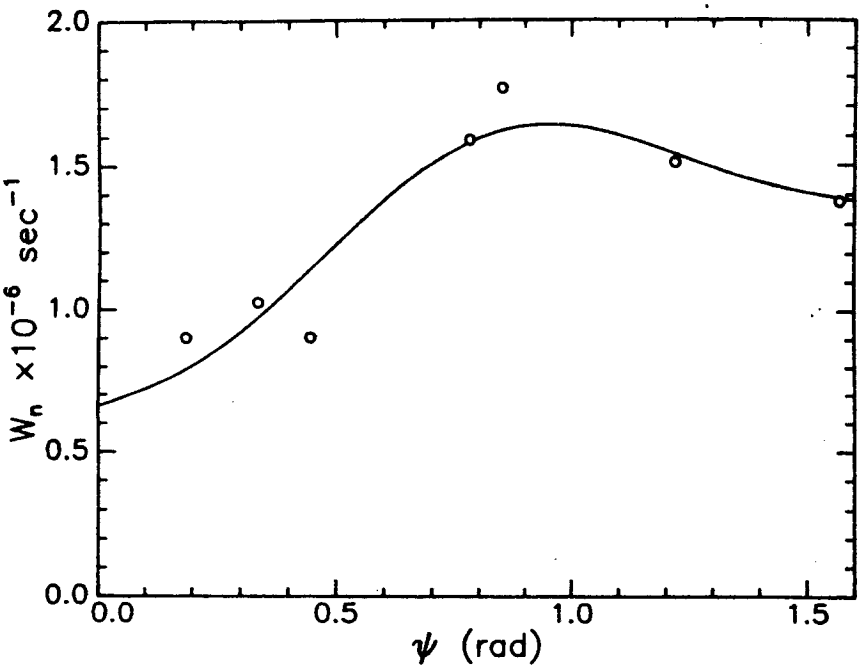

Fig. 33. Orientation dependence of nuclear spin flip rate W_n for PD-Tempone in the liquid crystal S2 at 20°C. [From Ref. 72].

the probe will experience a coupled orientation-position potential as it diffuses in the spatially non-uniform liquid crystalline bilayers. It has been possible to obtain consistently good fits between this model and the angular dependence of W_n over a range of T in the smectic phase. Additional information is obtainable from the orientation-dependent T_2 measurements by ESE (72) which are illustrated in Fig. 34. Combined with the W_n measurements, they provide the zero frequency spectral densities: $J_M^{DD}(0)$, $J_M^{DD}(0)$ where M=0,1,2. The predicted qualitative trends for the J(0) are observed experimentally, but in general, we find that the $J(0) > J(\omega_e)$, and that the J(0) from experiment are greater than predicted. This suggests a second dynamical mechanism which selectively enhances the zero-frequency spectral densities. Such a mechanism would have to be relatively slow in order to affect J(0) predominantly. It was speculated that this may be due to cooperative fluctuations in the hydrocarbon chains sensed by the probe.

Finally, we demonstrate the importance of measuring accurate homogeneous T_2's rather than cw linewidths (i.e. $T_{2,cw}^{-1}$) in ordered media, as discussed in Sect. 2. We show in Fig. 35 how the two differ, especially for the $M_I \rightarrow +1$ hf line for which $T_{2,cw} < T_2$. Furthermore, we find that the orientation dependence of $T_{2,cw}$ is inconsistent with that for the homogeneous T_2's from ESE. In fact, the observed $T_{2,cw}$ may be obtained by simulating the effects of a static distribution of director orientations which is magnetic-field dependent, such as shown by Lin and Freed (25) earlier.

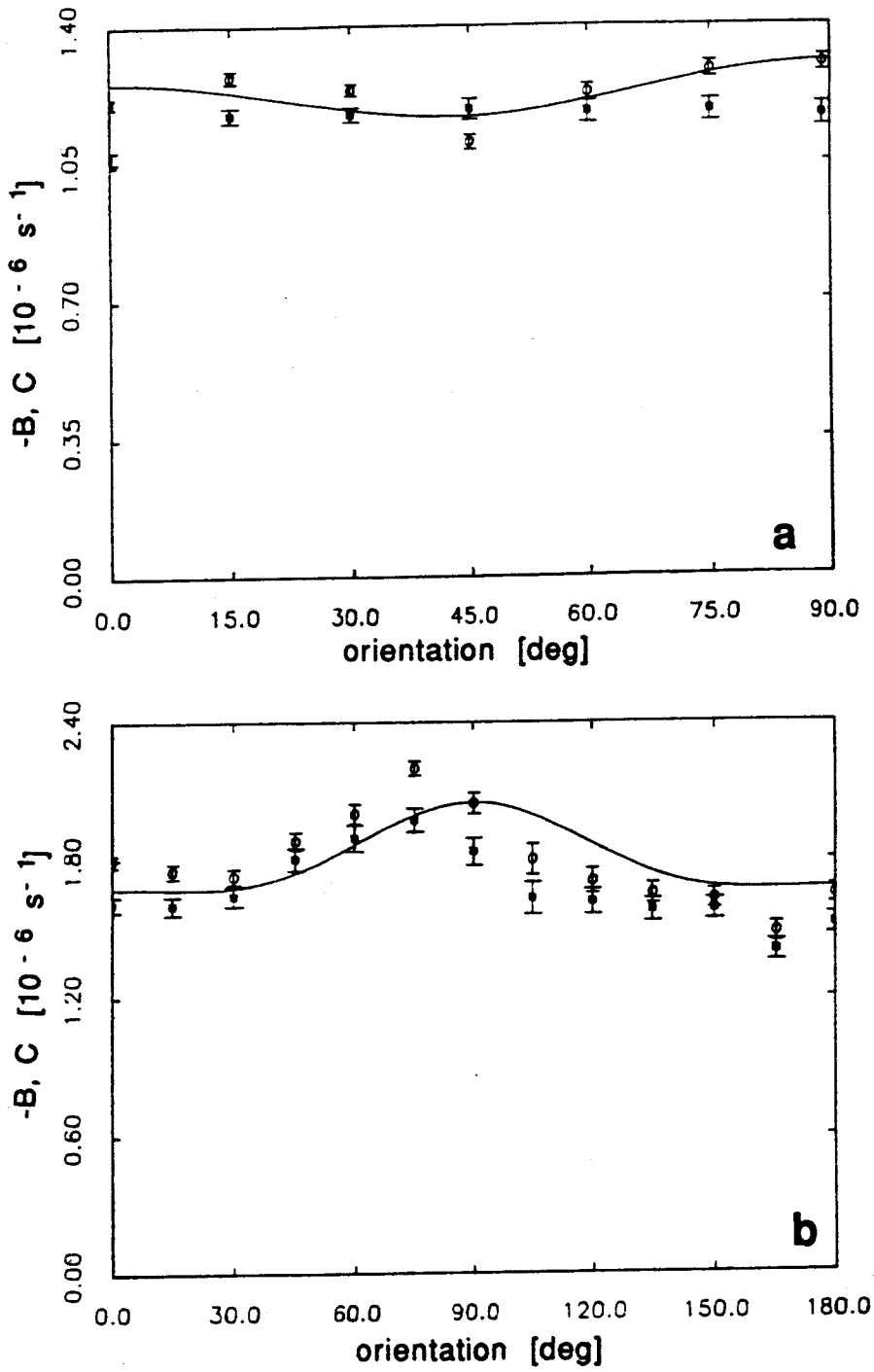

Fig. 34. Orientation dependence of linewidth parameters B and C determined by ESE for PD-Tempone in S2 at (a) 38°C (b) 31°C. B and C were calculated from experimental T_2's according to $T_2(M_I)^{-1} = A + BM_I + CM_I^2$ [From Ref. 72].

In summary, note (i) the extensive and reliable information provided by these new techniques which bear directly on molecular dynamics in multi-bilayers; (ii) their utility in discriminating between models.

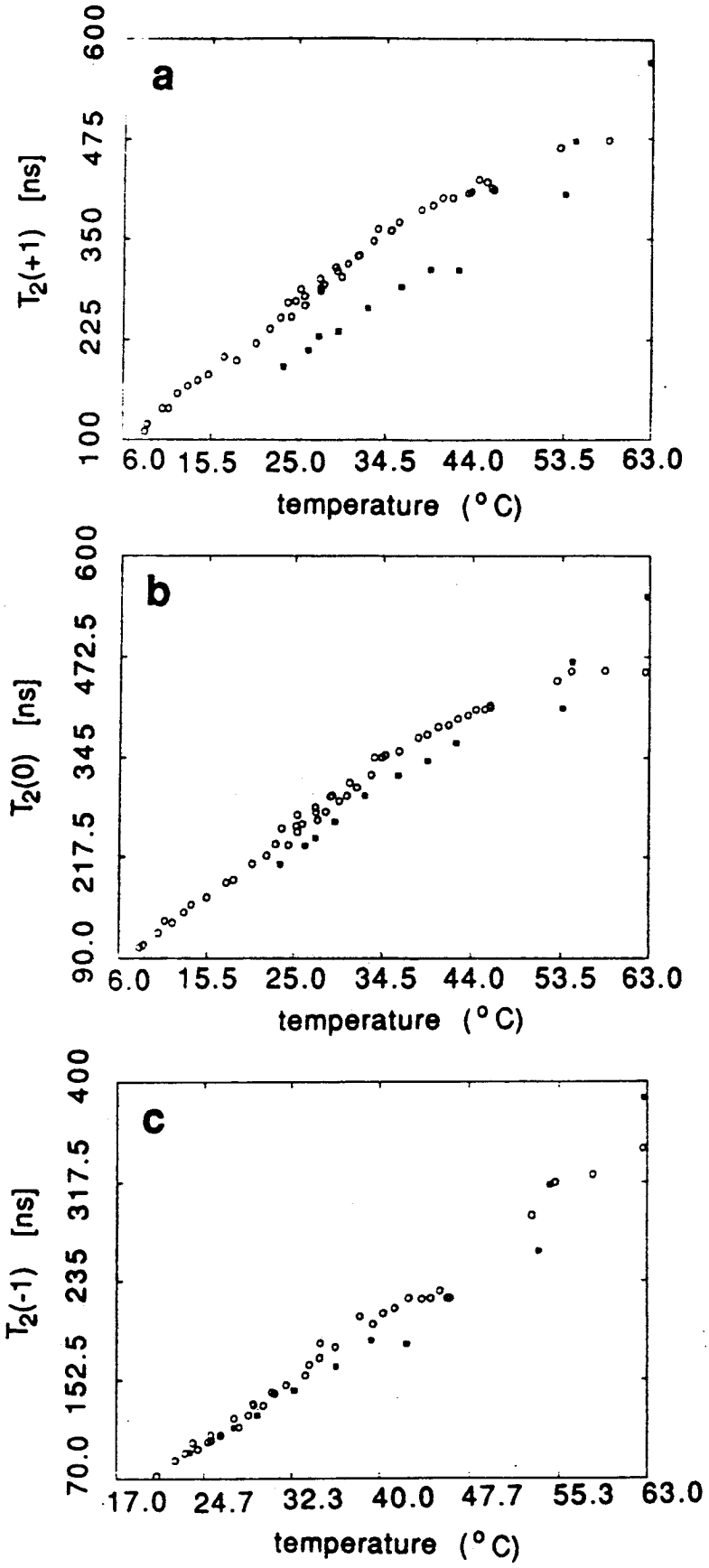

Fig. 35. Temperature dependence of homogeneous (o) T_2 from ESE and (▪) $T_{2,cw}$ for the three hyperfine lines of PD-Tempone in S2. [From Ref. 72].

6.5 Theory of 2D-ELDOR and COSY (67,68,72)

The FID following a single pulse is given by the expression

$$s(t) = B' \sum_j a_j \exp(-\Lambda_j t), \qquad [22]$$

where the complex coefficients a_j are given by:

$$a_j = \sum_{l,m} U_l O_{o,lj} O_{o,mj} U_m, \qquad [23]$$

according to the notation we have already introduced.

The expression for 2D-ELDOR is:

$$s'_{ELDOR}(T,t_1,t_2) = B' \sum_{l,m,n} c_{lmn} \exp(-\Lambda_n t_2) \exp(-T/\tau_m) \, \mathrm{Re} \sum_j b_{lj} \exp(-\Lambda_j t_1) \qquad [24]$$

where

$$c_{lmn} = \sum_{k,r} U_r O_{o,rn} O_{o,kn} O_{d,km} O_{d,lm} \qquad [25]$$

and

$$b_{lj} = \sum_p O_{o,lj} O_{o,pj} U_p \qquad [26]$$

where, for simplicity, we have ignored the V_j factors, corresponding to the assumption of uniform spectral rotation by the pulses. The result of Eqns. [24]-[26] is closely related to that of Eqn. [12] for the field-swept MT experiment, except for the fact that an FID (rather than an echo is detected).

Eqns. [24]-[26] represent only one of several terms predicted by the theory; in particular, they represent the contribution to the 2D spectrum which provides the ELDOR information. We may identify four independent contributions to the time-domain spectral function $s(T,t_1,t_2)$,

$$s'_{(x,x,x)}(T,t_1,t_2) = s'_{ELDOR} + s'_{Transverse} + s'_{Axial(E)} + s'_{Axial(M)}. \qquad [27]$$

where (x,x,x) identifies, for each pulse, the axis of rotation by B_1. s'_{ELDOR} is the contribution given by Eqns. [24]-[26], while $s'_{Transverse}$ is the contribution associated with the transverse interference discussed above, and $s'_{Axial(E)}$ and

$s'_{Axial(M)}$ are the terms associated with axial peaks (60). The quadrature component is written analogously as

$$s_{(y,x,x)}(T,t_1,t_2) = s''_{ELDOR} + s''_{TRANSVERSE} + s''_{Axial(E)} + s''_{Axial(M)}. \quad [28]$$

The phase cycling sequences cancel out $s_{Transverse}$ and $s_{Axial(E)}$. The $s_{Axial(M)}$ are removed by first measuring the constant baseplane offset described below.

In the case of Figs. 25 and 28, corresponding to the motional narrowing regime with three well-separated hf lines, our expressions are greatly simplified by the fact that O_o=1, the unit matrix, and we can write them as

$$s'_{ELDOR}(T,t_1,t_2) = B' \sum_{n,m,j} c_{nmj} A_n(t_2) \exp(-T/\tau_m) \, Re[A_j(t_1)] \quad [29]$$

and

$$s''_{ELDOR}(T,t_1,t_2) = B' \sum_{n,m,j} c_{nmj} A_n(t_2) \exp(-T/\tau_m) \, Im[A_j(t_1)], \quad [30]$$

where $A_i(t)$ is defined by

$$A_i(t) = \exp(-\Lambda_i t). \quad [31]$$

The real coefficients c_{nmj} are defined by

$$c_{nmj} = U_n O_{d,nm} O_{d,jm} U_j, \quad [32]$$

with

$$O_{d,nm} = \begin{array}{c} \\ -1 \\ 0 \\ +1 \end{array} \begin{array}{c} \begin{array}{ccc} 1 & 2 & 3 \end{array} \\ \begin{pmatrix} 3^{-1/2} & 2^{1/2} & 6^{-1/2} \\ 3^{-1/2} & 0 & -2(6)^{-1/2} \\ 3^{-1/2} & -2^{-1/2} & 6^{-1/2} \end{pmatrix} \end{array} \quad [33]$$

and with $n=M_I=-1,0,1$ and

$$\tau_1^{-1} = 2W_e, \quad [34]$$

$$\tau_2^{-1} = 2W_e + 2W_n + \omega_{HF}, \quad [35]$$

$$\tau_3^{-1} = 2W_e + 6W_n + \omega_{HF}. \quad [36]$$

[The presence of chemical exchange and/or pseudo-secular EED terms would lead to an effective exchange frequency ω_{EX} replacing ω_{HE} in these expressions (47)].

The U_n in Eqn. [32] are given by $U_n=i\epsilon/2$ where $-\epsilon$ is the equilibrium population difference for an isotropic system, given by $g\beta_e H_o/k_B T$ in the high-field limit. Eqns. [33]-[36] are appropriate when the nonsecular contributions from the g-tensor, hf-tensor, and EED tensor may be neglected. More generally, up to five τ_m would be required for a nitroxide. This case is discussed in detail in (68,72).

We see immediately from Eqns. [29] and [30] that the effect of the 2D quadrature phase alternation scheme is to select the real part of the time-domain spectral function $A_j(t_1)$ in the case of s' and the imaginary part in the case of s".

Upon FT with respect to t_2 we obtain $\hat{s}_{(x,x,x)}(T,t_1,\omega_2)$ and $\hat{s}_{(y,x,x)}(T,t_1,\omega_2)$ at which time we form (66):

$$\hat{s}(T,t_1,\omega_2) = Re[\hat{s}_{(x,x,x)}] + iRe[\hat{s}_{(y,x,x)}]. \qquad [37]$$

Then FT with respect to t_1 yields the 2D spectrum given by

$$S_{ELDOR} = S'_{ELDOR}(T,\omega_1,\omega_2) + iS''_{ELDOR}(T,\omega_1,\omega_2) \qquad [38]$$

with

$$S'_{ELDOR}(T,\omega_1,\omega_2) = B' \sum_{n,m,j} c_{nmj} \frac{1}{i\omega_1-\Lambda_j} \exp(-T/\tau_m)\, Re \frac{1}{i\omega_2-\Lambda_n} \qquad [39]$$

and with $S''_{ELDOR}(T,\omega_1,\omega_2)$ given by Eqn. [39] but with Re replaced by Im.

As noted above, we are left with the one remaining unwanted $S_{Axial(M)}$ after phase cycling, and it is removed during data analysis. One finds (67,68) that $s'_{Axial(M)}(T,t_2)$ is independent of t_1, and it constitutes the only contribution to $\bar{s}_{(x,x,x)}(T,t_1,t_2)$ with this property. Thus we first estimate a constant baseplane offset in $\bar{s}_{(x,x,x)}(T,t_1,\omega_2)$, which we identify with $\bar{s}'_{Axial(M)}(T,\omega_2)$. Then we subtract this baseplane from $\bar{s}_{(x,x,x)}(T,t_1,\omega_2)$, and repeat this procedure with $\bar{s}_{(y,x,x)}$ prior to FT with respect to t_1. The experimental implementation is not perfect. There is residual amplitude associated with axial peak contributions, and it gives rise to the distortions seen along $\omega_1=0$ in the spectra of Figs. 23, 25, and 28. [Additional distortions near $\omega_1=0$ arise from the extra amplitude modulation in t_1 due to distortions in the second MW pulse (causing a variation of the rotation angle for this pulse) as a function of interpulse delay t_1, which is a problem analogous to that in NMR (84)]. Combining Eqns. [32] and [39] and introducing the factors V_j, we obtain

$$ReS'_{ELDOR}(T,\omega_1,\omega_2) = B'\sum_{n,m,j} U_n V_n \frac{T_{2,n}}{1+(\omega_2-\omega_n)^2 T_{2,n}^2} U_j V_j^2 \frac{T_{2,j}}{1+(\omega_1-\omega_j)^2 T_{2,j}^2} \times O_{d,nm} O_{d,jm} \exp(-T/\tau_m), \quad [40]$$

applicable in the motional narrowing regime with well-separated hf lines. Here, $T_{2,j}$ and ω_j are the T_2 and resonant frequency of the j^{th} hf line. For the purpose of simulation one need only compute Eqn. [40].

We have neglected inhomogeneous broadening in the above analysis, as it does not play a significant role in the interpretation of 2D-ELDOR data in the motional narrowing regime (other than to broaden each resonance line by a small amount). The effect of including significant inhomogeneous broadening in the theory is that there would be several types of spin echo : viz. three spin echoes associated with each pair of pulses, plus a stimulated echo and a twice refocussed echo. [These matters are discussed elsewhere (24,36)]. These are the terms which would be important for slow motional 2D-ELDOR spectra, where $T_2^* < \tau_d$, so an FID technique would not be appropriate. Instead, one could observe the stimulated echo, which has a structure very similar to that of Eqns. [24]-[26], whereas the others would be canceled by phase cycling.

Before discussing 2D-ELDOR further, we note that a similar analysis leads to motional narrowing expressions for COSY-EPR:

$$s'_{COSY}(t_1,t_2) = -B' \sum_n U_n^2 A_n(t_2) Re[A_n(t_1)] \quad [41]$$

and

$$s''_{COSY}(t_1,t_2) = B' \sum_n U_n^2 A_n(t_2) Im[A_n(t_1)]. \quad [42]$$

Eqns. [41] and [42] predict a COSY spectrum without cross-peaks, consistent with the experimental result of Fig. 25. However, given sufficiently rapid exchange (e.g. ω_{HE} comparable to the hyperfine splittings), O_o is no longer simply the identity operator 1, and cross-peaks are predicted to appear in the COSY spectrum. It is also true in general that $O_o \neq 1$ in the slow-motional regime, hence one finds cross-terms in the appropriate analogues of Eqns. [41] and [42].

We now consider the analysis of the 2D-ELDOR experiment for a motionally-narrowed nitroxide spectrum with three well-separated hf lines characteristic of a nitroxide. We obtain from the experiment the 3×3 matrix Q(T) of volume integrals. [The matrix Q(T) is defined such that Q_{mj} is the volume integral of the

cross-peak located at coordinates $(\omega_1,\omega_2)=(\omega_j,\omega_n)$]. According to Eqn. [40] we can write:

$$Q_{nj}(T) = E \sum_m O_{d,nm} O_{d,jm} \exp(-T/\tau_m) \qquad [43]$$

where E is a spectrometer constant. The expressions for the matrix elements Q_{nj} (within the spectrometer constant) are given in Table 1 for the case when Eqns. [33] and [34] are applicable. In the analysis of experiments, one utilizes ratios: $f_{mj} = Q_{nj}/Q_{jj}$ thereby canceling the spectrometer constant, E.

In the very simplest case where W_e is negligible and Heisenberg exchange is the only source of magnetization transfer, one obtains after some algebra:

$$\omega_{HE} = \frac{1}{T} \ln \frac{2f_{mj}V_j r_{2j} + V_m r_{2m}}{V_m r_{2m} - f_{mj} V_j r_{2j}} \qquad [44]$$

Here the r_{2j} measure the dead-time reduction factors (as well as the filtering effects of the resonator with its finite Q) on the FID's collected as a function of t_2. The products $V_j r_{2j}$ are determined by measuring the normalized peak areas obtained from a single pulse FID collected under the same conditions (i.e. same dead time, pulse length, etc.) as the 2D-ELDOR spectrum.

Note that Eqn. [44] predicts that all six cross-peaks equivalently reflect the exchange process, and hence that six independent measurements of the exchange rate ω_{HE} are obtained from a single 2D spectrum. The equivalence of the six cross-peaks is a manifestation of the lack of a selection rule for the exchange mechanism (74), i.e. both $\Delta M_I=\pm1$ and $\Delta M_I=\pm2$ transitions are equally probable.

TABLE 1. Matrix Elements $E^{-1}Q_{nm}(T)$:[(a)]

Auto-Peaks[(b)]	
$E^{-1}\ Q_{\pm1,\pm1}$:	$\frac{1}{3}\exp[-T/\tau_1] + \frac{1}{2}\exp[-T/\tau_2] + \frac{1}{6}\exp[-T/\tau_3]$
$E^{-1}Q_{o,o}$:	$\frac{1}{3}\exp[-T/\tau_1] + \frac{2}{3}\exp[-T/\tau_3]$
Cross-Peaks	
$E^{-1}\ Q_{o,\mp1} = E^{-1}Q_{\mp1,0}$:	$\frac{1}{3}\exp[-T/\tau_1] - \frac{1}{3}\exp[-T/\tau_3]$
$E^{-1}\ Q_{\pm,\mp1}$:	$\frac{1}{3}\exp[-T/\tau_2] - \frac{1}{2}\exp[-T/\tau_2] + \frac{1}{6}\exp[-T/\tau_3]$

(a) This is the case of negligible non-secular terms.
(b) These apply both to 2D-ELDOR and to Stimulated Echoes from the three hyperfine lines.

The W_n mechanism and the exchange mechanism may be distinguished in these spectra as a result of their different selection rules. Unlike exchange, the W_n mechanism obeys the selection rule $\Delta M_I=\pm 1$ and thus gives rise predominantly to cross-peaks connecting only adjacent hf lines, (cf. Fig. 30), but see below. Thus the geometrical pattern of the spectral contours may be utilized to obtain information regarding the mechanism of magnetization transfer prior to the application of Eqn. [44] or its analogues for $W_n \neq 0$. If we consider, for example, a case where only cross-peaks for which $\Delta M_I=\pm 1$ are significant, we can write by analogy to Eqn. [44],

$$6W_n = -\frac{1}{T} \ln \frac{2\hat{Q}_{mj}V_j r_{2j} + V_m r_{2m}}{V_m r_{2m} - \hat{Q}_{mj}V_j r_{2j}} \qquad [45]$$

which applies to the two cross-peaks for which $m=\pm 1$ and $j=0$. In Eqn. [45], $\hat{Q}_{mj} = Q_{mj}/Q_{oo}$. Thus in the event that $\omega_{HE}=0$ one can obtain W_n directly from two of the four cross-peaks with the application of Eqn. [45]. The expression for the other two cross-peaks (i.e. $m=0, j=\pm 1$), is somewhat more complicated. These cross-peaks nevertheless directly yield W_n provided exchange is absent. If cross-peaks for which $\Delta M_I=\pm 2$ are significant, then the left side of Eqn. [45] requires an additive factor involving ω_{HE}. The full set of linear equations applicable when $\omega_{HE} \neq W_n \neq 0$ has been given elsewhere for all six cross-peaks (68,72).

The overdetermined set of six linear equations may be used to obtain both W_n and ω_{HE}. Note that the presence of cross-peak intensity at $\Delta M_I=\pm 2$ does not always imply the presence of Heisenberg exchange; the W_n mechanism may also contribute intensity to these peaks by a small amount, but only for sufficiently long mixing times T, i.e. when $W_nT > 1$, (cf. Table 1). The absence of $\Delta M_I=\pm 2$ peaks is easily shown by expanding $Q_{\pm 1 \mp 1}$ given in Table 1 to lowest power in W_nT.

These expressions for relative peak volumes for a given mixing time, T, do not by any means exhaust the available sources of data from the 2D-ELDOR experiment. There is, after all, a third dimension available, that of mixing time T. From a series of 2D-ELDOR spectra at different values of T, one can map out the T dependence of <u>all nine</u> auto- and cross-peaks. Thus, for example, from Table 1 in the simple special case of $W_n=0$, we obtain for the auto-peaks

$$Q_{nn}(T) \propto \exp[-2W_eT] + 2\exp[-(2W_e + \omega_{HE})T] \qquad n=-1,0,1 \qquad [46]$$

and for the cross peaks

$$Q_{nm}(T) \propto \exp[-2W_eT] - \exp[-(2W_e + \omega_{HE})T) \qquad n \neq m \qquad [47]$$

In general, each peak shows a time evolution given by a sum of exponentials which may be fit to provide W_e, W_n, and ω_{HE}. The Q_{nn} vs. T represents equivalent information to that of stimulated echoes, whereas the Q_{nm} vs. T for $n \neq m$ are equivalent to that from ELDOR echoes. We have found that for accurate and reliable estimation of relaxation rates, it is a good idea to obtain 2D-ELDOR at 3 or 4 values of T for which all the peaks are prominent. As 2D-ELDOR techniques improve and data acquisition rates are increased, it should become practical to obtain 2D-ELDOR for significanty more values of T, which would then more truly represent a 3D experiment.

6.6 Future Uses of 2D-FT-EPR

We have illustrated how FT-EPR is capable of routine use in several applications. We plan to develop the technique to be applicable to all studies involving nitroxides. Until very recently, one was limited to the application of FT methods to spectra not exceeding about 100 MHz spectral bandwidth. We have illustrated applications of the FT technique that do not require uniformity of effective rotation by B_1 across the entire spectrum. Such "B_1 uniformity" is not a necessity for the implementation of most two-dimensional techniques. The effects of B_1 non-uniformity can be accounted for in simulations by recognizing that spectral components which are only partially rotated by the pulses have reduced effective transition moments (65,67,68), as we have presented in Eqns. [17]-[19] or [40]. We have illustrated the utility of two-dimensional FT spectroscopy as a double resonance technique which yields quantitative information without necessarily requiring simulation or least-squares fitting of the data. We did find, however, that least-squares fitting in the form of linear prediction is a convenient method for projection of the pure 2D absorption representation of 2D-ELDOR data necessary for determination of volume integrals of the 2D absorption lines. It can also be effectively utilized to remove artifacts, such as residual axial peaks, and to significantly improve the signal-to-noise.

In the application of this technique to slow-tumbling motions of nitroxides one would obtain all of the ELDOR data in a single 2D spectrum. Such spectra would yield information about the couplings between dynamic spin-packets corresponding to different molecular orientations which can provide considerable insight into the microscopic details of the motional process (14,24,36-38,39,85). The implementation of a 2D-ELDOR experiment for the study of slow-tumbling motions would be somewhat different than described for motionally narrowed systems. FID's in these systems are, in general, rapidly damped as a result of the large inhomogeneous line widths, which are not averaged by the motion as in the motionally narrowed spectra. The FID will, in general, be lost in the dead-time following a microwave pulse. In these instances, the transverse magnetization can still be refocussed into a spin echo. In the 2D-ELDOR experiment one would have the option of applying an additional refocussing pulse or of recording the

stimulated echo following the third pulse. The latter method would have the advantage that axial-peaks will not be refocussed and therefore cannot contribute intensity to the 2D-ELDOR spectrum.

In another application, the implementation of SECSY to slow-tumbling nitroxides would be identical to the method described in Sect. 6.2 for motionally narrowed spectra, except that reduction of the DC magnetic field homogeneity is not required. This SECSY application would be the 2D-FT analogue of the field-swept 2D experiment described in Sect. 3. It would have the advantages of (i) greatly reduced data acquisition times; (ii) pulse widths significantly shorter than the relevant T_2's. It would also be useful for the study of echo-modulation patterns and how they vary across a spectrum (cf. Sect. 5).

Many other possibilities exist for the application of other two-dimensional spectroscopies to EPR. We mention one potential application of COSY-EPR to the study of distances in macromolecules such as proteins. Suppose an ^{14}N and an ^{15}N label are placed at two distinct sites in a protein, and in a rigid-limit spectrum they are coupled by the dipolar interaction between the two electron spins. Then from the COSY cross-peaks between the ^{14}N and ^{15}N spectra, one could, in principle, measure the dipolar interaction from which $1/r^3$ could be obtained.

Access to the full range of nitroxide spectra with FT techniques requires at least a doubling of the spectrometer bandwidth. The main challenge is the generation of sufficiently large B_1 fields at the sample. Based upon our current experience, a 220 MHz spectrum would require at least a 1.4 mT B_1 field at the sample in a rectangular pulse of width about 6 nsec. There is not sufficient power to rotate on-resonant magnetization by $\pi/2$ in a low Q cavity resonator. However, a loop-gap resonator, (86,87) which has been stabilized against electric breakdown, has enabled the generation of a large B_1 at the sample because of the high conversion efficiency of these resonators. To date we have obtained B_1 field strengths of 1.5 mT in a bridged loop-gap resonator (88) having a Q of 45 (68,89). Such a combination of high B_1 and wide bandwidth facilitates nearly uniform excitation of isotropic motionally narrowed spectra such as PD-Tempone in toluene-d_8 (cf. Fig. 36 for the "one-dimensional" FT) or PD-Tempone in the nematic liquid crystal phase V (cf. Fig. 37 for the 2D-ELDOR). As a result of these new developments, it is now possible to obtain 2D-ELDOR spectra from lipid dispersions in the liquid crystalline phase containing fatty acid spin labels. These are especially challenging, since the three hyperfine lines are inhomogeneously broadened due to the random orientation of the lipid fragments (6,8) with $T_2^* \approx$ 20-30 nsec. Nevertheless, interesting patterns of auto- and cross- peaks may be obtained as illustrated in Fig. 38.

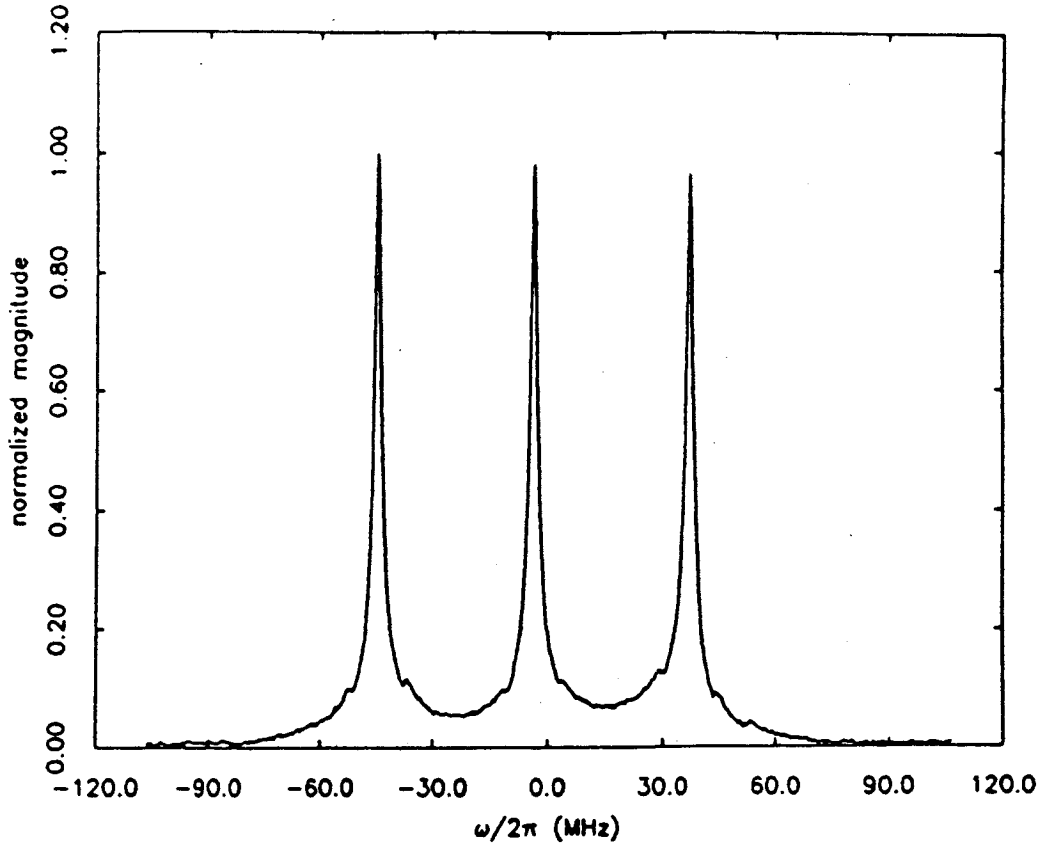

Fig. 36. FT spectrum of 5.0×10^{-4} M PD-Tempone in toluene-d_8 at 22°C obtained with a bridged loop-gap resonator. $\pi/2$ pulse width was 6.7 nsec, resolution in t_2 is 4.69 nsec, 2048 averages, 256 complex data points zero-filled to 1024 prior to Fourier transformation [from Ref. 68].

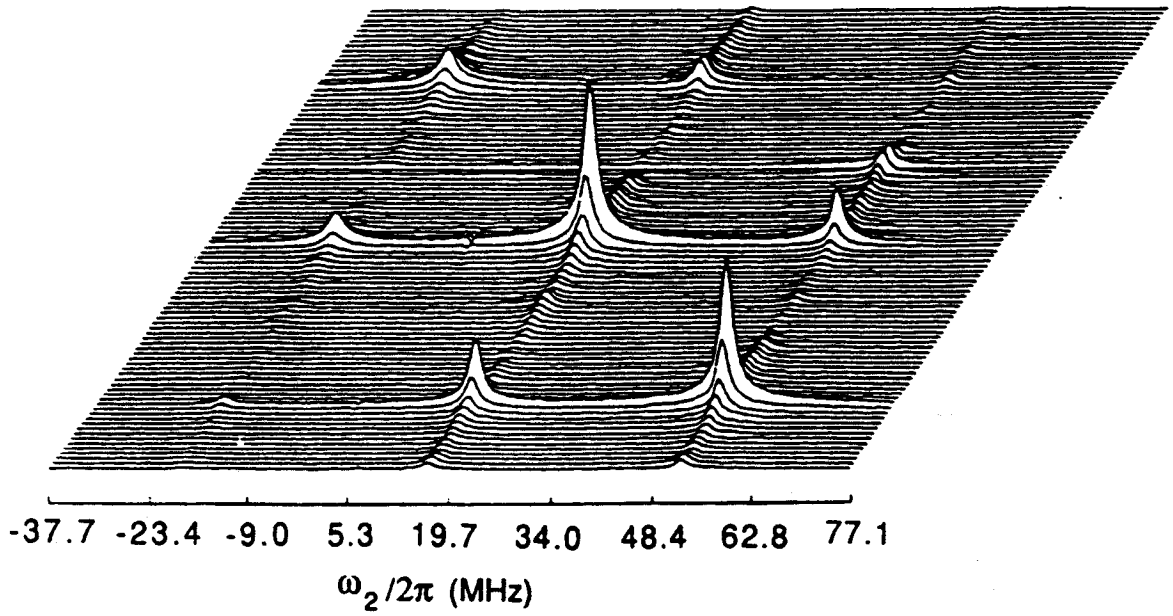

Fig. 37. Absolute value 2D-ELDOR spectrum of 5.0×10^{-4} PD-Tempone in phase V at 24°C obtained with a bridged loop-gap resonator; τ_p=9.5 nsec; Δt_1=7 nsec; Δt_2=3.9 nsec; 8-step phase alternation sequence; dead time in t_2 of 150 nsec; dead time in t_1 of 100 nsec; mixing time T=6.0×10^{-7} sec; acquisition time 49 minutes [From Ref. 68].

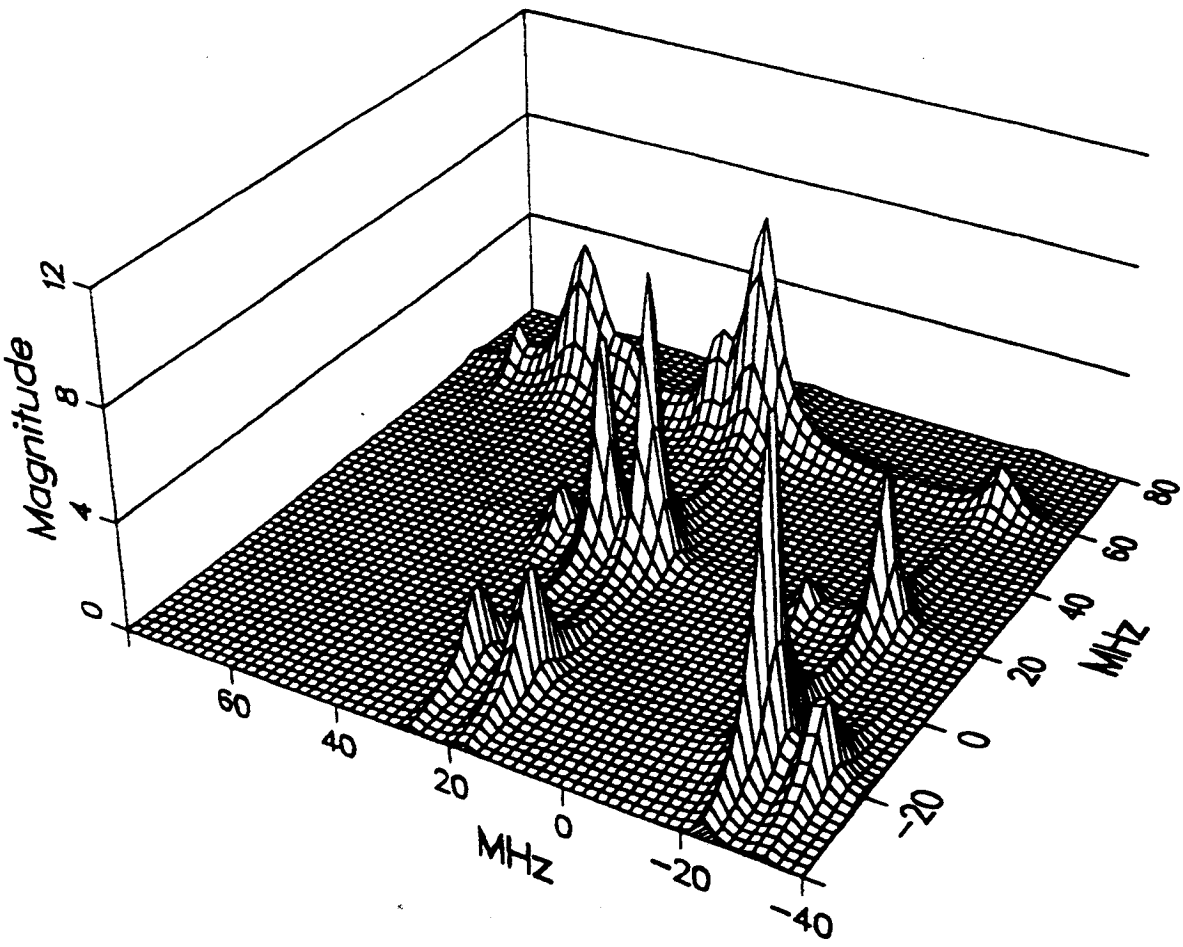

Fig. 38. 2D-ELDOR spectrum of 16-stearic acid spin label in at 0.5 mole percent in DMPC at 74.5°C. The lipid dispersion is in a buffer of 0.01 M KH_2PO_4 (pH=7) at concentration of 0.5 mg phospholipid/μl. The mixing time, T=500 nsec. The data have been treated by 2D-LPSVD to reduce noise, remove axial peaks, and correct for dead-time effects (due to t_1 and t_2 dead-times of 80 and 130 nsec, respectively) [Results obtained by R.H. Crepeau in these labs.]

In order to make the field more uniform across the spectrum, the possibility of using shaped pulses (89,90) is being investigated. A nearly rectangular pulse shape is used only as a matter of convenience; the response of the magnetization to such a pulse is of the form $\sin(\omega t_p)/\omega t_p$ and is far from optimal for FT work because of the points of null-response (65). Shaping of pulses can contain all of the available microwave power within a single band or envelope, thus improving the conversion of microwave power into useful B_1. Other possibilities for improvement of the present spectrometer include the use of a high sweep-rate 200 MHz digitizer which has just become available. We predict a reduction in FID acquisition time by at least an order-of-magnitude with the implementation of such digitizers. Also under investigation is the design of a multi-frequency superheterodyne FT spectrometer taking advantage of new multi-octave stripline devices.

In cases where B_1 field strengths are insufficient for total spectral coverage, variations of the techniques described in this report may be of interest. These are techniques of two-dimensional correlation spectroscopy which require that only a limited region of the spectrum be irradiated (so called "soft COSY" techniques (91)). A "soft" 2D-ELDOR spectra would provide information about the couplings among only those dynamic spin packets rotated by the microwave pulse. In these experiments one could collect several such 2D spectra, each focussing on a different region of the spectrum, and then combine the data during data analysis. Related techniques are already frequently utilized in NMR for 2D nuclear Overhauser spectroscopy of systems of biological interest.

It is clear that full bandwidth irradiation techniques will be limited to specific suitable applications in EPR. These will probably not, for the foreseeable future, include transition metals in liquid solution. Transition metal spectra have bandwidths of up to several gigahertz requiring B_1's of 10-100 mT, and their T_2's in liquids are too short (typically less than or on the order of nanoseconds). Nevertheless, solid state experiments on inorganic ions by field-swept 2D-ESE such as illustrated in Sect. 5 are quite feasible. The methods described in this section are generally applicable to studies of organic free radicals, because their spectral bandwidths usually do not exceed 100-200 MHz, and their T_2's are usually significantly greater than a nanosecond.

Finally, we believe that the range of applications of 2D-FT-EPR to biophysics will continue to increase as new developments in high-speed electronics, resonators, and microwave devices find their way into the research laboratory.

ACKNOWLEDGEMENTS

We thank David Budil and Betsey Van Sickle for assistance with the final manuscript. This research was supported by NIH Grant #GM25862, NSF Grants CHE87-03014 and DMR 8604200, and the Cornell Materials Science Center.

REFERENCES

1 L.J. Berliner (Ed.), *Spin Labeling: Theory and Applications*, Vol. I, Academic, New York, 1976.
2 L.J. Berliner (Ed.), *Spin Labeling: Theory and Applications*, Vol. II, Academic, New York, 1979.
3 L.J. Berliner and J. Reuben (Eds), *Biological Magnetic Resonance*, Vol. 8, Spin Labeling: Theory and Applications III, Plenum, New York, 1989.
4 J.J. Volwerk and O.H. Griffith, *Mag. Res. Rev.* 13, (1988) 135-178.
5 J.H. Freed in: L.J. Berliner (Ed.), *Spin Labeling: Theory and Applications*, Vol. I, Academic, New York, 1976, Ch. 3.
6 E. Meirovitch, A. Nayeem, and J.H. Freed, *J. Phys. Chem.*, 88 (1984) 3454-3465.
7 E. Meirovitch and J.H. Freed, *J. Phys. Chem.*, 84 (1980) 3281-3295, 3295-3303.
8 H. Tanaka and J.H. Freed, *J. Phys. Chem.*, 88 (1984) 6633-6644.
9 H. Tanaka and J.H. Freed, *J. Phys. Chem.*, 89 (1985) 350-360.
10 L. Kar, E. Ney-Igner, J.H. Freed, *Biophys. J.*, 48 (1985) 569-595.
11 Y.-K. Shin and J.H. Freed, *Biophys. J.* 55, (1989) 537-550.

12 D.J. Schneider and J.H. Freed, in: L.J. Berliner and J. Reuben (Eds), *Biological Magnetic Resonance*, Vol. 8, Plenum, New York, 1989, Ch. 1.
13 K.V. Vasavada, D.J. Schneider, and J.H. Freed, *J. Chem. Phys.*, 86 (1987) 647-661.
14 D.J. Schneider and J.H. Freed, in: J.O. Hirschfelder *et al.* (Eds), *Lasers, Molecules, and Methods*, *Adv. Chem. Phys.*, 73 (1989) 387-527.
15 J.H. Freed, in: T. Dorfmüller and R. Pecora (Eds), *Rotational Dynamics of Small and Macromolecules in Liquids*, Springer-Verlag, New York, 1987, pp. 89-142.
16 G.L. Millhauser, J. Gorcester, and J.H. Freed, in: J.A. Weil (Ed.), *Electronic Magnetic Resonance of the Solid State, Can. Soc. for Chemistry*, Ottawa, 1987, pp. 571-597.
17 L. Kevan and R.N. Schwartz (Eds), *Time Domain Electron Spin Resonance*, Wiley-Interscience, New York, 1979.
18 K.M. Salikhov, A.G. Sevenov, and Yu. D. Tsvetkov, *Electron Spin Echoes and Their Applications*, Nauka, Novosibirsk, 1976.
19 W.B. Mims and J. Peisach, in: L.J. Berliner and J. Reuben (Eds), *Biological Magnetic Resonance*, Vol. 3, Plenum, New York, 1981, Ch. 5.
20 J.R. Norris, M.C. Thurnauer, and M.K. Bowman, *Adv. Biol. Med. Phys.*, 17 (1980) 365-415.
21 A.E. Stillman and R.N. Schwartz, *J. Phys. Chem.*, 85 (1981) 3031-3040.
22 A.E. Stillman, L.J. Schwartz, and J.H. Freed, *J. Chem. Phys.*, 73 (1980) 3502-3503.
23 L.J. Schwartz, A.E. Stillman, and J.H. Freed, *J. Chem. Phys.* 77 (1982) 5410-5425.
24 L.J. Schwartz, Ph.D. Thesis, Cornell University, 1984.
25 a) W.J. Lin and J.H. Freed, *J. Phys. Chem.*, 83 (1979) 379-401; b) E. Meirovitch and J.H. Freed, *ibid.*, 84 (1980) 2459-2472.
26 R.P. Mason and J.H. Freed, *J. Phys. Chem.*, 78 (1974) 1324-1329; b) R.P. Mason, E.B. Giavedoni, and A.P. Dalmasso, *Biochemistry*, 16 (1977) 1196-1201.
27 D. Kivelson and S. Lee, *J. Chem. Phys.*, 76 (1982) 5746-5754.
28 U. Eliav and J.H. Freed, *Rev. Sci. Instrum.* 54 (1983) 1416-1417.
29 G.L. Millhauser and J.H. Freed, *J. Chem. Phys.*, 81 (1984) 37-48.
30 L.J. Kar, G.L. Millhauser, and J.H. Freed, *J. Phys. Chem.*, 88 (1984), 3951-3956.
31 Y. Shimoyama, D.J. Schneider, G.L. Millhauser, and J.H. Freed, (to be published).
32 G.L. Millhauser and J.H. Freed, *J. Chem. Phys.*, 85 (1986) 63-67.
33 G.L. Millhauser, D.S. Clark, and J.H. Freed (unpublished); G. A. Marg, G.L. Millhauser, P.S. Skerkev, D.S. Clark, *Ann. NY Acad. Sci.* 469 (1986) 253-258.
34 L. Kar, M.E. Johnson, and M.K. Bowman, J. Magn. Res., 75 (1987) 397-413.
35 J.S. Hyde and L.R. Dalton, in: L.J. Berliner (Ed.), *Spin Labeling: Theory and Applications*, Vol. II, Adacemic, New York, 1979, Ch. 1.
36 L.J. Schwartz, G.L. Millhauser, and J.H. Freed, *Chem. Phys. Lett.*, 127 (1986) 60-66.
37 J.H. Freed, *J. Phys. Chem.*, 78 (1974) 1155-1167.
38 J.H. Freed, in: L. Kevan and R.N. Schwartz (Eds), *Time Domain Electron Spin Resonance*, Wiley Interscience, New York, 1979, Ch. 2.
39 J.P. Hornak and J.H. Freed, *Chem. Phys. Lett.*, 101 (1983) 115-119.
40 M. Dorio and J.H. Freed (Eds), *Multiple Electron Resonance Spectroscopy*, Plenum, New York, 1979.
41 M. Nechtschein and J.S. Hyde, *Phys. Rev. Lett.*, 24 (1970) 672-674.
42 G.V. Bruno and J.H. Freed, *Chem. Phys. Lett.*, 25 (1974) 328-332; b) G.V. Bruno, Ph.D. Thesis, Cornell University, 1972.
43 a) J.S. Hyde, M.D. Smigel, L.R. Dalton, and L.A. Dalton, *J. Chem. Phys.* 62, (1975) 1655-1667; b) L.R. Dalton, B.H. Robinson, L.A. Dalton, and P. Coffey, *Adv. Mag. Reson.*, 8 (1976) 149-259; c) L.A. Dalton and L.R. Dalton, in: M. Dorio and J.H. Freed (Eds), *Multiple Electron Resonance Spectroscopy*, Plenum, New York, 1979, Ch. 5.
44 J.S. Hyde, W. Froncisz, and C. Mottley, *Chem. Phys. Lett.*, 110 (1984) 621-625.

45 S. A. Dzuba, A.G. Maryasov, K.M. Salikhov, and Yu.D. Tsvetkov, *J. Magn. Reson.* 58 (1984) 95-117.
46 D. Marsh, in: E. Grell (Ed.), *Membrane Spectroscopy*, Springer-Verlag, W. Berlin, 1981, Ch. 2.
47 J.H. Freed, M. Dorio (Eds), *Multiple Electron Resonance Spectroscopy*, Ch. 3.
48 C.A. Popp and J.S. Hyde, *Proc. Nat. Acad. Sci. (USA)* 79 (1982) 2259-2563.
49 a) E. van der Drift and J. Smidt, *J. Phys. Chem.*, 88 (1984) 2275-2284; b) E. van der Drift, Ph.D. Thesis, Delft, 1985.
50 L. Kevan, in: L. Kevan and R.N. Schwartz (Eds), *Time Domain Electron Spin Resonance*, Wiley-Interscience, New York, 1979, Ch. 8.
51 a) E. Szajdzinska-Pietek, R. Maldonado, L. Kevan, R.R.M. Jones, S.B. Berr, *J. Am. Chem. Soc.*, 106 (1984) 4675-4678; b) E. Szajdzinska-Pietek, R. Maldonado, and L. Kevan, *ibid.*, 107 (1985) 6467-6470.
52 a) V.F. Yudanov, S.A. Dikanov, Yu. A. Grishin, and Yu.D. Tsvetkov, *J. Struct. Chem.*, 17 (1976), 387-392; b) A.A. Shubin and S.A. Dikanov, *J. Mag. Reson.*, 52 (1983) 1-12.
53 W.B. Mims, *Phys. Rev.*, B5 (1972) 2409-2419; *ibid.* B6 (1972) 3543-3545.
54 D.J. Schneider, Y. Shimoyama, and J.H. Freed, (to be published).
55 R.P.J. Merks and R. deBeer, *J. Phys. Chem.*, 83 (1980) 3319-3322.
56 R.P.J. Merks, Ph.D. Thesis, Delft University, 1979.
57 P. Höfer, A. Grupp, H. Nebenführ, and M. Mehring, *Chem. Phys. Lett.* 132 (1986), 279-282.
58 R. R. Ernst and W.A. Anderson, *Rev. Sci. Instr.*, 37 (1966) 93-102.
59 J. Jeener, Ampère Summer School, Basko Polje, Yugoslavia, 1971.
60 W.P. Aue, E. Bartholdi, and R.R. Ernst, *J. Chem. Phys.*, 64 (1976) 2229-2246.
61 R.R. Ernst, G. Bodenhausen, and A. Wokaun, *Principles of Nuclear Magnetic Resonance in One and Two Dimensions*, Oxford, New York, 1987.
62 M. Bowman, *Bull. Am. Phys. Soc.*, Ser. II, 31 (1986) 524.
63 R.J. Massoth, Ph.D. Thesis, University of Kansas, 1988.
64 J. Gorcester, G.L. Millhauser, and J.H. Freed, *Proc. XXIII Congress Ampère on Magnetic Resonance*, Rome, 1986, pp. 562-563.
65 J.P. Hornak and J.H. Freed, *J. Magn. Reson.*, 67 (1986) 501-518.
66 J. Gorcester and J.H. Freed, *J. Chem. Phys.*, 85 (1986) 5375-5377.
67 J. Gorcester and J.H. Freed, *J. Chem. Phys.*, 88 (1988) 4678-4693.
68 J. Gorcester, Ph.D. Thesis, Cornell University, 1989.
69 R. Kumaresan and D.W. Tufts, *IEEE Trans.* ASSP-30, (1982), 671-675.
70 H. Barkhuijsen, R. de Beer, W.M.M. Bovee, and D. van Ormondt, *J. Magn. Reson.*, 61 (1985) 465-481.
71 J. Gorcester and J.H. Freed, *J. Magn. Reson.*, 78 (1988) 291-301.
72 J. Gorcester, S. Rananavare, and J.H. Freed, *J. Chem. Phys.* (1989) in press.
73 D.J. States, R.A. Haberkorn and D.J. Ruben, *J. Magn. Reson.*, 48 (1982) 286-292.
74 J.H. Freed, *J. Phys. Chem.*, 71 (1967) 38-51.
75 J. Jeener, B.H. Meier, P. Bachmann, and R.R. Ernst, *J. Chem. Phys.*, 71, (1979) 4546-4553.
76 S. Macura and R.R. Ernst, *Mol. Phys.*, 41 (1980) 95-117.
77 M.P. Eastman, R.G. Kooser, M.R. Das, and J.H. Freed, *J. Chem. Phys.*, 51 (1969) 2690-2709.
78 A.E. Stillman and R.N. Schwartz, *J. Magn. Reson.*, 22 (1976) 269-277.
79 A. Nayeem, Ph.D. Thesis, Cornell University, 1986; A. Nayeem, S. Rananavare, and J.H. Freed (to be published).
80 J.S. Hwang, R.P. Mason, L.P. Hwang, and J.H. Freed, *J. Phys. Chem.*, 79 (1975) 489-511.
81 J. Yin, M. Pasenkiewicz-Gierula, and J.S. Hyde, *Proc. Natl. Acad. Sci. (USA)*, 84 (1987) 964-968.
82 G.R. Luckhurst and C. Zannoni, *Proc. Royal Soc. Lond. A.*, 353 (1977) 87-102.
83 G. Moro and P.L. Nordio, *J. Phys. Chem.*, 89 (1985) 997-1001.
84 A.F. Mehlkopf, D. Korbee, T.A. Tiggelman, and R. Freeman, *J. Magn. Reson.*, 58 (1984) 315-323.
85 G.L. Millhauser, Ph.D. Thesis, Cornell University, 1986.

86 W. Froncisz and J.S. Hyde, *J. Magn. Reson.*, 47 (1982) 515-521.
87 J.P. Hornak and J.H. Freed, *J. Magn. Reson.*, 62 (1985) 311-313.
88 S. Pfenninger, J. Forrer, A. Schweiger, and T.H. Weiland, *Rev. Sci. Instrum.*, 59 (1988) 752-760.
89 R.H. Crepeau, A. Dulcić, J. Gorcester, T. Saarinen and J.H. Freed, (*J. Magn. Reson.* submitted).
90 W.S. Warren, *J. Chem. Phys.*, 81 (1984) 5437-5448.
91 R. Brüschweiler, J.C. Madsen, C. Griesinger, O.W. Sørensen, and R.R. Ernst, *J. Magn. Reson.*, 73 (1987) 380-385.